

Analysis of solar faculae using stray-light-corrected spectropolarimetric data and numerical simulations

Dissertation

zur Erlangung des mathematisch-naturwissenschaftlichen Doktorgrades

“Doctor rerum naturalium”

der Georg-August-Universität Göttingen

im Promotionsstudiengang Physik

der Georg-August University School of Science (GAUSS)

vorgelegt von

Sudharshan Saranathan

aus Chennai, Indien

Göttingen, 2021

Betreuungsausschuss

Prof. Dr. Ansgar Reiners

Institut für Astrophysik, Georg-August-Universität Göttingen, Germany

Prof. Dr. Sami Solanki

Max-Planck-Institut für Sonnensystemforschung, Göttingen, Germany

Dr. Michiel van Noort

Max-Planck-Institut für Sonnensystemforschung, Göttingen, Germany

Mitglieder der Prüfungskommission

Referent: **Prof. Dr. Ansgar Reiners**

Institut für Astrophysik, Georg-August-Universität Göttingen, Germany

Korreferent: **Prof. Dr. Sami Solanki**

Max-Planck-Institut für Sonnensystemforschung Göttingen, Germany

Weitere Mitglieder der Prüfungskommission:

Dr. Natalie Krivova

Max-Planck-Institut für Sonnensystemforschung Göttingen, Germany

Prof. Dr. Hardi Peter

Max-Planck-Institut für Sonnensystemforschung Göttingen, Germany

Prof. Dr. Andreas Tilgner

Institut für Geophysik, Georg-August-Universität Göttingen, Germany

Prof. Dr. Ariane Frey

II. Physikalisches Institut, Georg-August-Universität Göttingen, Germany

Tag der mündlichen Prüfung:

Contents

Abstract	6
Kurzfassung	8
1 Introduction	9
1.1 Solar photosphere	12
1.2 Solar faculae	14
1.2.1 Facular magnetic fields	14
1.2.2 Facular models and radiation	19
1.2.3 Theoretical models	22
2 Image restoration	27
2.1 Image degradation	28
2.1.1 The Earth's atmosphere	28
2.2 Image restoration methods	30
2.2.1 Adaptive optics	30
2.2.2 Speckle reconstruction	31
2.2.3 Multi-Object Multi-Frame Blind Deconvolution	32
2.3 Restoration of slit-spectra	34
3 Correction of atmospheric stray light in restored slit spectra	37
3.1 Introduction	37
3.2 Residual degradation in ground-based observations	39
3.3 Residual degradation in slit spectra	42
3.4 Estimating the stray-light PSF	44
3.5 Kolmogorov phase screens	45
3.6 Observations and data reduction	45
3.6.1 Image restoration	46
3.6.2 Crosstalk and grey stray light	48
3.6.3 Fried parameter	49
3.6.4 Calculating the stray-light PSF	50
3.7 Results and analysis	52
3.7.1 Effects on RMS granulation contrast	53
3.7.2 Effects on spectra	53
3.8 Discussions and conclusions	56

4	Inversions of slit-spectra	59
4.1	Radiative transfer and spectral line formation	59
4.2	Spectropolarimetric inversions	62
4.3	Introduction to facular bright points	65
4.4	Inversions of facular bright points	66
4.4.1	Temperature	69
4.4.2	Magnetic fields	72
4.4.3	Line-of-sight velocities	73
5	Numerical simulations of faculae	77
5.1	Numerical code and simulation setup	78
5.2	Simulation results	81
5.2.1	Photometric properties of simulated facular bright points	81
5.2.2	Atmosphere in simulated facular bright points	83
5.2.3	Time-distance analysis of facular jets	92
6	Conclusions and outlook	95
	Bibliography	101
	Acknowledgements	115
	Curriculum vitae and publications	117

Abstract

The objective of this thesis is to develop methods to improve the quality of restored ground-based observations, and to use such restored observations, along with 3D radiative MHD simulations, to study the properties of small-scale facular magnetic elements in the lower solar atmosphere. The importance of understanding such structures is derived from studies that report their significant contribution to the total unsigned magnetic flux through the solar photosphere, as well as solar irradiance and variability.

Benefiting from advancements in instrumentation and camera readout speeds, high quality observations (slit-spectra) were collected at the 1-m Swedish Solar Telescope (SST). In addition to a significant wavelength coverage that includes numerous photospheric spectral lines, the high spatial resolution, spectral resolution, and polarimetric sensitivity of the data allow for detailed, fully height stratified spectropolarimetric inversions.

Before the analysis of the ground-based data was undertaken, image restoration methods that correct for different kinds of image degradation were applied to the data in order to ensure that the spatial and spectral distribution of intensities are as close as possible to the true solar values. One such method, extended as part of this thesis, is a stray-light correction procedure, which aims to remove the component of stray light caused by uncompensated high-order wave-front aberrations from the observations. The application of this method was found to improve the granulation contrasts in the slit-spectra, as well as reduce undesirable changes to the shapes of the observed spectral lines caused by stray-light contamination.

Spectropolarimetric inversions were performed using the SPINOR-LTE inversion code, producing maps of the inverted physical quantities as a function of the optical depth. The retrieved atmospheres in the observed faculae were found to be in good agreement with the results of similar studies undertaken earlier, references to which can be found in the introductory chapter. Moreover, several facular bright points were identified in the cores of strong spectral lines. The temperatures, line-of-sight magnetic field strengths and line-of-sight velocities of these bright points were analysed using the inverted maps, however, since slit-spectra do not provide information on the time-evolution of magnetic structures, 3D-MHD direct-numerical-simulations (DNS) of faculae and facular bright points were performed using the MURaM 3D radiative-MHD code. The evolution of the physical parameters in a selected facular bright point was studied using the simulated atmospheres. While some of the atmospheric parameters were found to be similar in some respects with the results of the inversions, the use of high resolution simulations with high cadence also

revealed the possible existence of additional dynamical processes that were seen to participate in and possibly drive the evolution of the bright point.

This thesis is divided into six chapters. In the introductory chapter, a brief account of some of the important studies that analysed the properties of the vector magnetic fields in solar faculae is provided. Emphasis is placed on novel observational techniques and numerical methods that were developed to quantify magnetic field strengths, and orientation in solar faculae. In chapters 3 and 4, attention is drawn to image restoration and its importance in ground-based observations. The chapters include a brief description of the working principle of adaptive optics (AO) and the theory behind the multi-frame blind deconvolution (MFBD) method employed to restore the spectropolarimetric observations. Subsequently, a detailed discussion of the theory of residual stray light arising from uncompensated high-order wave-front aberrations is provided, and a method to remove this residual stray-light contamination from the restored slit-spectra using Kolmogorov phase screens and synthetic, degraded images is described. The final chapters on spectropolarimetric inversions and 3D radiative-MHD simulations briefly introduce the theory behind spectral-line formation, and the equations of compressible, non-ideal magneto-hydrodynamics (MHD), respectively, in addition to describing the setup of the inversions, the choice of the spectral lines, the selection of the physical parameters to be retrieved, and the setup of the numerical simulations and the relevant boundary conditions. In the concluding chapter, the results of the stray-light correction procedure, spectropolarimetric inversions, and the numerical simulations are compiled and sequentially listed. Also, a very brief outlook is given on possible next steps.

Kurzfassung

Die Zielsetzung dieser Arbeit ist die Methodenentwicklung zur Verbesserung der Qualität numerisch rekonstruierter bodengebundener Beobachtungen. Zusätzlich werden solche rekonstruierten Beobachtungen zusammen mit 3D strahlungs-MHD Simulationen verwendet, um die Eigenschaften von kleinskaligen magnetischen Elementen in Fackeln (engl. faculae) der unteren Sonnenatmosphäre zu studieren. Die Wichtigkeit des Verständnisses solcher Strukturen ergibt sich aus Studien, die über deren maßgeblichen Beitrag zur gesamten absoluten magnetischen Flussdichte durch die solare Photosphäre, als auch zur solaren Strahlungsdichte und -variabilität berichten.

Von Fortschritten in der Instrumentierung und den Kameraauslesegeschwindigkeiten profitierend wurden hoch-qualitative Beobachtungen (Spaltspektren) am 1-m Swedish Solar Telescope erhoben. Zusätzlich zu einer erheblichen Wellenlängenabdeckung, welche zahlreiche photosphärische Spektrallinien beinhaltet, erlauben die hohe räumliche als auch spektrale Auflösung, sowie die polarimetrische Sensitivität der Daten, eine detailierte, höhengeschichtete spektropolarimetrische Inversionen.

Bevor die Analyse der bodengebundenen Daten vorgenommen wurde, wurden Bildrekonstruktionsmethoden, welche die unterschiedlichen Arten von Abbildungsfehlern korrigieren, angewendet, um sicherzustellen, dass die räumlichen und spektralen Intensitätsverteilungen so nah wie möglich an den wahren Sonnewerten liegen. Eine dieser Methoden, erweitert im Rahmen dieser Arbeit, ist die Streulichtkorrektur, deren Ziel es ist, die Streulichtkomponente, verursacht durch unkompenzierte Wellenfrontabberationen höherer Ordnung in den Beobachtungen, zu entfernen. Es wurde festgestellt, dass die Anwendung dieser Methode zu einer Kontrasterhöhung der Granulation in Spaltspektren führt, als auch unerwünschte streulichtinduzierte Veränderungen in den beobachteten Spektrallinienformen reduziert.

Spektropolarimetrische Inversionen wurden mit dem SPINOR-LTE Inversionscode ausgeführt und Karten der aus der Inversion erhaltenen physikalischen Größen als Funktion der optischen Tiefe erstellt. Die so gewonnenen Atmosphären in den beobachteten Faculae sind in guter Übereinstimmung mit den Ergebnissen aus früheren ähnlichen Studien, Referenzen dazu können dem Einführungskapitel entnommen werden.

Außerdem wurden einige helle Fackel-Punkte in den Kernen tiefer Spektrallinien identifiziert. Die Temperatur, die magnetische Feldstärke als auch die Geschwindigkeitskomponente in Sichtlinie dieser hellen Punkte wurden anhand der invertierten Karte analysiert. Allerdings, da den Spaltspektren keine Informationen zur zeitlichen Entwicklung der magnetischen Strukturen zu entnehmen sind, wurden 3D-MHD numerische Sim-

ulationen von Fackeln und hellen Fackel-Punkten mit dem MURaM 3D Strahlungs-MHD-Programm durchgeführt.

Die Entwicklung der physikalischen Parameter in einem ausgewählten hellen Fackel-Punkt wurde mit den simulierten Atmosphären untersucht. Während einige der atmosphärischen Parameter in mancher Hinsicht als ähnlich zu den Ergebnissen aus den Inversionen identifiziert wurden, offenbaren die hochaufgelösten Simulationen mit hoher Kadenz auch die mögliche Existenz von zusätzlicher dynamischen Prozessen, welche an der Entwicklung des hellen Punktes teilhaben und diese möglicherweise vorantreiben.

Diese Arbeit ist in sechs Teile unterteilt. In dem Einleitungskapitel wird ein kurzer Bericht einiger wichtigen Studien, die sich mit der Analyse von den Eigenschaften des magnetischen Vektorfeldes in solaren Fackeln beschäftigen, gegeben. Der Schwerpunkt liegt auf neuartigen beobachterischen Techniken und numerischen Methoden, welche entwickelt wurden, um die magnetische Feldstärke und deren Orientierung zu quantifizieren.

In den Kapiteln 3 und 4 liegt die Aufmerksamkeit in der Rekonstruktion von Bildern und die Bedeutung dieser für bodengebundene Beobachtungen. Die Kapitel beinhalten eine kurze Beschreibung des Funktionsprinzips der adaptiven Optik und der Theorie hinter der Methode der multi-frame blind deconvolution (MFBD), welche verwendet wird um die spektropolarimetrischen Beobachtungen zu rekonstruieren.

Anschließend folgt eine detaillierte Diskussion der Theorie des remanenten Streulichts, welches bei unkompensierten Wellenfrontenabberationen auftaucht, und eine Methode zur Beseitigung dieser remanenten Streulichtkontamination aus den rekonstruierten Spalt-spektren mit Kolmogorov-Phasenscheiben und synthetischen, degradierten Bildern wird beschrieben. Die letzten Kapitel über spektropolarimetrische Inversionen und 3D strahlungs-MHD Simulationen stellt jeweils kurz die Theorie hinter der Bildung von Spektrallinien, und die Gleichung der komprimierbaren, nicht-idealen Magneto-hydrodynamik vor. Zusätzlich beschreiben die Kapitel die Konfiguration von Inversionen, die Wahl der Spektrallinien, die Wahl der abgerufenen physikalischen Parameter, und die Konfiguration der numerischen Simulationen mit den relevanten Randbedingungen. Im Schlusswort werden die Ergebnisse der Streulicht-Korrektur, der spektropolarimetrischen Inversionen, und der numerischen Simulationen zusammengefasst und fortlaufend aufgeführt. Außerdem ist ein kurzer Ausblick auf mögliche nächste Schritte gegeben.

1 Introduction

In the context of stellar evolution, the Sun (\odot) is an unremarkable star. Like its peers on the main sequence, the Sun will continue to burn hydrogen for several billion years (Fig. 1.1) before entering the red giant phase. Even at the end of its life, the Sun will fade into a white dwarf. However, being the only star whose surface can be observed in excellent detail, the Sun holds a special significance. At visible wavelengths, the solar surface can be resolved to within one ten-thousandth of the Sun's diameter (~ 70 km with 1-m class telescopes). This has led observers over the course of its observational history to a surprising realization - the solar surface is anything but unremarkable. Instead, it is found to be a spatially structured and dynamic environment that evolves on timescales as short as minutes. However, how is the *surface* defined for a self-gravitating ball of plasma?

Main sequence stars have a hot and dense core where energy from the thermonuclear fusion reactions is primarily released in the form of gamma photons, a small fraction escapes as neutrino flux. Depending on the mass of the star, the fusion reactions may proceed via the $p - p$ chain ($M_\star \sim M_\odot$) or the CNO -cycle ($M_\star > 1.5M_\odot$) with different consequences for the interior structure of the star. In the former case, due to the lack of a steep enough temperature gradient, the core is enclosed by a radiative zone that may extend to a significant fraction of the stellar radius (R). The transport of energy in this zone is chiefly achieved through the gradual diffusion of photons. In the Sun, for example, estimates of the radiative diffusion timescale vary from several thousand years to a million years. Beyond the radiative zone, main sequence solar-like stars have convective envelopes. In these layers, the gas is mechanically unstable to perturbations in radial displacements - pockets of hot plasma that are displaced upwards (direction of increasing radius) become buoyant, quickly developing into bulk motions that transport the energy efficiently to larger radii. This instability is mathematically expressed by the Schwarzschild criterion:

$$\left| \frac{\nabla \ln T}{\nabla \ln P} \right|_\star > \left| \frac{\nabla \ln T}{\nabla \ln P} \right|_{ad} = \left(\frac{\gamma - 1}{\gamma} \right) \quad (1.1)$$

where P is the gas pressure, T is the gas temperature, and γ is the adiabatic index. Therefore, the bulk of convection zones in solar-like stars are characterized by the presence of numerous turbulent convection cells. The dominant photon scattering (or absorption) processes that contribute to the opacity of the gas are bound-free absorption (ionization), free-free absorption (thermal Bremsstrahlung), and Thomson-scattering by free electrons. Although it is difficult to estimate the opacity of the solar interior due to the lack of direct observations, the Kramer's opacity law is thought to be a valid approximation at interme-

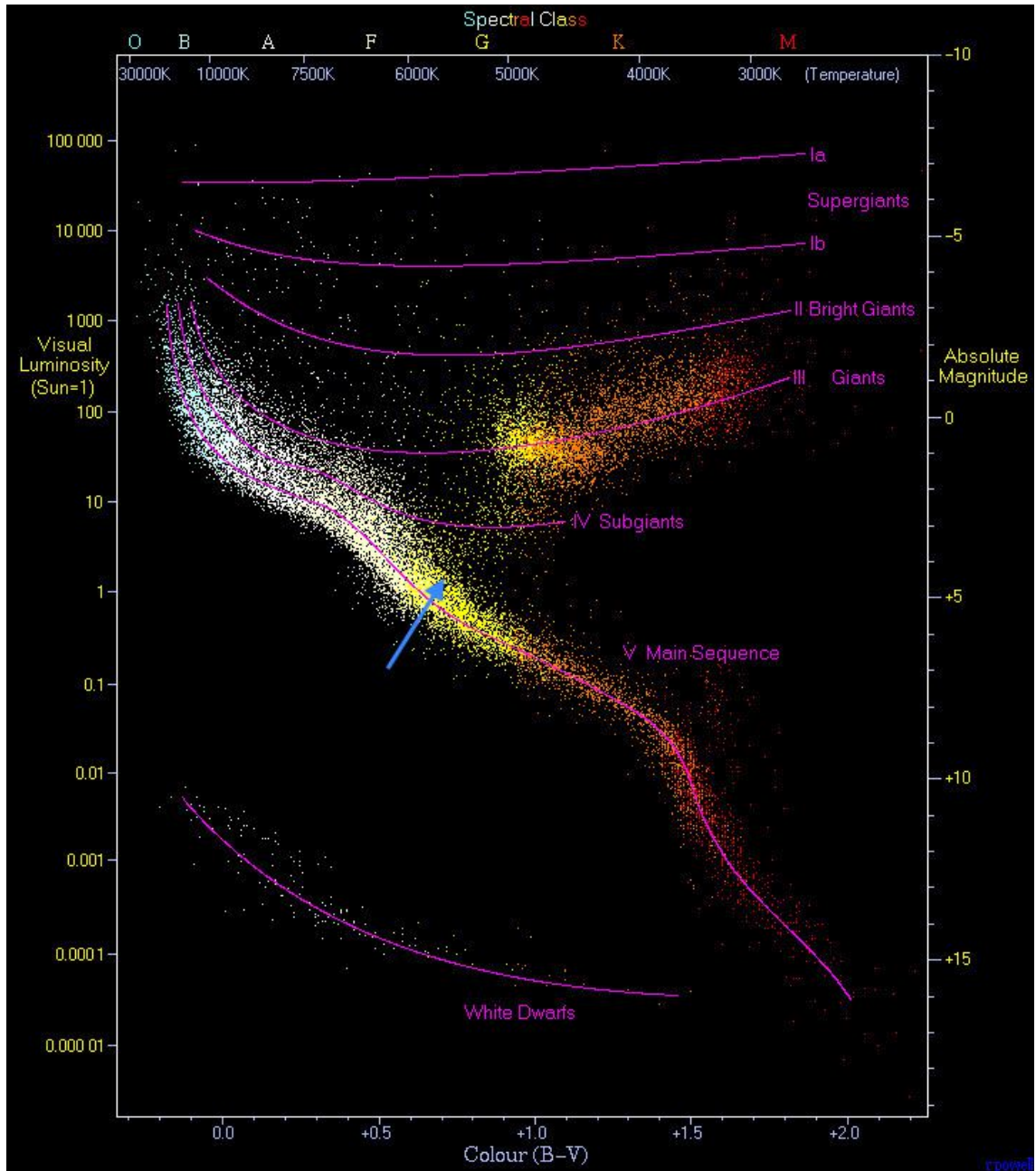


Figure 1.1: Hertzsprung-Russell diagram, showing the main sequence and other asymptotic branches. The Sun (G2V), indicated by the blue arrow, has an estimated life-span of 13 billion years.

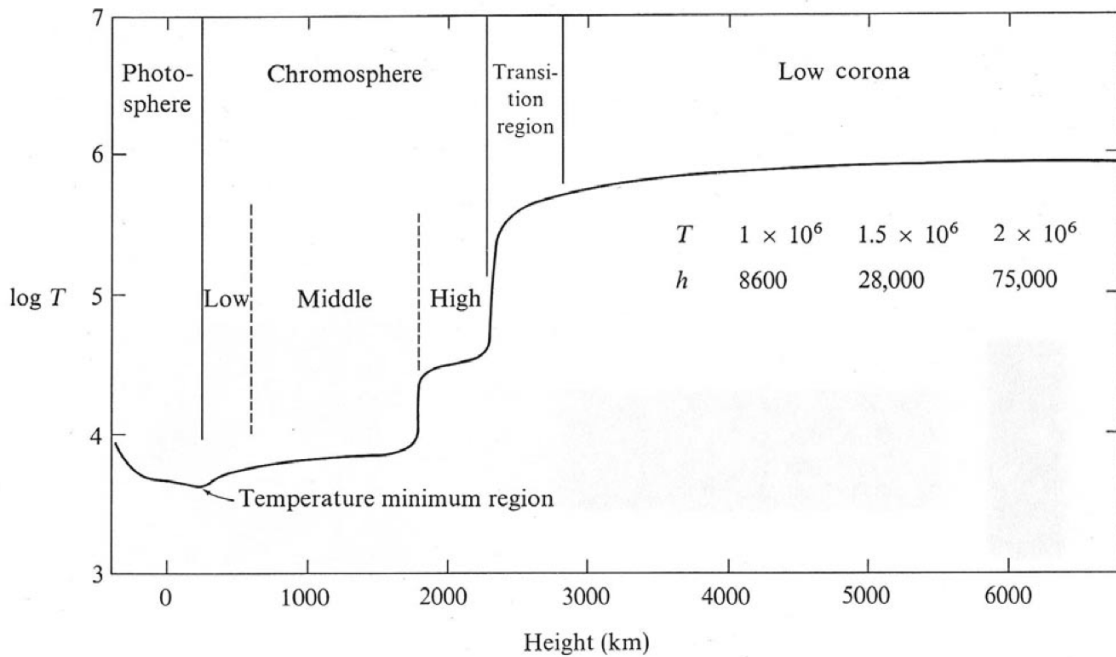


Figure 1.2: Plot of the logarithm of temperature *vs* height. The different idealized layers of the solar atmosphere and their rough boundaries are indicated with respect to the zero-reference height.

diate temperatures:

$$\bar{\kappa} \propto \rho T^{-7/2}$$

where κ is the opacity, ρ and T are the density and temperature of the gas, respectively. Thus, due to very high densities in the stellar interior, the opacity of the gas in the convection zone is sufficiently high to trap the radiation within. However, as the density continues decreasing with radius, the opacity of the plasma is abruptly reduced by several orders of magnitude over a relatively shallow layer, allowing radiation from the turbulent gas to escape into outer space. These last scattering layers become visible to us in images as the stellar surface. Thus, the surface isn't an infinitesimally thin shell, but a region that may be several hundred kilometres thick. On the other hand, the surface is also a strong function of the wavelength (λ) of observations. At specific wavelengths, transitions between different states of excitation of atomic elements may enhance the total opacity of the gas, translating the surface from which photons escape upwards by several hundred kilometers. Depending on the wavelength then, a star is typically associated with multiple surfaces that are geometrically separated in height. By using multi-wavelength observations, these layers in the stellar atmosphere can, in general, be mapped. In the solar case, such observations led to the discovery of the different parts of the solar atmosphere (Fig. 1.2). In order of decreasing radius, these are the solar corona, the transition region, the solar chromosphere, and the solar photosphere, which in an idealized model of the solar atmosphere form shells above the solar surface.

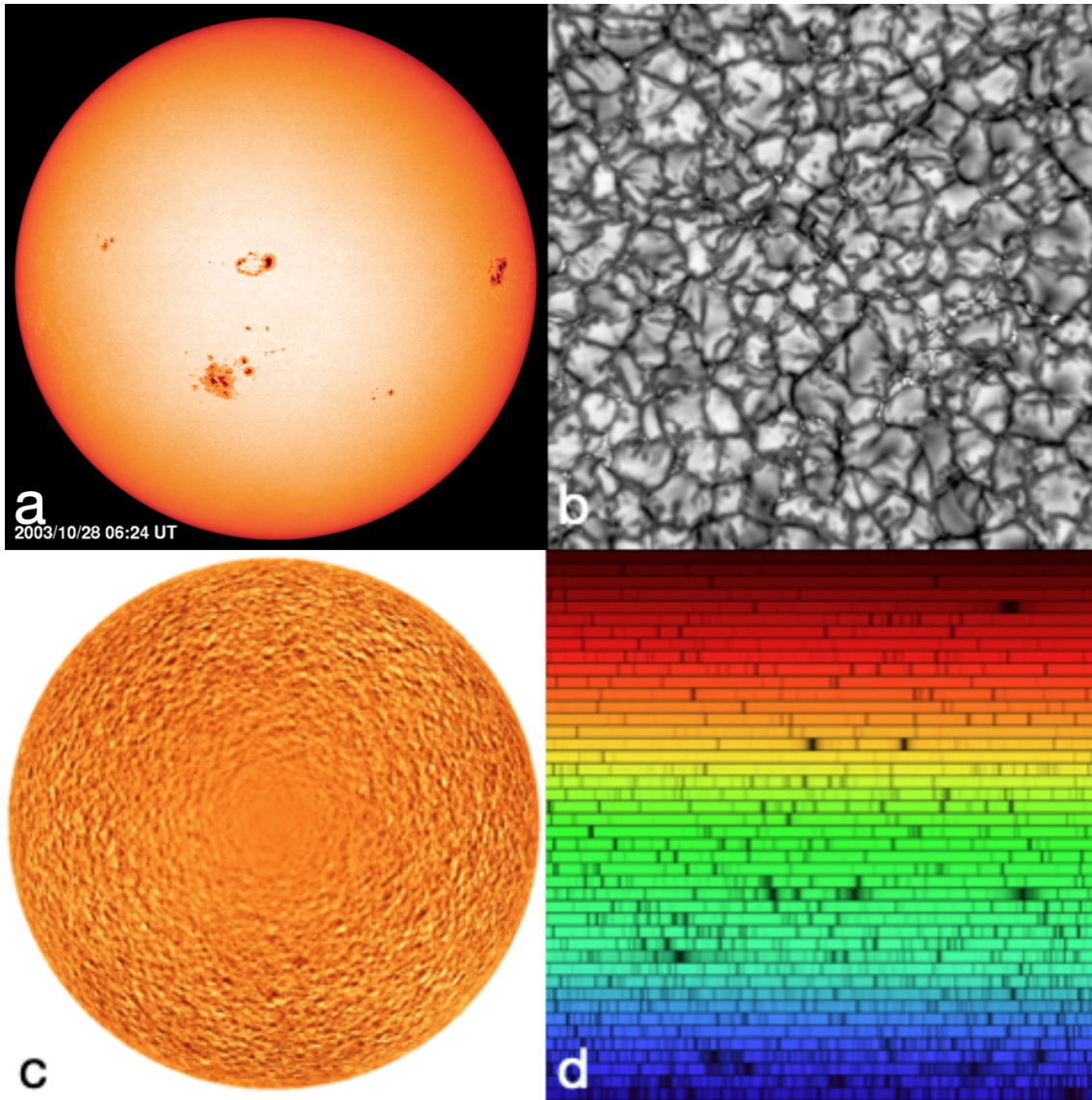


Figure 1.3: Plots of the observed properties of the photosphere. **a.)** Full-disk image of the solar photosphere shown in white light, courtesy NASA **b.)** Magnified image of the photosphere obtained at DKIST **c.)** Full-disk Doppler, courtesy MDI. **d.)** Photospheric spectrum showing hundreds of spectral lines

1.1 Solar photosphere

The solar photosphere is the deepest visible layer of the solar atmosphere. It is usually identified in white-light images or in those taken at continuum wavelengths in the visible region of the electromagnetic spectrum. The photosphere marks the upper boundary of the convection zone, and is conventionally defined as the surface of unit optical depth (τ) at $\lambda = 5000\text{\AA}$:

$$\tau_{5000\text{\AA}} = \int_{\infty}^{R_{\odot}} \kappa_{5000\text{\AA}} dR = 1 \quad (1.2)$$

The photosphere has a long history of observations. It was found in 1610 to feature dark spots that emerged and co-rotated with the Sun at heliographic latitudes near the equator. Throughout the 1800s, the shapes of these spots as well as their trajectories across the solar disk were frequently recorded through drawings or with the help of photographic plates. Moreover, lines in the photospheric spectrum were independently discovered by Wollaston and Fraunhofer, the latter of whom subsequently developed a catalogue of ~ 600 absorption lines - the Fraunhofer lines. The presence of these distinctive photospheric features quickly attracted the interest of several other astronomers. Later in the 19th century, Schwabe, over a period of 43 years of meticulous observations, noted that the spots on the photosphere followed a cyclic variation with a period of roughly ten years, marking the beginning of modern research on the solar cycle. By the beginning of the twentieth century, the association of these spots (sunspots) with strong magnetic fields had been established by Hale, who detected the Zeeman splitting of spectral lines using a spectroheliograph. Thus, the photosphere became an important target of scientific inquiry, prompting countless ground-based and space-based observing campaigns throughout the twentieth century. Through those campaigns, our understanding of the physics of the solar photosphere has dramatically improved.

The photosphere is the dominant source of solar irradiance in the visible region of the electromagnetic spectrum. Its spectrum approximates that of a blackbody with a peak wavelength of 500 nm and an effective temperature of 5770 K . Near the surface, the continuum opacity decreases with a scale height of $\sim 100\text{ km}$, and the convection cells from the interior become visible as a pattern of bright (granules) and dark (inter-granular lanes) structures. Within the granules, pockets of hot gas rise up to the surface and overshoot into the upper atmospheric layers. Due to the lower opacity of the gas, these pockets radiate away a fraction of their internal energy (appearing bright), cooling down and becoming dense in the process. Thus, the inter-granular lanes act as conduits for the mechanical transport of the low-entropy gas back into the solar interior (1.3). The turbulent nature of these bulk fluid motions is reflected in the rapid morphological evolution of solar granulation, as well as their characteristic velocities ($v_{rms} \approx 2\text{ km/s}$). Although, the solar granulation pattern is one of the most easily identifiable features in photospheric images, full-disk Dopplergrams reveal the presence of acoustic waves (for example, the p-mode oscillations) as well as the existence of larger structures of convective origin - the meso-granules ($\sim 10000\text{ km}$ in diameter) and supergranules ($\sim 30000\text{ km}$). These structures are associated with characteristic velocities of 250 m/s , and typically last for several days. Their origin, however, remains unclear due to the lack of direct observations of the solar interior, and is a topic of ongoing research. For a comprehensive review on supergranulation, see Rieutord and Rincon (2010).

On the other hand, analyses of the polarization of photospheric radiation in spectral lines reveal a near ubiquitous presence of magnetic fields that occupy a hierarchy of spatial scales. The largest magnetic structures occur in the form of bipolar active regions (Sect. 1.3) - extensive distributions of magnetic flux that emerge at the mid-latitudes during the beginning of the solar cycle. The magnetic fields in active regions may either be monolithic (pores and sunspots), filamentary (faculae), or both. As the solar cycle progresses, supergranular diffusion and meridional flow, in combination with the Joy's

law, lead to a preferential, poleward transport of the trailing polarity flux over a period of 11-years, becoming the seed fields of the next solar cycle (Mackay and Yeates 2012). However, our understanding of the origin(s) of their magnetic fields and why they emerge onto the solar surface at all is incomplete. Further, active regions are often sites of violent bursts of magnetic energy released in the form of solar flares. While these flares have been studied at extreme-ultraviolet (EUV) wavelengths, what triggers them and how they release their energy is still unclear. On smaller spatial scales, the magnetic flux is distributed into the network and inter-network magnetic fields. The lateral dimensions of these structures is on the order of a few hundred kilometers, and their flux densities are small compared to active regions. Thus, unlike active regions, these fields are much more susceptible to the eviscerating flows of the turbulent convection and consequently have very short lifetimes. Nonetheless, they constitute an important component of solar magnetism as studies have shown that they account for the dominant fraction of the total unsigned magnetic flux. Moreover, the flux in the form of these small-scale magnetic structures is observed to be independent of the phase of the solar cycle, suggesting that the origin(s) of their magnetic fields may be linked to local turbulence-driven dynamo mechanisms. For a comprehensive review on the magnetic fields found outside active regions, see Bellot Rubio and Orozco Suárez (2019).

This thesis focuses on the thermodynamic and magnetic properties of solar faculae. The following sections aim to provide an account of the observational history of faculae, as well as an overview of our understanding of their thermodynamic, and magnetic properties. In solar physics, the terms 'plage' and 'faculae' are now understood to refer to the same constituent magnetic elements. However, in order to stay consistent with conventional nomenclatures, these terms are used in the thesis to refer to the magnetic elements as observed at the chromospheric, and photospheric layers, respectively.

1.2 Solar faculae

1.2.1 Facular magnetic fields

The association between solar plages and magnetic fields can be traced back to the invention of the photoelectric magnetograph (Thiessen 1952, Kiepenheuer 1953, Babcock 1953), which measures the splitting in wavelength of the two σ components of spectral lines in the presence of a longitudinal magnetic field (longitudinal Zeeman effect), yielding an estimate of the field strength after suitable calibration. A comprehensive description of such magnetographs and their associated calibration methods can be found in Beckers (1968). In the years that followed, owing to their high sensitivity, magnetographs became widely used in detecting solar magnetic fields. For example, Babcock and Babcock (1955), over a period of two years, (1952 – 1954) compiled more than 450 magnetograms in the Fe I 5250Å photospheric spectral line obtained at the Mount Wilson observatory. In their observations, they discovered a weak 'general field' at high heliographic latitudes in either hemisphere with a slit-averaged deduced longitudinal field strength of 1 Gauss. In the lower latitudes, however, stronger fields were observed to be co-spatial with the bright structures (solar plages) in Ca-II and H α spectroheliograms.

Howard (1959) and Leighton (1959) later made similar comparisons using magnetograms in the Fe I 5250Å and Ca I 6103Å lines, respectively, but with much higher angular resolution. They too arrived at the conclusion that the observed brightness distributions in chromospheric spectroheliograms were fundamentally related to magnetic fields. Thus, plagues soon came to be understood as filamentary distributions of magnetic flux with possible fine structure (see Severny 1964, for a review). However, the effects of a number of factors such as the spatial resolution, atmospheric seeing, and systematic changes to the line profiles on the deduced field strengths remained unknown or unclear.

The first investigation into the effects of spatial resolution was made by Stenflo (1966) at the Crimean observatory. He obtained magnetograms in the Fe I 5250Å line of several 60'' × 60'' regions near the solar poles, with spectrograph slits of four different sizes (2'' × 27'', 2'' × 9'', 3'' × 4.5'', and 3'' × 2.3''). In his study, he found the slit-averaged magnetic flux to be larger for smaller slits, and vice-versa. If the magnetic regions contain unresolved fields of mixed polarity, this trend, he argued, would follow due to the partial cancellation of the net Stokes V signal over the slit. Further, Stenflo (1966) also showed that such partial cancellation effects are made worse by the combination of image motions due to atmospheric seeing, and the integration of the signal over the time-constant of the magnetograph. Thus, the true longitudinal field strengths of magnetic regions were likely to be underestimated when observed with low angular resolution.

In parallel, in the late 1960s, numerous Fraunhofer lines were observed to weaken in relatively strong non-sunspot magnetic fields (Sheeley 1966, 1967, Howard 1967, Chapman and Sheeley 1968). Although this was initially attributed to the Zeeman-splitting of the line, Chapman and Sheeley (1968) argued that it was not the dominant factor due to the following reasons. Firstly, irrespective of the magnetic sensitivity of their observed spectral lines, the Zeeman-splitting due to an assumed field strength of 500 gauss (which was considered strong) was found to produce insufficient weakening when compared to the observations. Secondly, the observed weakening was found to be inversely correlated with the ionization potential of the atomic species - lines corresponding to singly ionized species were marginally affected compared to neutral atoms. Thus, based on calculations of the number density of the atomic species from the Saha-Boltzmann equation, Chapman and Sheeley (1968) concluded that the weakening must also be driven by the local temperature. The implications of this to the measurement of magnetic fields were further discussed by Harvey and Livingston (1969), who obtained simultaneous magnetograms in several pairs of spectral lines at a time. In their analysis, they noted that the deduced field strengths were similar only when the line-pair weakened identically, and different otherwise. Thus, correction factors between 2 – 5 were suggested to the field strengths estimated using particularly temperature sensitive lines like the Fe I 5250Å.

On account of these systematic errors, the deduced field strengths of small-scale magnetic elements were reported with considerable scatter. Thus, Sheeley (1966) found longitudinal field strengths varying from 200 – 700 gauss, while Sheeley (1967) reported absolute field strengths of 350 ± 50 gauss, by measuring the center-of-gravity shifts of the σ components in the magnetically sensitive Fe I 5250Å line. These reports of relatively strong non-sunspot magnetic fields were confirmed in subsequent investigations by Beckers and Schröter (1968), Grigorjev (1969), and Harvey et al. (1972), the last of whom used the theory developed by Unno (1956) to produce fits to the observed Stokes

V profiles (among the first precursors to spectropolarimetric inversions).

An important method that allowed the detection of unresolved strong fields was proposed by Stenflo (1973), using the technique of line-ratios. In their method, a pair of spectral lines with different sensitivities to the magnetic field, but which otherwise form at approximately the same atmospheric layers are selected. For example, the Fe I 5250Å and the Fe I 5247Å lines satisfy this requirement - they belong to the same multiplet, have similar line strengths, but different Landé factors (g_{eff}). Thus, in an observed region with weak magnetic fields, the ratio of their Stokes V amplitudes (normalized to Stokes I) is proportional to the ratio of their g_{eff} . However, if the magnetic fields are strong, the line with the larger g_{eff} becomes Zeeman-saturated (i.e. its Stokes V amplitude stops growing with field strength) and the ratios would deviate appreciably from their nominal values. By measuring these deviations, an estimate of the peak magnetic field strength in the resolution element can be derived. Stenflo (1973), using the line-pair described above, applied the technique to observations of the photospheric network in a quiet Sun region and deduced fields as strong as 2000 – 2400 gauss. The existence of such strong kilogauss fields were subsequently confirmed in several independent studies. Harvey and Hall (1975) used the Fe I 15648Å ($g_{\text{eff}} = 3.0$) infrared line to obtain strengths of 1500 – 2000 gauss. Wiehr (1978) extended the line-ratio method to three relatively temperature insensitive lines - Fe I 6302Å, 6336Å, and 6408Å - and obtained strengths of 1200 – 1700 gauss. They found higher values of 1500 – 2200 gauss using another method with three exit slits in the Fe I 6173Å line. Further studies by Tarbell and Title (1977), Koutchmy and Stellmacher (1978), and Solanki and Stenflo (1984) confirmed an emerging picture that magnetic fields in the solar atmosphere do not form a continuous distribution in field strength, but are rather strongly concentrated. However, inferences of the geometry of these magnetic fields became possible only after the development of better instruments and more sophisticated analysis techniques.

In the late 1970s, the Fourier Transform Spectrometer (FTS, Brault (1978) at the Kitt Peak McMath-Pierce solar telescope was equipped with a polarimeter (see e.g. Baur et al. 1980, 1981) that could simultaneously record both the total intensity (Stokes I) and the circular polarization (Stokes V) component. Although the spatial resolution of the FTS spectra was typically poor, the very high spectral resolution, signal-to-noise ratio (SNR), and the large wavelength coverage made statistical studies of numerous strong and weak spectral lines possible. Thus, Stenflo et al. (1984) obtained FTS spectra covering a wavelength range of $\sim 1000\text{\AA}$ that included several well known chromospheric (Na I D₁ 5895Å and D₂ 5889Å, H β 4861Å) and photospheric (Fe I 5250Å, Fe I 5247Å) spectral lines. Their observational targets included plages and network magnetic fields at the disk center. In the Stokes V spectra, they found systematic asymmetries between the blue and red lobes in several unblended lines, while their zero-crossing wavelengths were close to the nominal line-center on average. This led them to conclude that the magnetic elements in plages may harbour strong gradients in line-of-sight velocities (v_{los}), in sharp contrast to the prevailing theoretical models that assumed hydro-staticity. Stenflo et al. (1984) additionally used their observations to test the validity of the weak-field approximation, as well as identify lines where the LS-coupling approximation failed.

A similar, but complementary study was undertaken by Solanki and Stenflo (1984)

using observations covering 400 Fe I spectral lines from the same instrument. However, in addition to quantifying the amplitude and area asymmetry of the Stokes V lobes, Solanki and Stenflo (1984) also numerically synthesized spectra of hypothetical Fe I lines with different atomic parameters, corresponding to a set of magneto-hydrostatic model atmospheres. By comparing the line-depths and the broadening of the observed lines with synthetic lines, they too verified that magneto-hydrostaticity may be an insufficient approximation of the atmospheres in magnetic structures. Although such studies highlighted the existence of complex sub-structures in magnetic elements, they were unable to circumvent the degeneracy with which the temperature, magnetic field, line-of-sight velocity, and turbulent velocities affected the shapes of spectral lines. Consequently, the development of a more formal technique - spectropolarimetric inversions - quickly gained importance (see Chapter 4).

Auer et al. (1977) were among the first to develop a numerical code that retrieved the atmospheric parameters using a least-squared (χ^2) minimization method, with the assumption that the atmospheric parameters varied linearly with optical depth (Milne-Eddington approximation). A similar inversion code was implemented by Keller et al. (1990) to retrieve the temperature and magnetic field of the plages in the same observations collected by Stenflo et al. (1984). In agreement with the facular models, they found the magnetic field strengths to decrease with geometrical height - from 2000 Gauss at $\log(\tau) = 0.0$ to 500 Gauss at $\log(\tau) = -3.0$. Although earlier magnetograms of different spectral lines had already established this property (since different lines form at different layers), their study was among the first to confirm the result using the method of inversions.

In the following years, telescopes were equipped with better polarimeters that could simultaneously record the full Stokes spectra, making spectropolarimetric inversions the diagnostic method of choice. Although inversion codes still used the Milne-Eddington approximation due to computational limitations, it became possible to retrieve the complete vector magnetic field. Thus, Martínez Pillet et al. (1997) used the Advanced Stokes Polarimeter (ASP) at the Vacuum Tower Telescope (VTT) to observe a number of active regions at various heliocentric angles. Their data was obtained with a spatial resolution of $1''$, covering the well-known Fe I 6301Å ($g_{\text{eff}} = 1.5$) and Fe I 6302Å ($g_{\text{eff}} = 2.5$) spectral lines. For the inversions, they used the Milne-Eddington inversion code developed by Skumanich and Lites (1987). Further, the spectra emerging from any given pixel within the FOV were assumed to be an admixture of two independent atmospheres - a magnetic component parametrized by α , and a non-magnetic component parametrized by $1 - \alpha$. The filling factor α represented the fraction of a possibly unresolved pixel that was magnetized, and was another free parameter to be constrained by the inversion code. The use of such filling factors was considered necessary to circumvent the issue of unresolved fields, especially in foreshortened faculae appearing close to the limb. In the maps of the atmospheric parameters retrieved by their inversion code, Martínez Pillet et al. (1997) observed that the magnetic fields in faculae, both near and away from the disk center, were almost vertical with respect to the local solar surface. The most probable value of the distribution of their deduced inclination was found to be 10° , with a Full-Width Half Maxima (FWHM) of roughly 20° . This was consistent with theoretical models (see Chapter 1.2) and the results of other independent observational studies, for example, by

Bernasconi et al. (1994). For the azimuth of these magnetic fields, no preferred direction was observed. However, given that their inversion code was Milne-Eddington based, the variations of the magnetic fields with height were instead investigated by studying them as a function of the heliocentric angle (μ). At disk center, the most probable value (mode) of the distribution of field strengths was found to be 1.4 kilo-Gauss with an FWHM of 300 Gauss. While the stronger fields (> 1 kilo-Gauss) were nearly vertical, the weak field regions (< 500 Gauss) were equally likely to be horizontal. On the other hand, the mode of the distribution of field strengths was found to decrease for plages located close to the limb. Combined with prior theoretical and observational studies, these results formed the basis of what is still held to be generally true regarding the nature of small-scale magnetic elements:

- They occur mostly in the strong-field form, contributing to more than 90% of the total unsigned flux through the photosphere (Frazier and Stenflo 1972).
- Their magnetic fields rapidly expand with height above the photosphere, some of which even reach coronal heights (Simon and Noyes 1971).
- They have a substructure that is unresolved with a spatial resolution of 1'' (Mehlretter 1974).
- The smallest magnetic structures are ephemeral, often having lifetimes comparable to the granulation timescales (Dunn and Zirker 1973).
- The magnetic fields are typically normal to the surface at the photosphere (Martínez Pillet et al. 1997). Determining the variation of their inclination with height, however, required further observations with better quality data, and more sophisticated analysis methods.

Further advances in our understanding of their geometrical structure were driven by improvements in the spatial resolution of observations, instrumentation and observational techniques, as well as computational capabilities. Numerical codes were developed to retrieve the atmospheric parameters as a function of $\log(\tau)$ (full stratification) at select optical depths (see Chapter 4). Consequently, better fits were produced for the asymmetries in the observed spectra in Stokes I and Stokes V, boosting confidence in the constraints set by such codes to the inverted physical parameters. Thus, Buehler et al. (2015) used the SPINOR-LTE code (Frutiger et al. 2000a) to invert spectropolarimetric observations of active region plages taken with the Hinode SOT/SP (Tsuneta et al. 2008, Suematsu et al. 2008, Ichimoto et al. 2008, Shimizu et al. 2008). Unlike earlier studies, the retrieval of independent atmospheric maps at $\log(\tau_{5000}) = 0.0, -1.0, -2.3$ allowed them to directly *see* the expansion of the magnetic field without recourse to theory. By applying a threshold to the maps of the magnetic field strengths at all optical depths, Buehler et al. (2015) found good agreement between the observed expansion of the field in select magnetic elements and the semi-empirical thin fluxtube models constructed earlier (see Sec. 2.2.2). Moreover, in the center of magnetic elements, they found the magnetic fields to be nearly vertical and the strongest (> 1.5 kilo-Gauss at $\log(\tau_{5000}) = 0.0$) at all optical depth nodes. In the fringes of the magnetic elements, however, the weaker expanding fields were often

found to be co-spatial with strong downflows at the lower nodes. These fringe regions were verified to be the source of the amplitude and area asymmetries of the Stokes V lobes, since the line-of-sight intersects the interior of the fluxtubes at the upper nodes and the field-free exterior of the fluxtubes at the lower node, confirming earlier findings by Grossmann-Doerth et al. (1988) and Solanki (1989). On the other hand, the inhibition of convection by the strong magnetic fields of the plage (see for e.g. Narayan and Scharmer 2010) was also confirmed in the line-of-sight velocity maps at $\log(\tau_{5000} = 0.0$, where regions with the strongest fields - such as in the core of the magnetic elements - tended to have plasma line-of-sight velocities that were close to zero.

1.2.2 Facular models and radiation

In the previous section, some of the important observational studies on the magnetic nature of solar faculae were introduced, along with a brief discussion on the analysis techniques. The focus of this section, however, is to provide an overview on the two broad categories of facular models - semi-empirical models that were constructed with the aid of observations, and purely theoretical models that were validated by numerical simulation. The section also introduces the radiative characteristics of faculae, both from an observational and theoretical perspective.

1.2.2.1 Semi-empirical models

In the early semi-empirical models, faculae were conceived as vertical columns of magnetic field embedded in a field-free photosphere. The atmospheres in both the faculae and the photosphere were considered to be plane-parallel, and the gas was thought to exist in hydrostatic equilibrium (Fig. 1.4). One of the key methods of constructing facular models was to use the center-to-limb variation (CLV) of the intensity contrasts of faculae at continuum wavelengths, as well as in the cores of spectral lines. For example, Chapman and Sheeley (1968) used the broadband observations of Rogerson (1961) to calculate the contrasts of observed faculae as a function of their heliocentric angle (μ). This CLV, and by extension the facular limb-darkening, were inverted to obtain a preliminary stratification for the temperature ($T(\tau_\lambda)$) from which the stratification of the gas pressure, the electron pressure, and the opacity were iteratively computed by integrating the equation of hydrostatic equilibrium. For the initial stratification of these quantities, the reference Bilderberg Continuum Atmosphere (BCA, Gingerich and de Jager (1968)) was chosen. Finally, since they considered a facular atmosphere of a finite lateral size, Chapman (1970) additionally modified the stratification of the temperature through trial and error to ensure that the observed facular contrasts at the limb ($\mu < 0.2$) matched the numerically synthesized values. Thus, they arrived at an atmosphere that was cooler than the quiet Sun in the photosphere by approximately 300 K. The temperature was then found to equal the quiet Sun at $\log(\tau) = -0.8$ before exceeding it by approximately 900 K at $\log(\tau) = -1.0$.

However, the effects of scattered light and low spatial resolution contributed to a large scatter in the observed CLVs (see e.g. Schmahl 1967, Chapman 1970, Frazier 1971), causing the constructed facular models to become incompatible with observations of the line-profiles i.e. the temperature excess in faculae indicated by the weakening in the cores

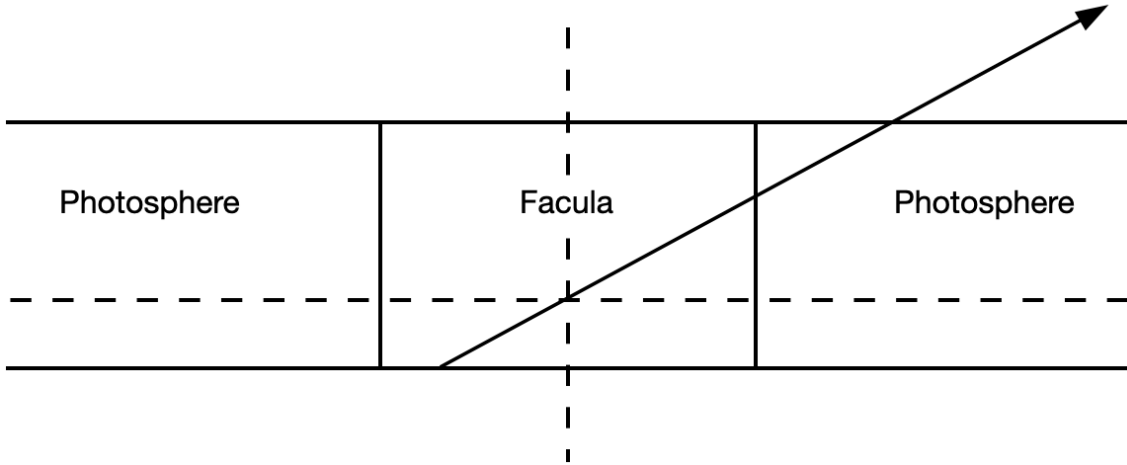


Figure 1.4: Sketch of the facular model of Chapman (1970). The facular contrasts were computed as a function of μ by calculating the emergent intensity of a ray passing through the multiple (facular and photospheric) atmospheres.

of Fraunhofer lines was much less than that computed from the CLV studies (Stellmacher and Wiehr 1971, 1973, Caccin et al. 1974). In order to bring the two studies into parity, Chapman (1977) studied the effects of scattered light and strong magnetic fields on the line-profiles. In his analysis, he considered the observed spectra in their resolution element to be a mixture of spectra from the faculae as well as the surrounding photosphere:

$$I_{obs} = \alpha I_{ph} + (1 - \alpha) I_f \quad (1.3)$$

where I_{obs} is the photospheric spectrum, I_f is the facular spectrum, and α parametrizes the fraction of scattered light from the photosphere in the resolution element. Thus, a set of spectra were generated for existing models of the faculae (with prescribed stratification of the temperature) with both α and B , the magnetic field in the faculae, tuned such that the central intensity of the synthetic facular spectra matched that of the observed spectra of eight independent spectral lines simultaneously. The atomic parameters of the chosen spectral lines were each independently calibrated using the reference HSRA atmosphere (Gingerich et al. 1971) and the observed line-profiles of the quiet Sun, assuming local thermodynamic equilibrium (LTE). With the chosen setup, they found that a large fraction of the observed spectra was likely contaminated by scattered light from the quiet Sun ($\alpha \approx 0.6$). Correcting the apparent deduced longitudinal fields for this scattered light yielded actual field strengths of upto 2.4 kilo-Gauss, similar to the independent estimations of Stenflo (1973).

Further refinements to the semi-empirical facular models were proposed by Chapman (1979) (Fig. 1.5), who included a stratification of the magnetic field in the same method followed by him earlier (Chapman 1977). While the pressure due to the magnetic field was added to the internal gas pressure in the equation describing horizontal pressure equilibrium, he neglected the curvature forces, arguing that significant errors are introduced only at the upper layers of the atmosphere:

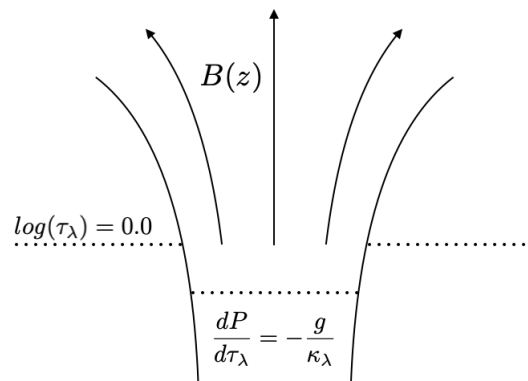


Figure 1.5: Sketch of the updated facular model of Chapman (1979). The dotted line represents the $\log(\tau) = 0.0$ layer, which is now depressed within the faculae, and the magnetic field strength varies with height (z).

$$P_e(z) = P_i(z) + B^2(z)/2\mu_0 \quad (1.4)$$

where P_e , p_i are the external and internal gas pressure, respectively, and B is the magnetic field in the faculae. In order to maintain pressure equilibrium at equal geometric heights, the facular model was shifted downwards such that $P_i < P_e$ at each depth (z). The above equation was then inverted to retrieve both the magnetic field as a function of the depth, as well as the radius ($R(z)$) assuming a cylindrical field region with a flux of ($\phi = 4.4 \times 10^{17}$, Mehlretter (1974)). However, an important limitation of the semi-empirical models described above were that they exclusively relied on measurements of the total intensity, but not the polarization intensities (Stokes Q, U, V). Thus, fewer observational constraints were available, preventing an adequate resolution of the intrinsic degeneracy between different physical factors (filling factor, field strengths) that could produce, in principle, the same Stokes I spectra. Subsequent improvements to semi-empirical models of fluxtubes based on the Stokes profiles were later pioneered by Stenflo (1975) and Solanki (1986), the latter of whom used FTS spectra with several hundred spectral lines.

While the CLVs of facular contrasts continued to be investigated (see for e.g. Foukal et al. 1981, Chapman and Klabunde 1982), other authors attempted to characterize the line-of-sight velocities in magnetic elements. However, a number of contradictory results were often obtained and the existence of systematic flows in facular elements remained unclear. Giovanelli and Slaughter (1978) computed the zero-crossing wavelengths of the Stokes V spectra in isolated magnetic elements and plages from observations made with photospheric (Fe I 8688Å, C I 9111Å) and chromospheric (Mg I 5183Å) spectral lines, respectively. While they found no mean v_{los} in the chromospheric layer, redshifts of up to 1.6 km s^{-1} were reported at the photosphere. Using the height range spanned by the formation layers of these lines, they reasoned that for a downflow to persist for the observed lifetimes of $\sim 2 \text{ h}$, matter near the temperature minimum region would have to be continuously fed into the magnetic structures from the non-magnetic surroundings. Similarly, stronger redshifts of up to 2 km s^{-1} , detected with the Ca^+ spectral line using the same method, were hypothesized to be evidence of the convective collapse mechanism

(Spruit 1979) by Wiehr (1985).

Contradictory results were produced by investigations of systematic downflows made with FTS spectra. For example, Solanki (1986) used two methods to determine the existence of flows in magnetic elements - the zero-crossing wavelengths of the Stokes V profiles, as well as the broadening of the Stokes I profiles. Since with the FTS, the spectra are integrated in time, the former method is mainly sensitive to persistent uni-directional line-of-sight velocities spanning multiple layers of the magnetic structures. The latter method, however, is more sensitive to gradients in line-of-sight velocities (which broaden the spectral lines), as well as oscillations. In his study, Solanki (1986) found an upper limit of 250m/s for global flows in either direction along the line-of-sight in both plages and network elements, an indication that siphon flows, such as those proposed by Giovanelli and Slaughter (1978), may not exist for long periods of time in magnetic elements. However, his study did not preclude the existence of mass motions on shorter time-scales like propagating waves and the five minute oscillations, as he reported that it was necessary to include a microturbulent and/or a macroturbulent velocity in order to reproduce the observed broadening of spectral lines.

Further, to study the disparity between the results of Solanki (1986) and Giovanelli and Brown (1977), Giovanelli and Slaughter (1978), Wiehr (1985), Solanki and Stenflo (1986) simulated the effects of a finite entrance slit and grating resolution on the Stokes V spectra. With decreasing resolution, they found that the spectral smearing of an intrinsically asymmetric Stokes V profile introduced spurious shifts in its zero-crossing wavelengths - the worse the spectral resolution, the larger the redshift. The effect was verified again for the line-center-magnetogram technique of Giovanelli and Ramsay (1971) on which the study of Giovanelli and Slaughter (1978) relied. Similarly, the study was repeated for the chromospheric Mg I b_1 line of Giovanelli and Slaughter (1978). Again, the finite slit width was found to produce fictitious shifts in the doppler velocity exceeding the mean v_{los} reported by them. Thus, they argued that on account of these instrumental factors that were unknown in earlier studies, the results of the earlier studies are compatible with the limit of mean 250 m/s reported by Solanki (1986).

1.2.3 Theoretical models

In the photosphere, a fraction of the gas exists as ionized plasma - including several species of ions and free electrons. Due to the high density, however, the collision rate between the different ions and neutral atoms is high enough so that the theory of single-fluid ideal magneto-hydrodynamics (MHD) holds. For an isolated strand of weak magnetic field that is introduced into the turbulent gas, the coupling of the field with the ions (Lorentz force back-reaction) causes the bulk motions of the fluid to drag the field lines with them - Alfvén's frozen flux scenario (Alfvén 1942). The dragging of field lines is especially effective in small-scale magnetic structures whose field strengths are too weak to arrest the turbulent motion of convection. They consequently act as tracers of the lateral motion of solar granulation, eventually accumulating in those regions where the flow fields on the surface converge i.e. intergranular lanes, and boundaries of super-granules on larger scales (see for e.g. Leighton et al. 1962, Parker 1963, Simon and Leighton 1964). At these locations, the field lines are concentrated until horizontal pressure equilibrium

with the surrounding photospheric gas is reached, leading to the formation of flux concentrations whose field strengths are determined by the equipartition between the magnetic energy density and the kinetic energy density of the gas.

In early analytical studies, the role of numerous physical processes were investigated in understanding the observed field strengths. For example, a field strength of 500 Gauss corresponds to a magnetic pressure of 10^4 dynes cm^{-2} , compared to a gas pressure of $NkT = 10^5$ dynes cm^{-2} at the photosphere i.e. either the external gas must confine the magnetic fields, or the fields must exist in a force-free configuration. The latter scenario was excluded by Parker (1976a), who showed that a force-free configuration of the field produces insufficient magnetic flux through the magnetic elements, compared to observed estimations. Thus, dynamical mechanisms such as turbulent pumping (Parker 1976b), and the Bernoulli effect (Parker 1974) were suggested as the primary ways by which fields in fluxtubes are enhanced to several hundred Gauss. However, the discovery of kilo-Gauss fields that soon followed presented additional challenges that could not be addressed by these mechanisms. The first attempt at resolving the conundrum was made by Parker (1978), whose theory is as follows. Consider a slender magnetic fluxtube with a field strength that is strong enough to inhibit convection within the fluxtube. That is, the lateral heat transport coefficient of convection is reduced by several orders of magnitude (10^4), so that the gas is well insulated from the ambient gas of the surrounding field-free regions at sub-surface layers. In such a case, a downward displacement of the gas within the fluxtube leads to an adiabatic increase in its temperature, in contrast to a superadiabatic increase that a similar displacement would produce in the field-free convecting region at the same depth. Thus, if systematic downdrafts in the fluxtube exist, Parker (1978) argued that they would cause a partial evacuation of the gas within the fluxtube at the photosphere, and that the magnetic fields there would intensify to compensate for the reduced gas pressure in the fluxtube. The latter argument trivially follows from the assumption of pressure equilibrium. Further, Parker (1978) also presented theoretical calculations to show that the lateral heat transfer from the surrounding convecting regions is too inefficient to heat the descending gas in the downdrafts fast enough. Consequently, he concluded that this *superadiabatic effect* is a likely mechanism for enhancing magnetic fields from a few hundred Gauss to kilo-Gauss values.

However, the theory above did not explicitly discuss the initial field strengths, or their regimes, for which the *superadiabatic effect* was purported to occur. This was addressed by Spruit (1979) and Spruit and Zweibel (1979), who studied the stability of a slender magnetic fluxtube (Defouw 1976, Roberts and Webb 1978) as a function of their initial field strength using linear stability analysis. In their study, they found the important result that adiabatic perturbations in the vertical displacement of the gas are unstable if the initial field strength of the fluxtube is less than 1270 Gauss. The fluxtube is, thus, *collapsed* into a new equilibrium state with a higher field strength, smaller cross-section, and lower energy. This convective collapse is now thought to be the primary mechanism that causes kilo-Gauss fields in magnetic elements.

The construction of the fluxtube model also proved indispensable in explaining the excess brightness of limb faculae (Fig. 1.6). In his analytical study, Spruit (1976) considered the pressure and energy balance between the fluxtube and the photosphere. His

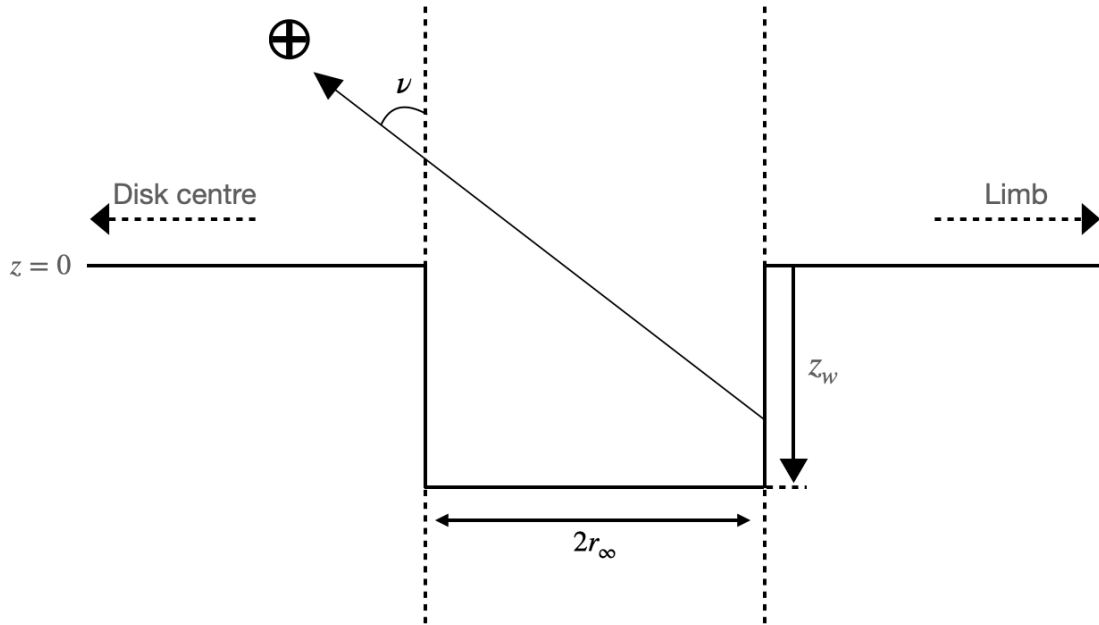


Figure 1.6: Schematic of the hot-wall effect (Spruit 1976). Radiation from the walls of the faculae propagates freely into the line-of-sight indicated by the cross-hair.

model is as follows: For an embedded fluxtube, pressure equilibrium at the photospheric layer lowers the density within the tube at equal heights. Consequently, the opacity of the gas is also reduced, causing a depression of the $(\log(\tau) = 0)$ surface (Wilson depression). For small fluxtubes ($r < 300 \text{ km}$), the reduction in this opacity allows radiation from the walls of the neighbouring granules to propagate and heat up the interior. This heating is particularly efficient when the radius of the fluxtube approaches $\sim 100 \text{ km}$. Regardless, for a tube that is viewed at an oblique angle, the line-of-sight eventually intersects the wall of the limbward granule adjacent to the magnetic structure. If the degree of opacity reduction is larger (a factor determined by the strength of the magnetic field), the brightness of the limbward granule is also higher. This 'hot-wall effect' (Fig. 2.6) is currently thought to be the reason for the brightness of limb-faculae.

Since the 1980s, the development of the theory of magnetohydrodynamics and radiative transfer spawned numerous studies based on direct-numerical-simulations (DNS). Such simulations came to be routinely used in investigating the relevant radiative and MHD processes that imparted the observed characteristics to faculae and other small-scale magnetic elements. Initially, due to computational limitations, 1D-MHD simulations were used to study the variation of the field strength, velocity, and temperature as a function of height in fluxtubes. Although such simulations were simplistic, they played an important role in verifying the physical theories developed thus far. For example, the 1D-MHD simulations by Sirajul Hasan (1984), and Hasan (1985) provided immediate confirmation of the convective collapse mechanism. Beginning with an initial field of 400 Gauss at the photosphere, they found that the instability quickly established a final mean field strength of 1400 Gauss. However, in their simulations, the final solutions of $B(z)$, $v(z)$, and

$T(z)$ exhibited oscillations in time with amplitudes as large as 400 Gauss, 1 km s^{-1} , and 500 K, respectively. Subsequent investigations by Takeuchi (1993), however, attributed the oscillations to the closed boundary conditions (no mass exchange) adopted by Sirajul Hasan (1984). These studies were soon followed by more sophisticated 2D-MHD simulations using a slab-geometry. Thus, Deinzer et al. (1984), and Knoelker et al. (1988) provided key verification of the temperature, field strengths, and their stratification. Further confirmation of the observed properties were provided by Grossmann-Doerth et al. (1998), who were able to reproduce the Stokes V amplitude asymmetries observed by Stenflo et al. (1984) in spectra synthesized from their simulations. On the other hand, Steiner et al. (1998) studied the interaction of the fluxtubes with the photospheric granulation. They presented and discussed several dynamic, hitherto unknown, phenomena such as shocks, persistent downflows at the fluxtube-granule interface, considerable fine-scale structure in the magnetic element, and vigorous buffeting of the fluxtube due to turbulent convection. These characteristics have been verified in the more sophisticated 3D-MHD simulations by Vögler et al. 2005. Vögler and Schüssler (2003), Vögler et al. (2005a), Keller et al. (2004), Carlsson et al. (2004), the latter of whom were also able to explain the excess brightness of faculae observed at an oblique angle for the first time. However, since simulations are typically performed with a grid-spacing that far exceeds the best resolution available in observations, the fine-scale structure and characteristics pertaining to the dynamic nature of solar magnetic elements await confirmation from observational studies.

2 Image restoration

For any distant astrophysical object, the only measurable quantity is its instantaneous spectrum i.e. intensity as a function of wavelength. This is achieved using a spectrograph and a detector, for example. If a polarimeter is used, the state of its polarization (Stokes vector) can also be recorded. In the solar case, however, two additional degrees of freedom are available:

$$I_{\odot}^{inst} \cong I(x, y, \lambda) \quad (2.1)$$

where (x, y) is the two-dimensional position on the solar disk, λ is the wavelength, and I^{inst} denotes the instantaneous intensity. The equation above lists the independent variables that this intensity could theoretically be a function of. However, in practice, since the detector is two-dimensional, either a spectrum or an image can be obtained at any given time. Thus, in spectrographs, a slit is used to disperse the incident beam through a prism or a diffraction grating. The dispersed spectra, therefore, represent the instantaneous intensities of a thin strip of the solar disk over a range of wavelengths. By scanning the solar-disk in time, one can construct a field of view (FOV) from the individual slits, with spectra recorded for each pixel in this FOV:

$$I_{\odot} \cong I(x, \lambda, y(t)), \quad (2.2)$$

where $y(t)$ is assumed to be the direction perpendicular to the slit. Consequently, the spatial distribution of intensities at a particular wavelength do not correspond to an instantaneous *image*. On the other hand, filtergraphs typically use a Fabry - Perot interferometer tuned to a specific wavelength to capture images. The spectra are then constructed by capturing successive images at a number of wavelengths:

$$I_{\odot} \cong I(x, y, \lambda(t)) \quad (2.3)$$

and, therefore, the intensities as a function of wavelength at a given position on the solar disk do not represent true spectra. In either case, a three-dimensional matrix of values can be obtained to represent the distribution of intensities over a FOV as well as wavelength, recorded over a given period. We use the term *data-cube* to refer to such a matrix. However, before the recorded intensities can be used to infer the physical properties of the solar atmosphere, the issue of image degradation, due to the Earth's atmosphere as well as the optical instruments, must be addressed. In this chapter, an overview of the theory behind image degradation in ground-based observations is provided, followed by an introduction to the methods currently used in correcting them.

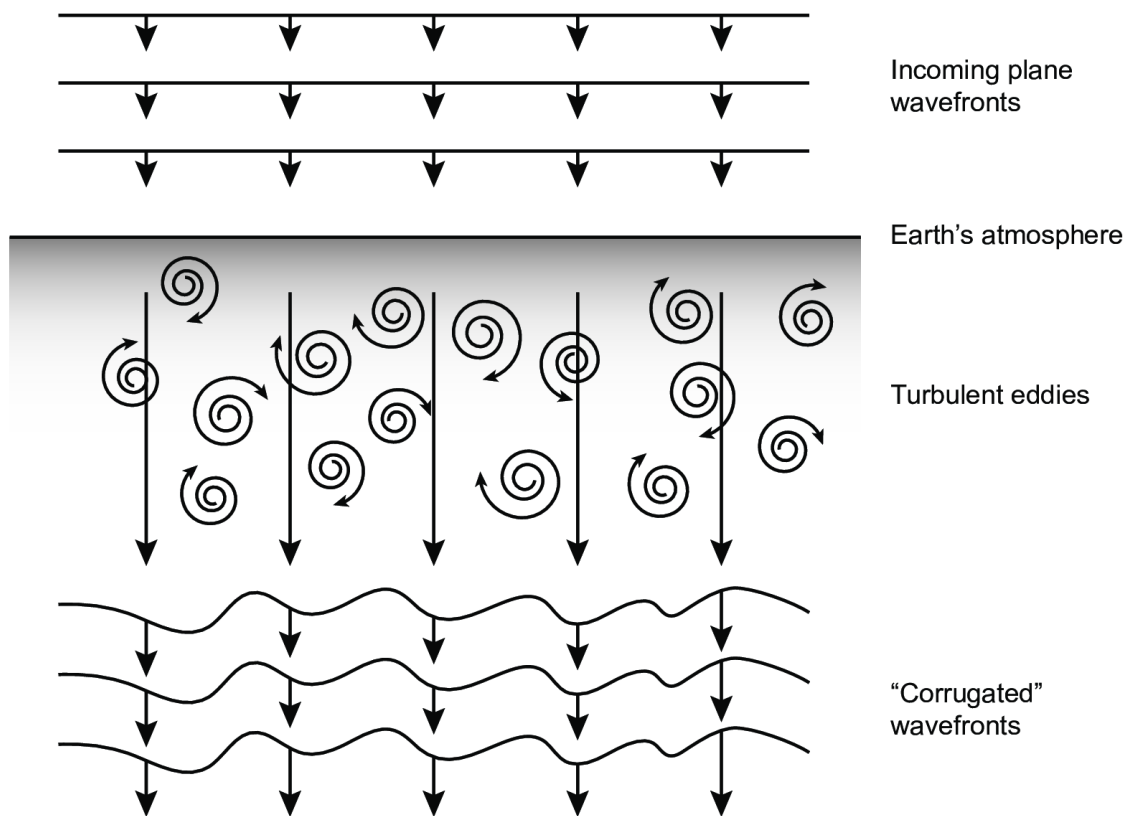


Figure 2.1: Schematic of the corrugations introduced in a plane-parallel wavefront by the refractive index fluctuations - atmospheric seeing.

2.1 Image degradation

Image degradation is simply the loss of quality of images. It can occur in various forms (loss of spatial resolution, noise, distortions, etc.) with different degrees of severity. While a certain amount of degradation in the final data is unavoidable (for example diffraction), it is generally beneficial to characterize other kinds so as to gain access to data that represent the distribution of intensities in the source faithfully (Eq 3.3).

2.1.1 The Earth's atmosphere

The Earth's atmosphere is far from a stably stratified medium. During the day, the heating of the crust by solar radiation is partly transferred to the atmosphere, establishing convection currents that ascend from the ground. Thus, at any given position and time, the density $\rho(\mathbf{x})$, temperature $T(\mathbf{x})$ become stochastic variables, in turn causing fluctuations in the refractive index of air. The stochastic nature of the thermodynamic parameters may also be caused by other phenomena such as wind shears and jet-streams. Regardless, in the context of image formation, the relevant fundamental property of the Earth's atmosphere is the refractive index $n(\mathbf{x}, t)$, a three-dimensional time-varying function whose fluctuations are non-deterministic. Thus, a plane-parallel wavefront ($\psi(\mathbf{r}) = 1$) propa-

gating through the Earth's atmosphere acquires a random phase $\phi(\mathbf{r})$, as a function of the two-dimensional position, before reaching the aperture of a telescope at a time t (Fig. 2.1). To describe the corrugations of this wavefront statistically, the appropriate structure function (D_ϕ) can be defined as follows:

$$D_\phi(\xi, t) = \langle |\phi(\mathbf{r} + \xi, t) - \phi(\mathbf{r}, t)|^2 \rangle, \quad (2.4)$$

where D_ϕ is a function of the displacement ξ between two points \mathbf{r} and $\mathbf{r} + \xi$ in the plane, and the angular braces indicate spatial averaging over the aperture. The structure function thus represents the phase-similarity between two neighbouring points on the wavefront in a statistical sense, which can be shown to be related to the auto-correlation function.

The form of the structure function is determined by the model of turbulence. For the specific case of the Earth's atmosphere, Kolmogorov's theory of turbulence (Kolmogorov 1941) is typically taken to be a good approximation for scales between 1 cm and 100 m, and D_ϕ takes the following form (Roddier 2004):

$$D_\phi(\xi) = 6.88(\xi/r_0)^{5/3} \quad (2.5)$$

$$r_0 = 0.423k^2(\cos\gamma)^{-1} \left[\int C_N^2(h)dh \right]^{-3/5}, \quad (2.6)$$

where ξ represents the spatial scale of fluctuations in the phase, k is the wave-number, γ is the zenith angle, and r_0 is the Fried parameter (Fried 1966) - a statistical quantity that represents the maximum effective diameter of a telescope for which diffraction limited images can still be obtained under the given seeing conditions. It is related to the structure constant C_N and increases with the wavelength of observations i.e. the *relative* effect of atmospheric seeing is reduced in observations made at larger wavelengths. Typical values of r_0 vary from 5 cm (poor seeing) to 20 cm (good seeing).

Each wavefront is associated with a Point Spread Function (PSF), a function that determines the spatial distribution of the intensity of a point source in the recorded image. In the absence of seeing, the PSF of an optical system is exclusively determined by the telescope and other optical elements downstream. In the presence of seeing, however, the central peak of the airy disk is typically broken into a pattern of speckles that change on the time-scales of seeing-fluctuations. Thus, images obtained without any correction to the wavefronts become distorted and blurred, causing a (usually) severe loss of spatial resolution and thereby signal. Additionally, if the observations include polarimetric data, atmospheric seeing may also cause 'crosstalk' between the polarization signals (see e.g. del Toro Iniesta 2003). Thus, to prevent (or reduce) the systematic degradation of observations due to atmospheric seeing, a suite of instrumental and numerical methods are frequently used.

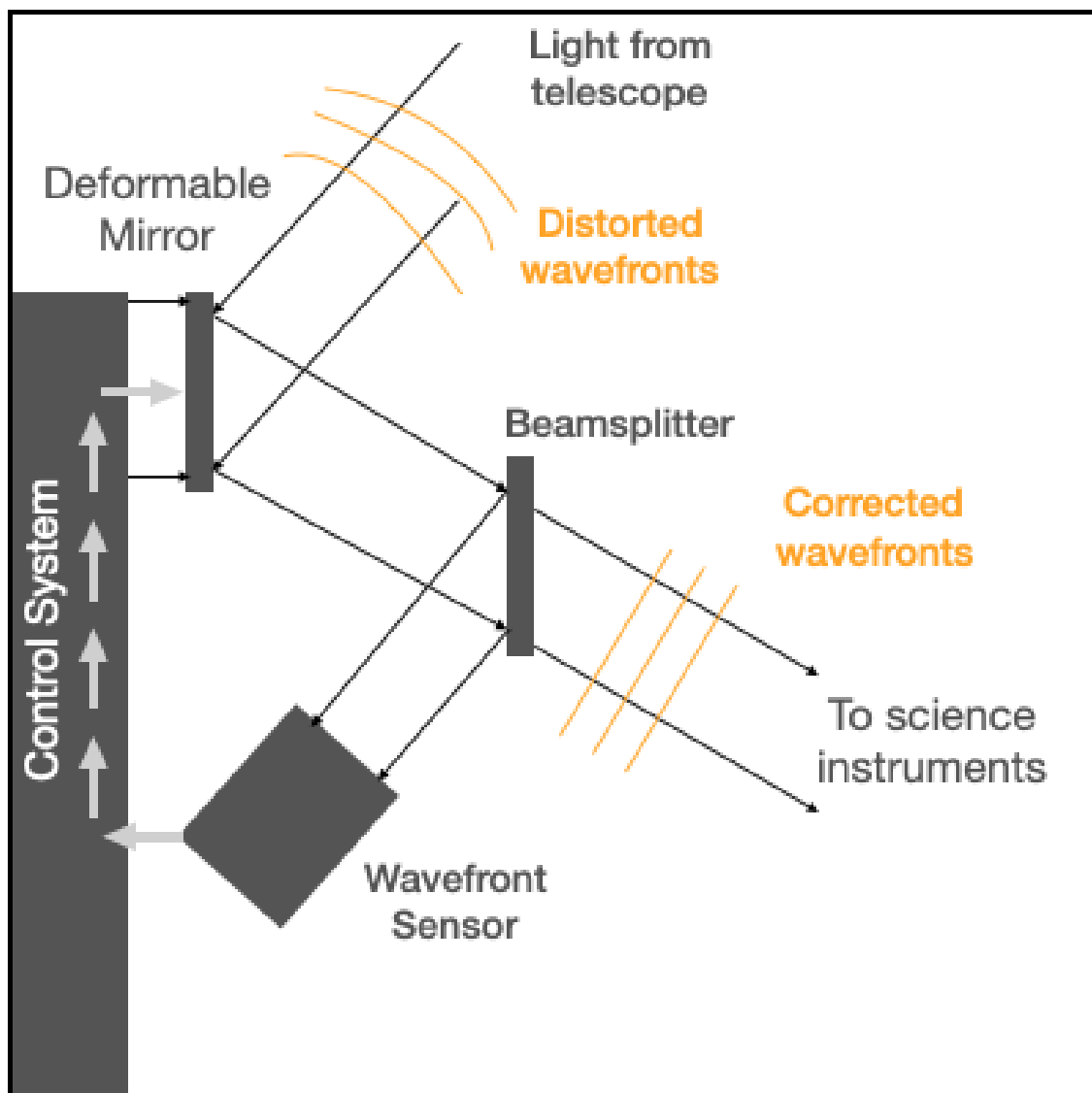


Figure 2.2: Schematic of the working principle of adaptive optics (AO) systems.

2.2 Image restoration methods

2.2.1 Adaptive optics

In the pursuit of reducing (or avoiding) image degradation, a good starting point is to reverse the random retardation in phase of the incident wavefronts (i.e. flatten them) before the optical elements and instruments downstream. This is achieved through the use of Adaptive Optics (AO) systems, which have become practically indispensable in ground-based observations, especially in solar telescopes larger than 1 *m*. A typical AO system consists of the following components (Fig. 2.2):

- **Beam Splitter** - The incident beam from the observed source is split into two, simultaneously feeding the primary optical train (scientific elements) and a Wavefront Sensor (WFS).

- **Wavefront Sensor (WFS)** - The WFS is a device used for measuring aberrations of an optical wave front. One common type is the Shack-Hartmann WFS, which consists of an array of sub-apertures spatially distributed so as to sample different regions of the pupil plane. A sub-image corresponding to each sub-aperture is generated, and the local slope of the wavefront is encoded in the shift of the sub-image with respect to a reference image.
- **Deformable Mirror (DM)** - The DM can be mechanically deformed to the desired shape through the use of piezo-electric actuators connected to its faceplate. The number of actuators used is usually equal to the number of sub-apertures of the WFS.
- **Processing unit** - The processing unit computes the slope of the wavefront at each sub-aperture from the image shifts, and converts them into appropriate voltages before applying them to the respective actuators of the DM.

Thus, AO systems continuously measure the shape of the wavefronts and deform the mirror so as to maximize the spatial coherence of the reflected wavefront. If the control loop is run significantly faster ($\sim 2 \text{ kHz}$) than the de-correlation time of a single wavefront, the latency between the detection of the shape (in the WFS) and the application of the voltages (to the DM) can be assumed to introduce only a small error in the applied corrections. However, since the number of sub-apertures is finite, aberrations in the incident wavefronts corresponding to larger spatial scales (low-order) are corrected more efficiently than those corresponding to smaller spatial scales (high-order). The presence of residual, i.e. uncorrected high-order aberrations may also be caused by the insensitivity of the WFS to the second-order shape (curvature of the wavefront over each sub-aperture). Thus, while AO systems dramatically improve the SNR and the spatial resolution of the final images, residual aberrations may still prevent them from being diffraction limited, requiring further restoration using computational methods. Additional causes of residual aberrations include differential seeing in the Earth's atmosphere (multiple turbulent layers geometrically separated by height). Differential seeing typically induces anisoplanatic effects in the wavefronts i.e. the statistical properties of wavefronts vary with angle, limiting the area over which wavefront aberrations are corrected by the AO. For a comprehensive review on the design and performance of AO systems, see the review by Rimmele and Marino (2011).

2.2.2 Speckle reconstruction

Before the deployment of modern AO systems in telescopes, a method used to surpass the resolution limit set by atmospheric seeing was the speckle interferometry holographic technique, proposed by Labeyrie (1970). The technique relied on capturing multiple short-exposure images of an apparent point source, the instantaneous intensity distribution (I_{\star}^{inst}) of which can be described in the spatial and Fourier domains, respectively, by:

$$I_{\star}^{inst}(\mathbf{x}) = I_0(\mathbf{x}) * p(\mathbf{x}) \quad (2.7)$$

$$\hat{I}_{\star}^{inst}(\mathbf{k}) = \hat{I}_0(\mathbf{k}) \cdot \hat{p}(\mathbf{k}), \quad (2.8)$$

where $I_{\star}^{inst}(\mathbf{x})$, $I_0(\mathbf{x})$, and $p(\mathbf{x})$ denote the observed intensity distribution, the unknown source intensity distribution, and the PSF of the optical system, respectively. In the presence of atmospheric seeing, since $I_{\star}^{inst}(\mathbf{x})$ is broken into a pattern of speckles for a point light-source, the estimation of the angular diameter of a star (or the detection of binary stellar systems) directly from the observed images is difficult. Thus, the photographic films on which the intensities were recorded were used as an aperture to diffract a coherent light source such as a laser (holography). Recording the observed diffraction patterns of the incident laser for each short-exposure image then yielded the power spectra of the observed intensities of the respective frames:

$$|\hat{I}_0(\mathbf{k})|^2 = \frac{\sum |\hat{I}_{\star}^{inst}(\mathbf{k})|^2}{\sum |\hat{p}(\mathbf{k})|^2}, \quad (2.9)$$

where the power spectra of the source intensity distribution are retrieved from Eq 3.8. However, since information about the phase of the Fourier transformed image is lost in the holographic technique, the reconstruction of the source intensity distribution is only possible under the assumption that $I_0(\mathbf{x})$ is centro-symmetric. Nonetheless, Labeyrie (1970) used the method to show the presence of characteristic interference patterns in the optical Fourier images of a simulated double-star system separated by an angular distance much smaller than the seeing-limited spatial resolution. The validity of the method was subsequently verified in observations of nine stars (including binary stellar systems) by Gezari et al. (1972), who detected stellar angular diameters as small as 0.016".

The issue of the unknown phase was subsequently addressed by Knox and Thompson (1973), who used interference from an additional off-axis reference coherent light source to retrieve the phase information. With both the power spectra and the phase of the source so determined, the construction of the intensity distribution of the source in the spatial domain became possible. Thus, von der Luehe (1985), von der Luhe (1987), von der Luhe and Dunn (1987), and Keller and von der Luehe (1992a) extended the method to solar observations. The latter, for example, used two cameras in two channels with different filters (one broad-band and one narrow-band) to simultaneously record the intensity distribution of the solar scene (speckle imaging). The broad-band images were used to derive the instantaneous Optical Transfer Function (OTF) corresponding to each frame, following which the source intensity distributions in the narrow-band were retrieved.

2.2.3 Multi-Object Multi-Frame Blind Deconvolution

One of the limitations of the speckle reconstruction methods is the assumption that the properties of atmospheric turbulence are statistically well described, an assumption that does not apply well to wavefronts that have been partially corrected in the lower orders by an AO system, or for bursts of data that are too short to obtain the statistics accurately (especially for apertures larger than one meter). In the Multi-Frame Blind Deconvolution

(MFBD) method developed by Paxman et al. (1992), Paxman et al. (1996), and later van Noort et al. (2005), this limitation is circumvented as the method makes no prior assumptions about the behaviour of the atmospheric seeing, except that they fluctuate on time-scales typically much shorter than the time-scales of evolution of the observed solar features. The theory of this method is briefly described below.

In the MFBD method, multiple images (frames) of the object are captured in succession through a variety of different independent channels (filter or polarization states). The image formation model described in Eq. 3.7 and Eq. 3.8 are assumed to be valid after the addition of an additive (Gaussian) noise term. Additional channels that improve the restoration such as Phase-Diversity (Löfdahl and Scharmer 1994a) may also be used to record more intensities. For frames recorded within a given well-defined span of time, the object (solar scene) is assumed to be static so that variations in the observed distribution of intensities with time can be assumed to be exclusively driven by different realizations of atmospheric seeing. In the case of atmospheric turbulence, such realizations are usually sufficiently linearly-independent to constrain the intensity distribution of the source. In MFBD, however, the estimation of the PSFs corresponding to each observed, degraded frame is indirect - they are computed from wavefronts parametrized by a set of coefficients (α_j) that represent the 'components' of the wavefronts when projected onto an orthonormal set of basis modes ($Z_m(\mathbf{x})$) defined over a circular aperture:

$$\phi_j(\mathbf{x}) = \theta_j + \sum_m \alpha_{jm} Z_m(\mathbf{x}) \quad (2.10)$$

where j denotes a specific frame, and θ_j represents the addition of known aberrations, for example the de-focus in Phase-Diversity channels. The modes m are typically arranged in the order of decreasing spatial scales. Thus, estimating the wavefront that caused the degradation of a *specific* frame translates to estimating the correct α_j corresponding to that frame. This is subsequently achieved by iteratively minimizing a suitably defined Maximum-Likelihood error metric for each independent *object* in the observations:

$$L(\alpha_j) = \sum_\nu \left[\sum_j |I_j^{inst}|^2 - \frac{|\sum I_j^{inst*} \hat{p}_j|^2}{\sum |\hat{p}_j|^2 + \gamma_j} \right] \quad (2.11)$$

where $L(\alpha)$ is the error metric, ν represents the channel, and j indexes the recorded frames corresponding to a single object. Minimization of this error metric yields the best estimate of the coefficients α_j , as well as the most probable intensity distribution of the source, assuming those coefficients are correct. Thus, both $I_0(\mathbf{x})$ and $p(\mathbf{x})$ are estimated by the MFBD method.

Nonetheless, a few issues in this formalism exist. While MOMFBD is flexible in its implementation, the expansion of the wavefronts in terms of the basis modes is invariably truncated at a particular mode limit \mathcal{M} . This leads to a systematic underestimation of the degradation caused by high-order aberrations in the wavefront - i.e. stray light. A more detailed description of this effect is provided in the next chapter.

2.3 Restoration of slit-spectra

In the previous section, some of the prevalent methods that are used to restore images obtained from ground-based telescopes were briefly introduced. The current section provides an overview of the restoration of slit-spectra on which this thesis is based.

As described in the introductory sections of this chapter, traditional long-slit spectrographs exchange a spatial dimension (perpendicular to the slit) for simultaneous information along wavelength. The intensity distribution of the FOV is then constructed by scanning the slit over the solar surface. While this allows the spectrum in a given pixel to represent that of the Sun more faithfully than filtergrams (especially when magnetic elements evolve rapidly), the exchange comes at the cost of not having simultaneous information about the distribution of intensities around the slit - a prerequisite for the image restoration methods described above. Moreover, long-slit spectrographs were often paired with long integration times (0.1 – 1 s) to improve the SNR, making it difficult for observations to reach the diffraction limits of the telescopes due to the smearing from atmospheric seeing.

In spite of these challenges, the first attempt to restore data obtained from slit-spectrographs was made by Keller and Johannesson (1995). In their setup, they used a slit-jaw camera with a broad-band filter to image the distribution of intensities around the slit, and another camera to record the dispersed spectra. The bandwidth of the broad-band filter included the spectral range covered by the spectrograms. While the image formation model for the traditional case has been described above, the corresponding model for the observed intensities of the slit-spectra, neglecting the noise terms, are described by:

$$I_s(\lambda, y, t) = \int w(x(t) - x')(I_0(x', y, \lambda) * p(x', y, t))dx' \quad (2.12)$$

where $I_s(\lambda, y, t)$ is the spectrum recorded by the spectral camera, $I_0(x', y, \lambda)$ is the unknown true source distribution of the spectra, y is the direction along which the slit is oriented, $w(x(t))$ is the transmission function of the slit located at $x(t)$, and the integration is performed over the slit-width. Using the broad-band slit-jaw images, Keller and Johannesson (1995) deduced the PSFs of the individual frames with the speckle imaging technique as a function of time. By discretizing Eq 3.12 and re-arranging the terms, the equation can be recast to the following matrix equation:

$$\mathbf{I}_s = \mathcal{K}\mathbf{I}_0 + \mathbf{N} \quad (2.13)$$

where \mathcal{K} is a matrix storing information about the deduced PSFs, and the observed intensities $I_s(\lambda, y, t)$ are stacked to form the column matrix \mathbf{I}_s with N^2 elements. The additive noise \mathbf{N} has been re-introduced in the image formation model. Thus, recovering the unknown true solar spectra \mathbf{I}_0 follows if the inverse of the matrix \mathcal{K} can be computed. This is, in general, a difficult task as the matrix \mathcal{K} is ill-conditioned due to the discretization and the presence of error terms, and may also be non-square. Keller and Johannesson (1995) attempted to retrieve the solution \mathbf{I}_0 through the Tikhonov-regularization method:

$$\mathbf{I}_0 = (\mathcal{K}^T \mathcal{K} + \beta L^T L)^{-1} \mathcal{K}^T \mathbf{I}_s, \quad (2.14)$$

where the regularization matrix L was chosen to be the two-dimensional Laplacian. Thus, in their application of the method to observations of solar granulation, they found that the granulation contrasts increased from 7.0% in the raw-data to 10.5% in the speckle-reconstructed spectra, and the variation of intensities at the high-frequencies were improved compared to the raw data. Although their method was an important theoretical development, the inherent issues in speckle imaging and the lack of better instruments (sensors and polarimeters) limited the applicability of their method to observations with lower spatial resolution compared to modern telescopes.

Following the advances in AO systems, the development of fast polarimeters, and improvements to the camera read-out speeds, a more recent attempt to revisit the restoration of slit-spectra was undertaken by van Noort (2017a). He obtained slit-spectra with the TRIPPEL spectrograph (Kiselman et al. 2011b) at the 1 m Swedish Solar Telescope (SST, Scharmer et al. (2003a)). Although his formulation of the restoration is theoretically similar to the one followed by Keller and Johannesson (1995), a few key distinctions in the acquisition of data are worth noting. The first is the spatial resolution ($\sim 0.06''$), the spectral resolution ($\sim 41'' \text{ m}\text{\AA}$), and the comparatively broad spectral range ($\sim 16\text{\AA}$) of his observations, covering several spectral lines. This allows inversion codes to set better constraints on the deduced atmospheric parameters as a larger number of spectral lines each encode the physical parameters of the solar atmosphere in different ways. Secondly, his observations were made with the polarimeter, the slit-jaw camera and the spectral camera operating at a frequency of 400 *fps*. This enabled him to significantly reduce the integration time of the scan compared to earlier studies, thereby reducing the smearing effects of atmospheric seeing. Thus, the spatial resolution of his observations were reasonably close to the diffraction limit of the 1 m telescope at 6300 \AA . Lastly, the estimation of the PSFs from the slit-jaw images was performed using the MOMFBD method, although the underestimation of the wings of the PSFs (as described in the earlier section) was a persistent limitation. Consequently, the results of his efforts indicate that it is possible to obtain near diffraction-limited observations, even in data obtained from the ground with long-slit spectrographs.

While these image restoration methods have significantly improved the quality of ground-based observations, persistent residual image-degradation in the form of stray-light contamination continues to be an important issue that is worth characterizing, since the detrimental effects of such contamination are more evident in the way spectral line profiles are modified. Without methods to correct for the stray-light contamination, the accuracy with which the thermodynamic and magnetic atmospheres of solar faculae are retrieved by inversion codes would be limited. In the next chapter, a statistical method based on Kolmogorov-turbulence to remove stray-light contamination from slit-spectra is discussed, along with a more detailed description of the data obtained by van Noort (2017a). Further, the chapter also outlines where, and how modern image restoration methods fall short of addressing residual image degradation in ground-based observations.

3 Correction of atmospheric stray light in restored slit spectra

Saranathan, S., van Noort, M., Solanki, S. K.,
Astronomy and Astrophysics, in press¹

My contribution: Data reduction, writing of the manuscript

Abstract

A long-standing issue in solar ground-based observations has been the contamination of data due to stray light, which is particularly relevant in inversions of spectropolarimetric data. We aim to build on a statistical method of correcting stray-light contamination due to residual high-order aberrations and apply it to ground-based slit spectra. The observations were obtained at the Swedish Solar Telescope, and restored using the multi-frame blind deconvolution restoration procedure. Using the statistical properties of seeing, we created artificially degraded synthetic images generated from magneto-hydrodynamic simulations. We then compared the synthetic data with the observations to derive estimates of the amount of the residual stray light in the observations. In the final step, the slit spectra were deconvolved with a stray-light point spread function to remove the residual stray light from the observations. The RMS granulation contrasts of the deconvolved spectra were found to increase to approximately 12.5%, from 9%. Spectral lines, on average, were found to become deeper in the granular lanes and shallower in the inter-granular lanes, indicating systematic changes to gradients in temperature. The deconvolution was also found to increase the redshifts and blueshifts of spectral lines, suggesting that the velocities of granulation in the solar photosphere are higher than had previously been observed.

3.1 Introduction

The degradation of observations due to stray light has been a long-standing issue in solar physics. The term stray light, in recent literature, has come to refer to extraneous undesirable contributions to pixel intensities in images and spectra caused by one or more independent physical processes. Stray light is currently understood to be the sum of multiple components with possibly differentiable characteristics (see Martínez Pillet (1992), Beck et al. (2011) for a comprehensive review). For ground-based observations, these include

¹©ESO. Reproduced with permission. DOI: <https://doi.org/10.1051/0004-6361/201937100>

the refraction of light due to seeing, as well as large-scale scattering due to the presence of aerosols, dust, molecules, etc. The former effect varies rapidly with time and is the dominant effect over distances typically up to a few arcseconds, while the latter exhibits slower modulation and brings contributions from sources that are much farther away. For example, the inexplicable brightness of sunspot umbrae (Zwaan 1965) was found to be due to atmospheric scattering of light from the full solar disk. Stray light is also generated within telescopes and instruments by the diffraction of light, as well as scattering due to the surface roughness of optical elements. It is even present in space-based observations and may be anisotropic and inhomogeneous over the field of view (FOV).

Stray-light contamination manifests itself differently in images and spectra. Images suffer a loss of spatial resolution, as well as a reduction in intensity contrasts - an effect verified by observations obtained through both space-based and ground-based instruments (see Uitenbroek et al. 2007, Sánchez Cuberes et al. 2000, Danilovic et al. 2008). While this contrast reduction has been satisfactorily modelled in space-based observations (e.g. Mathew et al. 2009, Wedemeyer-Böhm and Rouppe van der Voort 2009), a discrepancy still exists in ground-based observations (Scharmer et al. 2010a). The effects of stray light on spectra are revealed by inversions of spectropolarimetric data. The mixing of intensities alters the depth, broadening, and symmetry of spectral lines, introducing different errors in different spectral lines. The quality of the fit in inversions is therefore generally poorer, and the reliability of the retrieved physical parameters is reduced. Several prescriptions to tackle spectral contamination can be found in the literature.

Orozco-Suárez et al. (2007) first proposed such a method by constructing a local stray-light profile from a $1''$ region surrounding every pixel. The inversion code was then allowed to fit the weight of this profile in the pixel being inverted. Although a significant step forwards, the method is formally incorrect as the stray-light contribution in a pixel cannot be directly estimated from the contaminated data. An improvement over this method through a self-consistent coupled inversion scheme was proposed by van Noort (2012). However, the method requires prior knowledge of the transfer functions that do not vary within the FOV. These constraints are likely not satisfied by ground-based observations (especially from spectrographs), and the preferred approach, therefore, is to restore the data as perfectly as possible before inversions.

Restoration of degraded observations is only possible with an estimate of the transfer function of the optical system. Systematic efforts have been undertaken along these lines. The earliest such attempts were made by Wanders (1934), Stumpff (1961), and David and Elste (1962). They defined an analytical point spread function (PSF) that quantified the extraneous contribution to intensity in a given pixel, as a function of distance. Subsequent theoretical and empirical refinements to the model were made by Zwaan (1965), Staveland (1970), Mattig (1971), and later Martínez Pillet (1992). Although instructive, early models of the spread function were limited in their ability to improve the quality of ground-based observations due to the use of coarse assumptions. A significant boost came from parallel developments in data acquisition, adaptive optics (AO), and image restoration techniques, such as speckle (Keller and von der Luehe 1992b), phase-diversity (Paxman et al. 1992, Löfdahl and Scharmer 1994b), and multi-frame blind deconvolution (MFBD; van Noort et al. 2005), which attempt to model the true PSF as it changes with time. In the current paradigm, AO systems and image restoration methods are routinely employed to circumvent degradation and/or reverse it to an acceptable level.

Despite the progress, persistent signs of degradation in ground-based observations have prompted a careful search for the sources of residual stray light. Scharmer et al. (2010a) found that high-order wave-front aberrations - corresponding to the wings of the PSF, which were systematically underestimated by MFBD - could be partly responsible for residual stray light in ground-based observations. They used a statistical method based on Kolmogorov statistics and knowledge of the Fried parameter r_0 (Fried 1966) to approximate corrections to the transfer functions returned by MFBD and subsequently reduce the amount of residual stray light in observations. We propose a refinement to this method by using the values of the Fried parameter to generate fully turbulence-degraded synthetic observations. Restoring the synthetic observations along with the actual observations in parallel, using MFBD, allows us to self-consistently quantify the efficiency with which the AO reversed seeing-induced degradation in the actual observations. Given that AO systems are not perfect, these efficiencies can be used to arrive at estimates of the residual degradation present in the AO-corrected, MFBD-restored observations. In this paper, we discuss the theory of the method and its implementation on spectropolarimetric data obtained from the Swedish Solar Telescope (SST, Scharmer et al. 2003b).

3.2 Residual degradation in ground-based observations

When observing astrophysical objects through a telescope of finite aperture, diffraction sets a fundamental limit to the spatial resolution of the final image(s). In the presence of atmospheric seeing, or due to the instruments themselves, additional degradation may be introduced. For a given optical system, quantification of image degradation in the observations is made with its transfer function. If the optical system includes the atmosphere, such as is the case for ground-based observations, the transfer functions are also time-dependent. We write the image formation model in the fourier domain:

$$\hat{I}(\vec{k}, t) = \hat{T}_{atm}(\vec{k}, t)\hat{T}_{inst}(\vec{k})\hat{O}(\vec{k}) + \hat{N}(\vec{k}), \quad (3.1)$$

where \vec{k} and t denote spatial frequency and time, respectively, $\hat{T}_{atm}(\vec{k}, t)$ is the transfer function of the atmosphere, $\hat{T}_{inst}(\vec{k})$ is the transfer function of the telescope and relevant instruments, and $\hat{O}(\vec{k})$ represents the true solar scene. $\hat{N}(\vec{k})$ represents additive noise, and $\hat{I}(\vec{k}, t)$ is the flat-fielded, dark-current subtracted image, recorded by the detector. In ground-based observations, the explicit dependence of $\hat{O}(\vec{k})$ on time is dropped because the timescales of solar evolution are much larger than the fluctuation timescales of the Earth's atmosphere.

To model $\hat{T}_{atm}(\vec{k}, t)$, the approximation that it is the result of a pure phase error in the wave front is commonly made. Wave-front phase errors are introduced either by the optical elements themselves (static) or by the atmosphere (dynamic). The $\hat{T}_{atm}(\vec{k}, t)$ is then computed using:

$$\zeta(\vec{x}, t) = \exp(i\phi(\vec{x}, t)), \quad (3.2)$$

$$\hat{T}_{atm}(\vec{k}, t) = R(\zeta, \zeta^*), \quad (3.3)$$

where $\phi(\vec{x}, t)$, $\zeta(\vec{x}, t)$, and $R(\zeta, \zeta^*)$ are the wave fronts, the pupil function, and the auto-correlation function, respectively. A perfectly flat wave front corresponds to an ideal

transfer function that drops nearly linearly with \vec{k} . In the presence of aberrations, the decline with \vec{k} is much steeper, forming images with a reduced signal to noise ratio (S/N) at high spatial frequencies. To prevent this, an AO system can be deployed combining a wave-front sensor (WFS) with a deformable mirror (DM) to measure and compensate wave-front aberrations in real time. The efficacy of such systems is a function of the number of actuators driving the DM, sampling of the wave front by the WFS, and the bandwidth of the AO. A review on the design and performance of AO systems is found in Rimmele and Marino (2011).

Aberrations are often quantified by projecting the corresponding spatial distribution of the wave-front phase error onto an ordered set of basis modes (Zernike polynomials, Karhunen-Loève functions, etc.):

$$\phi(\vec{x}, t) = \sum_{l=0}^{\infty} C_l Z_l(\vec{x}, t), \quad (3.4)$$

where l denotes the mode number, ϕ is the wave-front phase error, Z_l are the basis modes, and C_l are mode amplitudes. In closed-loop operation, AO systems act as high-pass filters (Rimmele and Marino 2011). Specifically, the amplitudes of low-order aberrations are suppressed better than the high orders. The meaning of "low" and "high" in this context is somewhat arbitrary as no such sharp boundary exists. Nonetheless, it is instructive to rely on such a classification for the purposes of motivating what follows. The action of AO on the wave-front error can then be written as:

$$\phi^{AO} = \sum_{l=0}^{\infty} (1 - \epsilon_l^{AO}) C_l Z_l, \quad (3.5)$$

where explicit dependence on \vec{x} and t is dropped for brevity. ϕ^{AO} is the phase-error after compensation by the DM, and ϵ_l^{AO} quantifies the suppression of mode l . That is, ϵ_l^{AO} characterises the efficiency of the AO in compensating for phase errors with a spatial distribution according to mode l . For perfect compensation, $\epsilon_l^{AO} = 1$, and the residual wave-front error would be identically zero over the entire aperture. Realistically, ϵ_l^{AO} would depend on l and typically vary between zero and one. Given that AO systems act as high-pass filters, ϵ_l^{AO} would be close to one at the lower orders and close to zero at the higher orders. One would also expect the AO to become completely ineffective beyond a certain point, that is:

$$\epsilon_l^{AO} = 0, \quad \forall \quad l > L. \quad (3.6)$$

However, during the application of our method to actual observations, several scenarios were observed when ϵ_l^{AO} was non-zero even when $l > 200$ were observed. Further interpretations of this characteristic are provided in Sec. (3.7) of this paper. Additional complications concerning the nature of ϵ_l^{AO} are that they may potentially vary with seeing, and within the FOV. The dependence on seeing is due, in part, to the way in which the WFS detects the shape of incident wave fronts. For instance, a Shack-Hartmann WFS, such as the one used at SST, simultaneously images a local region in the FOV through an array of sub-apertures. Cross-correlations of the sub-images are then used to compute their relative shifts, and subsequently the local tip-tilt of wave fronts over the sub-apertures. The

reliability of these shifts is particularly impacted when the seeing is very poor. Correspondingly, the ϵ_l^{AO} would be low. The second complication - dependence of ϵ_l^{AO} on the location - is due to anisoplanatism. When using an AO with a single mirror and a WFS, only the seeing that is common to the whole FOV can be corrected over the whole FOV. The more distant the atmospheric turbulence is, the smaller the area of the FOV that shares the same wave-front aberrations (isoplanatic patch), and the smaller, therefore, the area that can be fully corrected. However, any corrections that are specific to one isoplanatic patch are unavoidably applied to the whole FOV, and therefore added to the aberrations everywhere else, thus causing a statistical increase in the wave-front errors there, rather than a decrease. To avoid this, a ground-layer WFS can be used that relies on a larger area than one isoplanatic patch to calculate the wave-front slope, so that the cross-correlations are less sensitive to wave-front errors that are not shared across that area.

In practice, this method reduces, but does not completely eliminate, the sensitivity to anisoplanatic wave-front aberrations, so that the correction of the wave-front phase errors becomes increasingly ineffective with distance from the region to which the AO is locked onto (hotspot). This leads to statistically poorer corrections at the edges of the FOV. A combined effort of evaluating how the corrections get worse with distance, and how the high altitude seeing intrinsically varies within the FOV is required in order to characterise this effect. In the context of this section, the most important realization concerning ϵ_l^{AO} is that they are generally unknown. This leaves the profile of residual wave-front phase errors unknown, and therefore the corresponding residual transfer functions unknown. Revising the image formation model to allow AO-compensations, and denoting the residual transfer functions corresponding to ϕ^{AO} as \hat{T}^{AO} , we write:

$$\hat{I}(\vec{k}, t) = \hat{T}(\vec{k}, t)\hat{O}(\vec{k}) + \hat{N}(\vec{k}). \quad (3.7)$$

It is implicit that $\hat{T}(\vec{k}, t)$ corresponds to the combined optical system where the time-dependence is solely caused by the atmosphere. The subscripts have, therefore, been dropped. Further improvements to the quality of observations are availed with the use of post-facto processing methods such as MFBD (van Noort et al. 2005, van Noort 2017b) that do not require prior knowledge of the degrading transfer functions. In MFBD image restoration, estimates of the transfer functions are made directly from the degraded observations. This is achieved by expanding the wave-front phase errors onto an orthogonal basis and fitting for the amplitude of every mode. However, the basis used by MFBD is ultimately finite and the expansion is truncated to a mode limit M , which causes a systematic underestimation of the wings of the Point Spread Functions (PSFs). Therefore, while MFBD corrects for degradation caused by lower-order modes, the effects of the higher orders (stray light) are left largely untreated. Since image restoration with MFBD is normally performed on observations that are already AO-compensated, one may assume that:

$$\epsilon_l^{AO+MFBD} = 1, \quad \forall \quad l < M, \quad (3.8)$$

that is, residual degradation in AO-compensated MFBD-restored observations are exclusively due to the higher-order modes. A peculiar state of compensation is realised when the AO corrects more modes than MFBD ($L > M$). In this case, modes with $l < M$ are perfectly compensated by the AO and MFBD, modes with $M < l < L$ have been compensated

by the AO (but with unknown efficiency), and modes with $l > L$ have not been compensated at all. Alternatively, one may try to perform image restoration with M increased to $\sim L$ so that the issue of the unknown correction efficiency of the AO is circumvented entirely. However, given that the efficiency of wave-front corrections made by the AO vary within the FOV, mitigation of this issue is attempted during image restoration - by segmenting the FOV into a grid of patches and restoring each patch individually. In doing so, the assumption that wave-front phase errors over each patch are isoplanatic is made. This imposes a limitation on the admissible physical size of the PSFs, and indicates that restoring with arbitrarily high mode limits is not beneficial. The preferable approach is therefore to develop a self-consistent method of removing residual stray light from the restored data directly.

We clarify that the term 'residual stray light' here refers exclusively to the component of stray light arising from high-order aberrations. Other sources of stray light, such as true scattering in the atmosphere and within the instrument, are beyond the scope of this paper. Correspondingly, we refer to the PSF describing stray-light contamination as a stray-light PSF.

3.3 Residual degradation in slit spectra

In the previous section, we reviewed the limitations of AO and MFBD and qualitatively addressed the nature of residual degradation in ground-based observations. We now describe the characteristics of residual stray-light contamination in spectropolarimetric data obtained with Spectrographs. A detailed discussion on how such data are obtained and restored is found in van Noort (2017b). Here, we only briefly review the relevant details. In the interest of keeping the description concise, we ignore the polarimetric aspect of such data. We assume that the conclusions drawn in this section apply to all the Stokes components equally.

Slit-spectra are obtained with a detector that collects light that has passed through a slit, and that has been dispersed by a dispersive element, usually a grating. Another detector (slit-jaw camera) is used to image the slit and the surrounding FOV through a broadband filter spanning the spectral region covered by the spectra. Both the detectors are operated synchronously so that the recorded images/spectra can be assumed to be degraded by the same seeing, and the frame-rates of the detectors are kept high enough to prevent seeing-induced distortions, and seeing-induced crosstalk. The images recorded by the slit-jaw camera are restored in bursts with MFBD to yield estimates of the degrading PSFs as a function of space and time. However, to restore the slit-spectra, one cannot directly deconvolve them as the intensities perpendicular to the slit have not been recorded co-temporally. Instead, the problem is reformulated into a set of linear equations that connect the observed intensities with the undegraded solar spectra through the PSFs. That is, Eq.1 can be re-written into a matrix equation of the form:

$$\hat{M}\mathbf{x} = \mathbf{y}, \tag{3.9}$$

where \mathbf{x} represents the coveted undegraded spectra, \mathbf{y} represents the seeing-degraded intensities recorded by the spectral camera, and \hat{M} is, in principle, a non-sparse non-square matrix that represents an instantaneous PSF. The values of such PSFs are obtained from

the MOMFBD restoration of the slit-jaw images, and therefore the matrix \hat{M} is completely known. Eq. 3.9 can be constructed for every wavelength point, and for each instant of time, yielding an over-determined system of coupled equations. Since \hat{M} is not a square matrix, one could instead solve the pseudo-inverse problem:

$$\hat{A}\vec{x} = \vec{b}, \quad (3.10)$$

where $\hat{A} = \hat{M}^T \hat{M}$ is a square matrix, and $\vec{b} = \hat{M}^T \vec{y}$. However, since a large number of equations and unknowns are typically involved, it is difficult to directly invert the matrix \hat{A} . The solution therefore, is obtained using a variation of the iterative Lucy-Richardson scheme. Since the matrix \hat{A} is constructed using PSFs whose wings are underestimated, the solution thus obtained is likely to still contain some residual stray light. If we were to estimate a correction $\delta\hat{A}$ to \hat{A} that addressed this issue, the most self-consistent way forwards would be to construct a new matrix $\hat{A}' = \hat{A} + \delta\hat{A}$ and restore the raw data again. However, due to the rapid scaling of computational workload with the size of the domain, using \hat{A}' becomes prohibitively expensive. We therefore propose an alternate method of removing stray light directly from the restored spectra.

First, the Stokes signals are converted to modulated intensities using an arbitrary modulation scheme for each wavelength, yielding four modulated intensities corresponding to each Stokes parameter. This is followed by degrading the modulated intensities with a diffraction limited PSF corresponding to the aperture of the telescope. The degraded intensities corresponding to each Stokes parameter are then deconvolved using the same set of PSFs that describe residual stray light exclusively across all wavelengths. Although the deconvolution is bound to amplify the noise in the signals, this amplification is uniform across the Stokes parameters and does not, therefore, introduce spurious polarization signals (polarimetric precision is preserved). After the deconvolution is performed, the same modulation scheme used in the forward modulation is used to invert the deconvolved intensities back into Stokes spectra. The method described above requires that a set of suitable stray-light PSFs be found. Two key aspects of such a set of stray-light PSFs have to be noted.

Firstly, at any given wavelength, slit-spectra are not truly images because the intensities along the scan-direction have been recorded at different times. It then follows that residual stray light generally varies along the scan-direction as the seeing evolves with time. Therefore, to remove residual stray light from a single 'image' at a particular wavelength, multiple stray-light PSFs spanning the duration of the scan have to be computed. This complication is not shared by observations made with filtergraphs, as intensities there are obtained strictly co-temporally. Secondly, consider a fixed point on the Sun. Let the slit sample this point at time t_0 . According to Eq. (3.10), the true solar intensity of this point (solution) is computed from the intensities in the slit recorded between $t_0 - \Delta t$ and $t_0 + \Delta t$, where $2\Delta t$ is the time it takes for the slit to scan the spatial extent of the PSF. Naturally, intensities recorded at t_0 carry the highest weights towards the solution while those recorded at $t_0 \pm \Delta t$ carry the lowest. The correct amount of residual stray light is therefore described not just by one stray-light PSF computed at t_0 , but through a weighted average of many stray-light PSFs computed between $t_0 - \Delta t$ and $t_0 + \Delta t$, with the weights specified in the matrix \hat{A} .

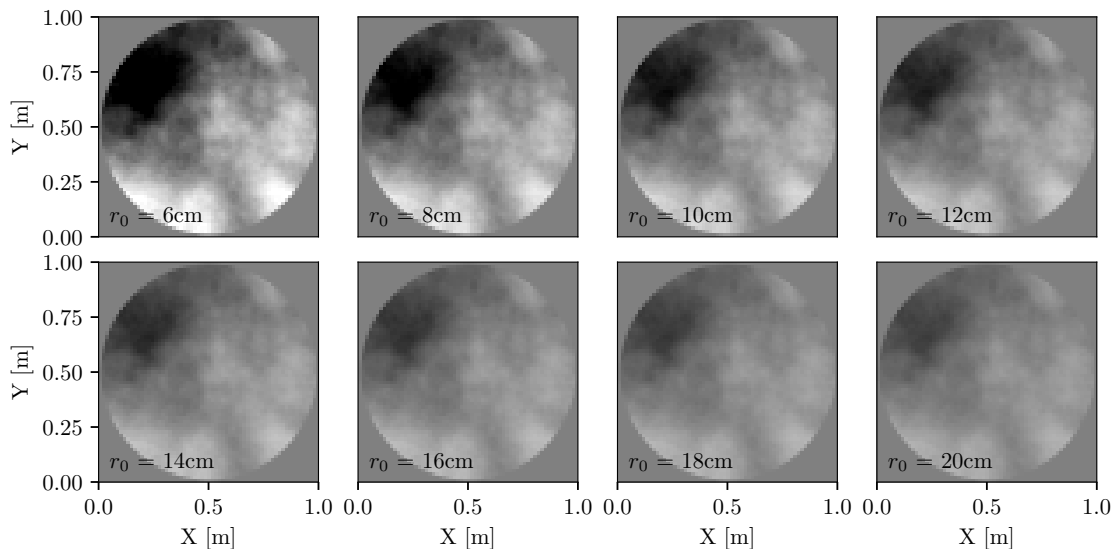


Figure 3.1: Kolmogorov wave fronts simulated for different values of the Fried parameter r_0 , for an aperture size of 1 m. The mean values of all the wave fronts have been subtracted, and a uniform grey scale has been used in the illustration of the wave fronts.

3.4 Estimating the stray-light PSF

Scharmer et al. (2010a) followed a statistical method, where values of the Fried parameter (r_0) were used to simulate a set of wave fronts obeying Kolmogorov statistics. r_0 values were calculated using a setup employing a wide-field wave-front sensor installed before the tip-tilt mirrors and the DM. At the time, the DM was driven by a 37-electrode configuration, corresponding to roughly 37 KL-modes. However, the DM at SST has since been upgraded to a configuration using ~ 85 electrodes, or roughly 100 KL-modes. As mentioned earlier, image-restoration is typically performed using MFBD with a mode limit of ~ 40 , so that the amplitude of KL-modes between $l = 40$ and $l = 100$ in the residual wave fronts is unknown. We propose that the average correction efficiency of the AO can be computed from the following procedure: (i) the r_0 values are first used to simulate wave fronts obeying Kolmogorov statistics; (ii) the corresponding transfer functions computed through Eq. (3.2) & Eq. (3.3) are used to degrade an image synthesised from MHD simulations; (iii) both the sets of observations (synthetic and actual) are restored using MFBD (which returns the mode amplitudes); (iv) the ratio of the standard deviations of the mode amplitudes (Eq. 3.11) in both the restorations yields the efficiency of the AO as a function of the mode. This efficiency is mathematically expressed as:

$$\epsilon_l^{AO} = 1 - (\sigma_l^{obs} / \sigma_l^{syn}), \quad (3.11)$$

where l denotes the mode number, and σ_l^{syn} and σ_l^{obs} are standard deviations of the mode amplitudes returned by MFBD restoration of the synthetic and original recorded observations, respectively. Interpretation of Eq. (3.11) is straightforward for the trivial cases. For example, if the recorded observations are found to not have any degradation caused by mode l , the standard deviation for mode l computed from image restoration would ideally

be zero. This then implies that the AO perfectly compensated mode l in the incident wave fronts ($\epsilon_l^{AO} = 1$).

A potential source of error in the calculation of ϵ_l^{AO} is the assumption that MFBD works identically on the input observations, irrespective of the state of their degradation. To address this issue, the procedure outlined above can be followed iteratively - after the first round of ϵ_l^{AO} are found, these can be used to subtract modes from the incident wave fronts. These partially compensated wave fronts can then be used to generate another set of degraded observations followed by another round of image-restoration, and the cycle can be followed until the computed efficiencies are found to converge. Once a converged set of ϵ_l^{AO} are found, residual stray light in the observations is estimated by first perfectly subtracting all modes with $l < M$, followed by subtracting modes with $l > M$ with efficiency ϵ_l^{AO} . The residual wave fronts thus generated are largely dominated by higher-order aberrations, and they approximate the amount of residual stray light still present in the observations.

3.5 Kolmogorov phase screens

A frequent approach to characterizing AO-systems is through the use of Kolmogorov phase screens, which are simulations of the spatial distribution of phase errors (wave fronts) incident on the telescope. These simulations are statistical in nature since modelling the exact propagation of a wave front requires knowledge of the refractive index at all spatial locations within the path of the wave front. The statistical properties of these Kolmogorov phase screens are well established in the works of Noll (1976), McGlamery (1976), Lane et al. (1992), and Glindemann et al. (1993). They conform to the Kolmogorov-Obukhov power law, and can be numerically simulated (Nagaraju and Feller 2012) as a function of r_0 :

$$\Gamma(\vec{k}) = 0.023(D/r_0)^{-5/3}|\vec{k}|^{-\beta}, \quad (3.12)$$

where $\Gamma(\vec{k})$ is the power at spatial frequency \vec{k} , D is the diameter of the phase screen, and $\beta = 11/3$. Fig. 3.1 shows examples of such phase screens simulated over a circular aperture of 1 m diameter. The mean value of all wave fronts has been subtracted, but no other modes have been removed. The phase screens are then used to compute the PSFs with which the synthetic MHD-generated images are degraded, and an appropriate amount of noise, by comparison with slit-jaw observations for example, is added to the synthetic data. We make a note that the validity of the MHD simulations is irrelevant as we are only interested in the synthetic images. Restoring the synthetic data and the original recorded observations with MFBD facilitates a comparison of their respective mode amplitudes.

3.6 Observations and data reduction

The dataset used in this paper was obtained on 28 June 2016 at the SST (Scharmer et al. 2003b), using the TRIPPEL spectrograph, a detailed description of which has been provided by Kiselman et al. (2011a). A fast polarimeter designed for slit-spectra - based

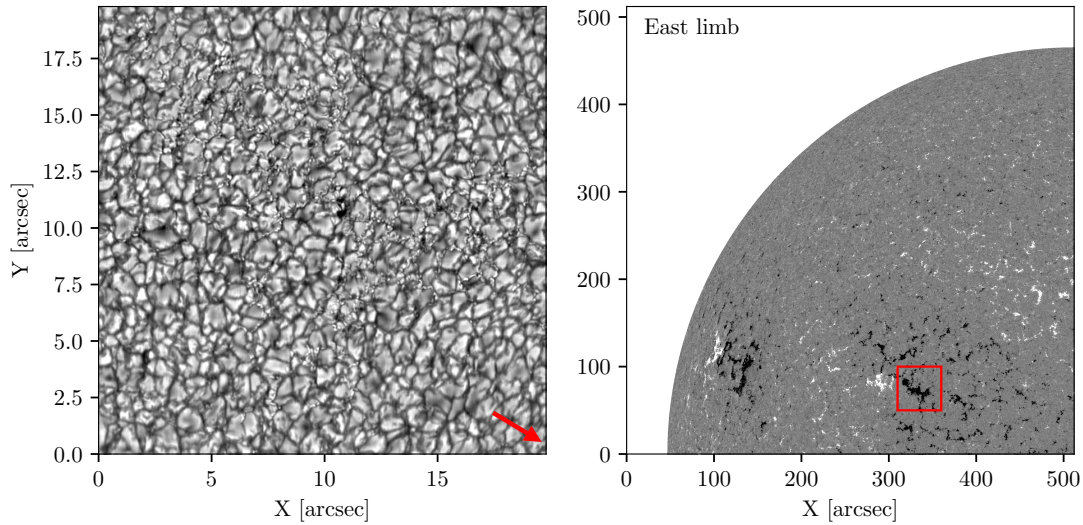


Figure 3.2: Panels showing the FOV and its location with respect to the full solar disk. *Left*: Continuum intensity image from the restored observations. The red arrow points towards the disk centre. *Right*: Line-of-sight magnetogram from HMI taken at approximately the same time. The red box highlights the FOV of the observations.

on the concept of FSP (Iglesias et al. 2016a) - was installed and used during the same campaign (TRIPPEL-SP, Doerr et. al 2019, in prep). The scan was made under moderate seeing conditions with the help of an AO consisting of an 85-electrode bi-morph mirror, a Shack-Hartmann wave-front-Sensor (WFS), a correlation tracker, and a separate mirror for tip-tilt adjustments. The AO reported an average Fried parameter value of 13 cm over the duration of the scan.

Two Jai SP20000 CMOS cameras were used for recording the slit-jaw images, whereas the spectra were recorded using two Jai SP12000 CMOS cameras. The latter allowed 4-Mpixel frames to be recorded at a rate of up to 400 Hz, the designed modulation rate of the FSP modulator. All cameras were synchronised using an external trigger signal. Although frames were recorded with a spatial sampling of $0.044''$, the sampling of the restored slit-spectra was scaled down to $0.06''$ - corresponding to the critical sampling of the SST at 6300 \AA .

3.6.1 Image restoration

The slit-jaw frames were restored in bursts of 2000 frames (5 s) with a temporal overlap of 3.75 s. As indicated in earlier sections, the restoration was performed over a grid of patches that were $128 \times 128 \text{ pixel}^2$ in size, with an overlap of $118 \times 118 \text{ pixel}^2$. The PSFs returned by MFBD for each patch were interpolated across the length of the slit. Karhunen-Loève modes were used as the basis functions, and the mode limit for the restorations was set to $M = 45$. As outlined in Sec. (3.3), the values of the PSFs were used to construct the matrix \hat{A} , and subsequently restore the data recorded by the spectral camera.

The restored slit-spectra cover a $53'' \times 53''$ FOV around a mostly uni-polar active re-

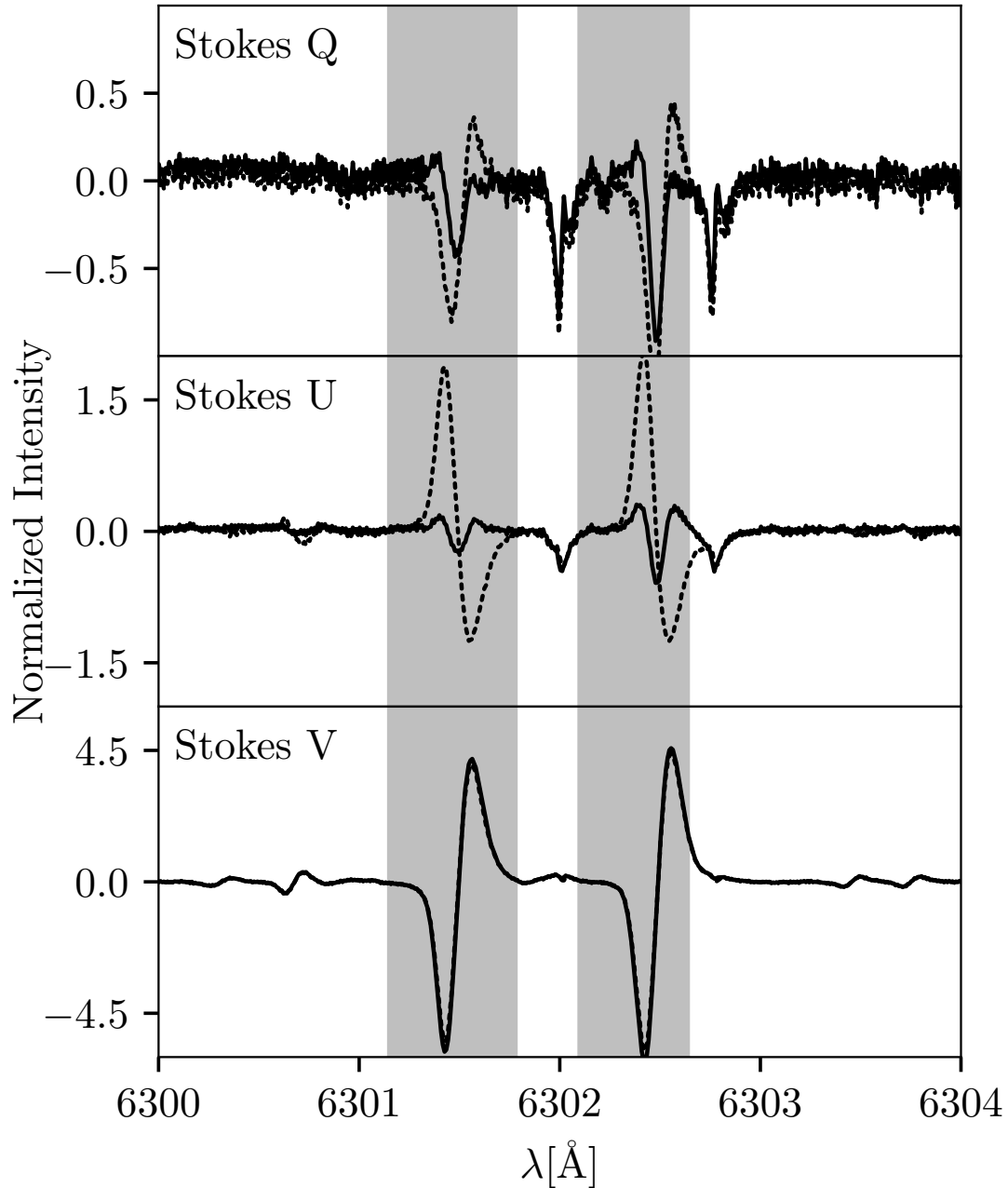


Figure 3.3: *Top to bottom:* Stokes Q , U , and V profiles averaged over the FOV. The dotted lines and solid lines show the spectra before and after crosstalk correction, respectively. The grey shaded areas indicate the wavelengths over which the dot products are computed. The units of intensity are arbitrary, and the profiles are not normalised with respect to Stokes I .

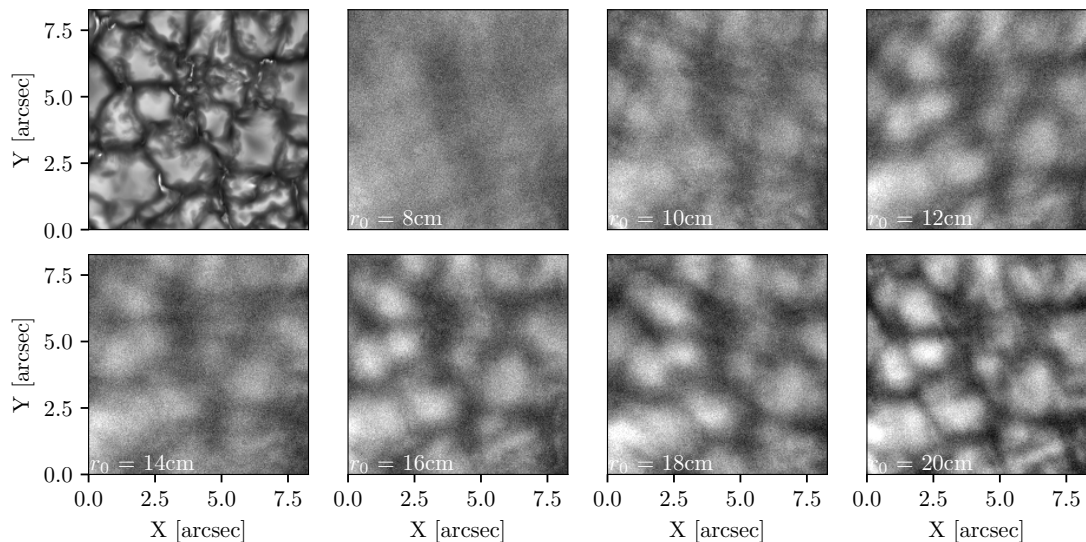


Figure 3.4: Panels showing degraded images synthesised from an MHD simulation at a continuum wavelength near 6300 \AA for different values of r_0 (mentioned in the panels). The grey scales of the degraded images are identical. The grey scale range of the undegraded image has been enlarged to avoid extreme contrasts. The sampling in all images is $0.044''$. *Top left*: Undegraded image (no added noise) corresponding to $r_0 = \infty$.

gion Plage, which is located towards the east limb at a heliocentric angle of 23 degrees ($\mu = 0.92$). The left panel in Fig. 3.2 shows a Stokes I image from the restored dataset, extracted at a continuum wavelength near 6296.0 \AA . The spectral window of the observations ranges from 6288.0 \AA to 6304.0 \AA , with a sampling of 8.6 m\AA . The wavelengths were calibrated by fitting the flat-field (obtained at disk centre) using a least-squares method to the standard FTS spectrum from Delbouille et al. (1973a). A total of 16 usable solar spectral lines were identified in the spectral window, including the iron pair at 6301.5 \AA and 6302.5 \AA . On the panel in the right of Fig. 3.2, a LOS magnetogram from HMI (Scherrer et al. 2012) is displayed for context.

3.6.2 Crosstalk and grey stray light

The restored images indicated the presence of crosstalk from $I \rightarrow Q, U, V$ and from $V \rightarrow Q, U$, a consequence of neglecting the polarizing effects of the telescope optics so far. Although models of the Mueller matrix of SST exist, we found it convenient to apply ad hoc corrections to the spectra. The crosstalk from $I \rightarrow Q, U, V$ was corrected by subtracting the average offsets (averaged over the FOV at continuum wavelengths) of Stokes Q, U , and V (normalised with respect to Stokes I). To remove crosstalk from Stokes V , we parameterised the Stokes vectors on the Poincaré sphere, and rotated the Stokes components such that the FOV-averaged Stokes Q, U , and V were symmetric, symmetric, and anti-symmetric in wavelength with respect to the line-centres, respectively. In doing so, we assume that the core of the plage makes the dominant contribution to the Stokes V spectra, and that in these regions, gradients in the line-of-sight velocities and magnetic fields are not too strong to produce significant intrinsic asymmetry. The shaded region

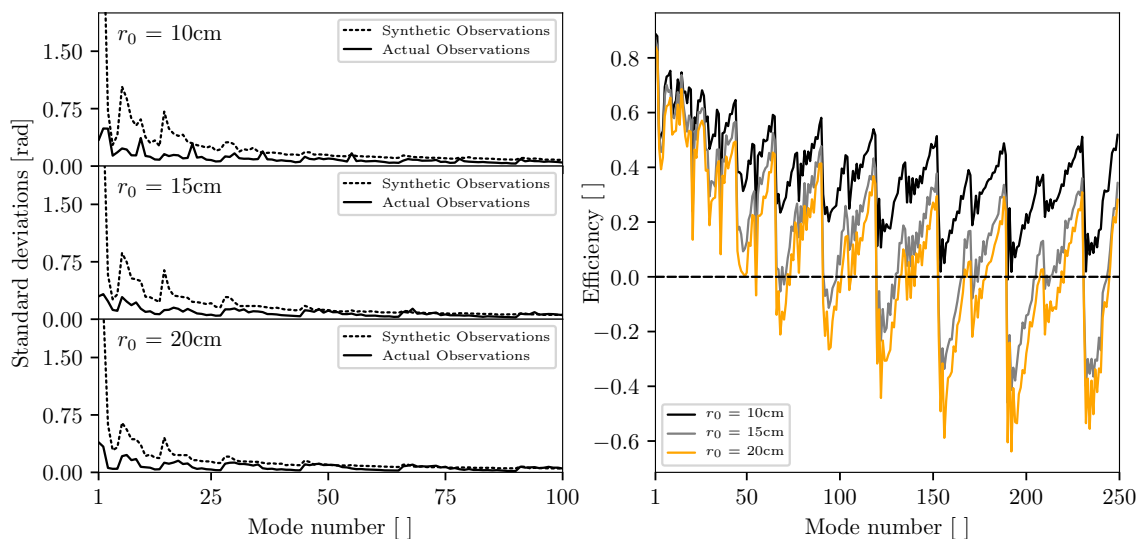


Figure 3.5: Plots of quantities obtained from MFBF restorations. *Left*: Standard deviation of mode amplitudes plotted as a function of mode number. Mode amplitudes were obtained from MFBF restoration of degraded images. Only up to 100 modes are shown here. *Right*: Average efficiency of the AO obtained from Eq. (3.11) plotted for different different values of r_0

indicates weighting of the profiles to include only solar lines in the (anti)symmetrization procedure. Since most of the crosstalk is from $V \rightarrow Q, U$, the linear polarization signals look significantly different after crosstalk removal, while Stokes V remains largely unchanged.

To remove the wavelength-independent component of the scattered light possibly caused by the extended wings of the spectral PSF (spectral veil, (Borrero, J. M. et al. 2016)), we make the assumption that the spectral PSF of the instrument is approximated to first order by a gaussian kernel with an initial guess value for its Full-Width Half Maxima (FWHM). The flat-field spectra obtained at disk centre is then expressed as the sum of the standard FTS spectra convolved with this gaussian kernel, and the additive spectral veil (expressed as a fraction of the continuum intensity). We then retrieved, both the FWHM of the gaussian kernel and the additive component, by iteratively fitting the flat-field spectra using a χ^2 minimization method. The FWHM was found to be $41\text{m}\text{\AA}$ and the fraction of spectral veil was found to be 5% of the continuum intensity.

3.6.3 Fried parameter

In closed-loop operation of the AO at the SST, an r_0 value for every second is computed from the voltages output to the DM-electrodes, as well as the variance of residual shifts of the 24×24 pixel² sub-images in four select sub-apertures, similar to a Differential Image Motion Monitor (Sarazin and Roddier 1990). Further, another concurrent set of r_0 values are also reported using the same method, but with smaller 8×8 pixel² sub-images. Since cross-correlations between larger images are more sensitive to shifts that are global, the values of r_0 computed from the 24×24 pixel² sub-images are biased more towards

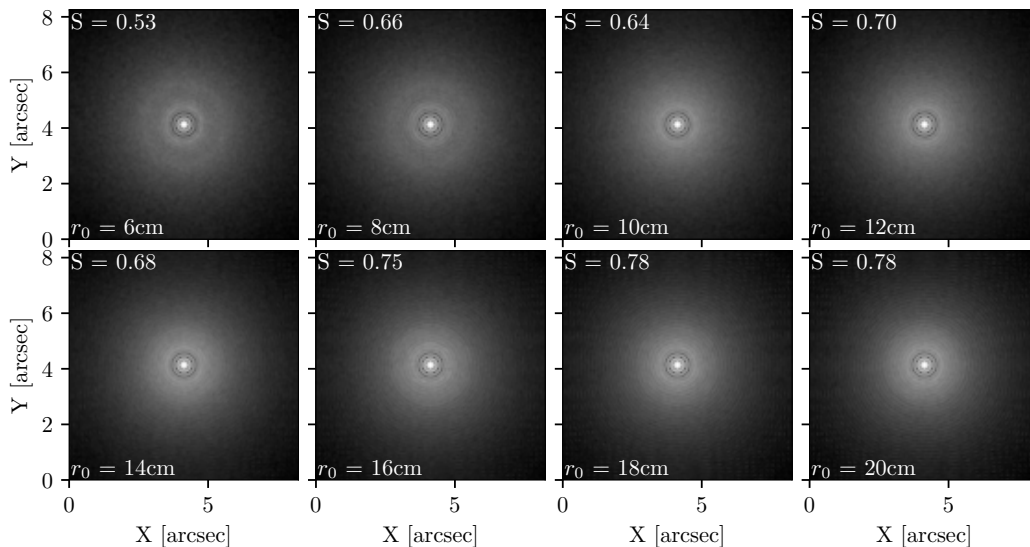


Figure 3.6: Stray-light PSFs for different r_0 , computed from the residual phase screens. The Strehl ratios of the PSFs are indicated in top left of each panel. At $r_0 = 20$ cm the radius encircling 90% energy is around $1.1''$.

ground-layer seeing that is shared by the full FOV. To avoid this bias, we use the values of r_0 computed from the 8×8 pixel² sub-images instead, and consider these to be more representative of seeing originating in both the ground and upper layers.

3.6.4 Calculating the stray-light PSF

An ensemble of 2000 Kolmogorov phase screens were created for each value of r_0 between $r_0 = 6$ cm and $r_0 = 21$ cm in steps of 1 cm. A snapshot from an MHD simulation of a quiet Sun, performed with MURaM (Vögler et al. 2005b), was then used to synthesise an image at a continuum wavelength near 6300\AA with the SPINOR radiative transfer code (Frutiger et al. 2000b). The synthesised image was subsequently degraded with the transfer functions corresponding to each of the 2000 Kolmogorov phase screens simulated for each r_0 , followed by the addition of Poisson noise to each of the degraded images. The amount of added noise was calibrated from the power-spectra of the slit-jaw images in the recorded observations. Fig. 3.4 shows a panel of these degraded images for the binned values of r_0 .

We then setup parallel image restorations of the synthetic degraded data generated above, and the recorded observations. The mode limit used in the restorations was set to $M = 250$. Since MFBD is applied on AO-compensated data in practice, we avoided restoring the synthetic data for $r_0 < 10$ cm. Further, due to the increased mode limit, the restoration of the recorded observations was constrained to the patch at the centre of the FOV. The implications of this restriction are that the stray-light PSFs that we compute would likely underestimate the residual stray-light contamination in the edges of the FOV.

MFBD returns the fitted mode amplitudes for each KL-mode, and for each degraded image. This allowed us to compute their standard deviations, which are plotted in the left panel of Fig. 3.5 for $r_0 = 5, 10, 20$ cm. The dotted and solid standard-deviation

curves correspond to the synthetic degraded data, and the original recorded observations, respectively. Only the first $M = 100$ modes are shown to magnify the behaviour of these curves at the lower orders, but they continue to decrease all the way upto mode $M = 250$. It is immediately seen that the standard deviations of the mode amplitudes in the recorded observations are lower than those corresponding to synthetic data, as it should be since the recorded observations are AO-compensated while the synthetic data are not AO-compensated. Another point to note from these curves is that the standard deviations of the synthetic degraded data decrease more rapidly than the recorded observations. This suggests that the AO-system at the SST works to keep the level of residual degradation in the observations fairly stable, irrespective of the seeing conditions.

From the standard-deviation curves, we computed the efficiency of the AO-system as described by Eq. (3.11), for every second of the scan. The panel on the right of Fig. 3.5 shows the computed efficiency of the AO (ϵ_l^{AO}) as a function of the basis mode, averaged over the realizations for $r_0 = 5, 10, 15$ cm. We now discuss the trends and features of these efficiency curves.

The first is the presence of a periodic saw-tooth pattern, observable also in the standard-deviation curves although not as strongly. These peaks correspond to the radial KL-modes, and may be caused by the ordering of the KL-basis modes. Since the radial KL-modes correspond to fluctuations at a lower spatial frequency compared to the preceding and succeeding azimuthal modes, they would always have more power according to the Kolmogorov-Obukhov power law. However, these peaks should partly cancel each other out in the efficiency curves as efficiency is obtained as a ratio of standard deviations. As to why they are very prominent is not fully clear. A possible cause may be that the MFBD restoration is somewhat sensitive to the level of residual degradation in the data. An approach to circumvent this issue would be to use an iterative scheme, where AO-efficiencies at a given iteration are used to simulate AO-compensation on the fully uncompensated phase screens, and thereby generate another dataset. Upon restoring this dataset with MFBD again, and comparing the resulting standard deviations with the observations, one can arrive at a correction to the AO-efficiencies. The procedure can be repeated iteratively until the AO-efficiencies are found to converge. In our application, we noted that AO-efficiencies were usually overestimated at the very first iteration, and therefore the stray-light PSFs corresponding to this iteration likely underestimated the amount of residual degradation. However, upon subsequently deconvolving the data, we noted the amplification of artefacts in the spectra. The more aggressive the stray-light PSF, the larger the artefacts were amplified beyond the noise level. The properties of these artefacts are further discussed in Sec. (3.7). In order to avoid these artefacts, we therefore considered the stray-light PSFs obtained at the very first iteration to be final. We note that owing to this choice, we may slightly underestimate the amount of residual stray light in our slit spectra.

The second is the indication that the AO continues to compensate very high-order modes consistently, particularly when the seeing is poor. While it is possible that certain higher-order modes are able to be compensated by the AO, the indication that modes upto $L = 250$ are corrected with an efficiency averaging 30% when $r_0 = 5$ cm could also be due to theoretical errors in the variances of mode amplitudes in the simulated phase screens. For example, modifications to the exponent β in Eq. (3.12) have been suggested in literature (Nicholls et al. 1995, Rao et al. 2000) with $2 < \beta < 4$, implying that the

stray-light correction that we perform could be both an underestimation ($\beta = 2$) or an overestimation ($\beta = 4$). Another factor that affects the standard-deviation curves are errors in r_0 . Ideally, for a completely unbiased estimate of r_0 , the size of the sub-images in the WFS should be smaller, still, than 8×8 pixel². However, a lower bound exists as the AO cannot lock onto regions without sufficient intensity contrast. Consequently, the r_0 that is computed from the cross-correlation of these sub-images may deviate from the true value at any given time. The third feature of the AO-efficiency curves is that they also appear to take on negative values. Going back to the standard-deviation curves, this implies that the recorded observations have more degradation in the higher-orders than that caused by completely uncompensated Kolmogorov wave fronts! One possible explanation for this effect is that the AO-mirror adds spurious high-order aberrations to the incident wave fronts. This may be because the mirror cannot exactly reproduce the Zernike or KL-basis modes, leading to the amplification of high-order modes in the residual wave fronts.

Despite some of the surprising results, the method outlines a self-consistent way of computing the performance of the AO-system from the recorded observations themselves. Since the slit spectra are AO-compensated and have been restored with MFBD, the amount of residual degradation in the slit spectra were estimated in the following way - first, modes until $M = 45$ were subtracted completely from the fully uncompensated phase screens. This step simulates the joint correction of AO and MFBD to the first 45 KL-modes, which is assumed to be perfect. In the next step, modes from $M = 45$ to $M = 250$ were removed using the AO-efficiencies:

$$\phi_R = \phi_S - \sum_{l=1}^{45} C_l Z_l - \sum_{l=46}^{250} \epsilon_l^{AO} C_l Z_l. \quad (3.13)$$

Here, ϕ_R is the residual wave front, ϕ_S is the simulated wave front, and C_l is the amplitude of mode l . The PSFs corresponding to the residual wave fronts were averaged over the realizations to yield a smooth stray-light PSF for every second of the scan. Following this, the stray-light PSFs were also running-averaged in time according to the weights specified in the matrix \hat{A} , and reduced to one stray-light PSF per row of the FOV (row is the scan-direction). These stray-light PSFs are displayed in Fig. 3.6 for different values of r_0 in log scale. The Strehl ratios of the PSFs are indicated in the top left of each panel, and vary from 50% in poor seeing to approximately 80% in good seeing.

3.7 Results and analysis

Following the procedure outlined in Sec. (3.3), the Stokes profiles were first converted to modulated intensities using a balanced modulation scheme. The four modulated intensities were then subsequently deconvolved with an airy-disk PSF corresponding to the diffraction limit of the aperture of the SST, at each wavelength. To perform the deconvolution, the Lucy-Richardson scheme was used. The deconvolution was non-regularised and terminated after 20 iterations as tests with synthetic data indicated that convergence is achieved quickly. We now discuss the effects of the stray-light removal procedure.

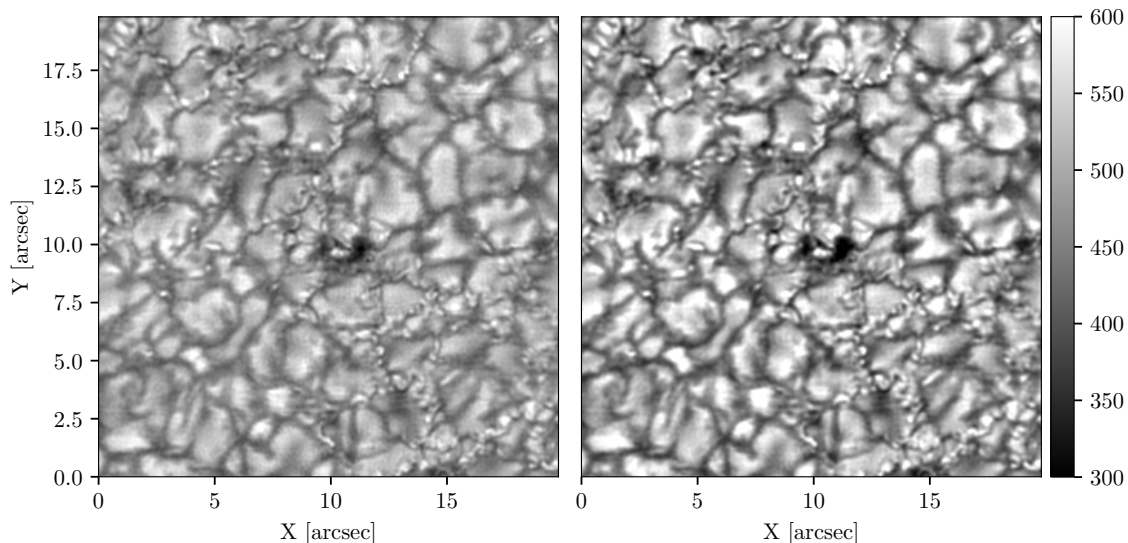


Figure 3.7: Comparison of the slit spectra at a continuum wavelength near 6300 \AA , before and after stray-light deconvolution. The grey scale has been kept uniform across both images, and the units of intensity shown here are arbitrary. The images shown here are at the centre of the larger FOV.

3.7.1 Effects on RMS granulation contrast

After deconvolution with the stray-light PSF, RMS granulation contrasts were found to increase to approximately to 12.3% in the quiet Sun, from 9.0% for the MFBD restored data. In Fig. 3.7, two continuum intensity images of the centre of the FOV are shown before (left) and after (right) the deconvolution. The grey scale has been kept equal so that the increase in contrast is readily visible in the deconvolved spectra. Since the method we followed works best at the centre of the FOV, the increase in contrast at the edges of the FOV is lower than it theoretically should be.

In order to understand the reduction of stray light in our data, a comparison with synthetic images is required. We therefore synthesised an image at a continuum wavelength near 6300 \AA (same region as our spectra) from an MHD simulation, and degraded it to 86.5% of the diffraction limit of the telescope. This percentage was extracted from the power spectrum of deconvolved observations, and locating the spatial frequency above which noise dominates. Comparing the RMS contrasts, we found that a deficiency of 2.5 – 3% still exists in our data. Since we are exclusively removing stray light due to higher-order aberrations, contributions from instrumental sources, and from atmospheric scattering still exist. However, as to how much they contribute to an increase in RMS contrast is still unclear.

3.7.2 Effects on spectra

The deconvolution was found to affect the shape of spectral lines significantly. Fig. 3.8 shows a comparison of the spatially averaged, normalised line profiles before and after the deconvolution in granules (top) and inter-granular lanes (bottom) for the Fe I line at

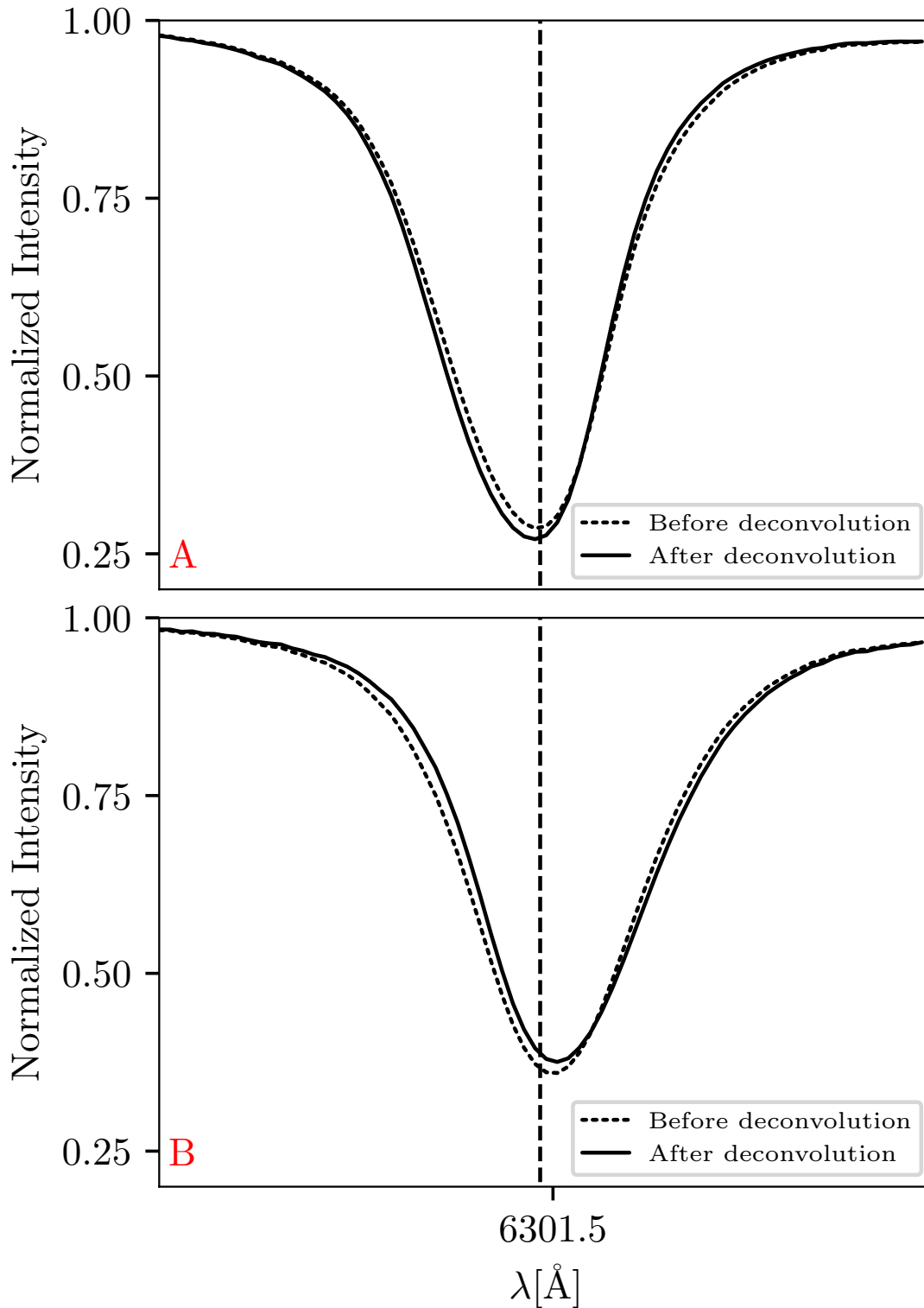


Figure 3.8: **A:** Comparison of the average line profile in granules before and after the deconvolution. Only the Fe I spectral line at 6301.5 \AA is shown here to magnify the differences. **B:** Comparison reproduced for the inter-granular lanes. The vertical scale for both plots have been kept the same.

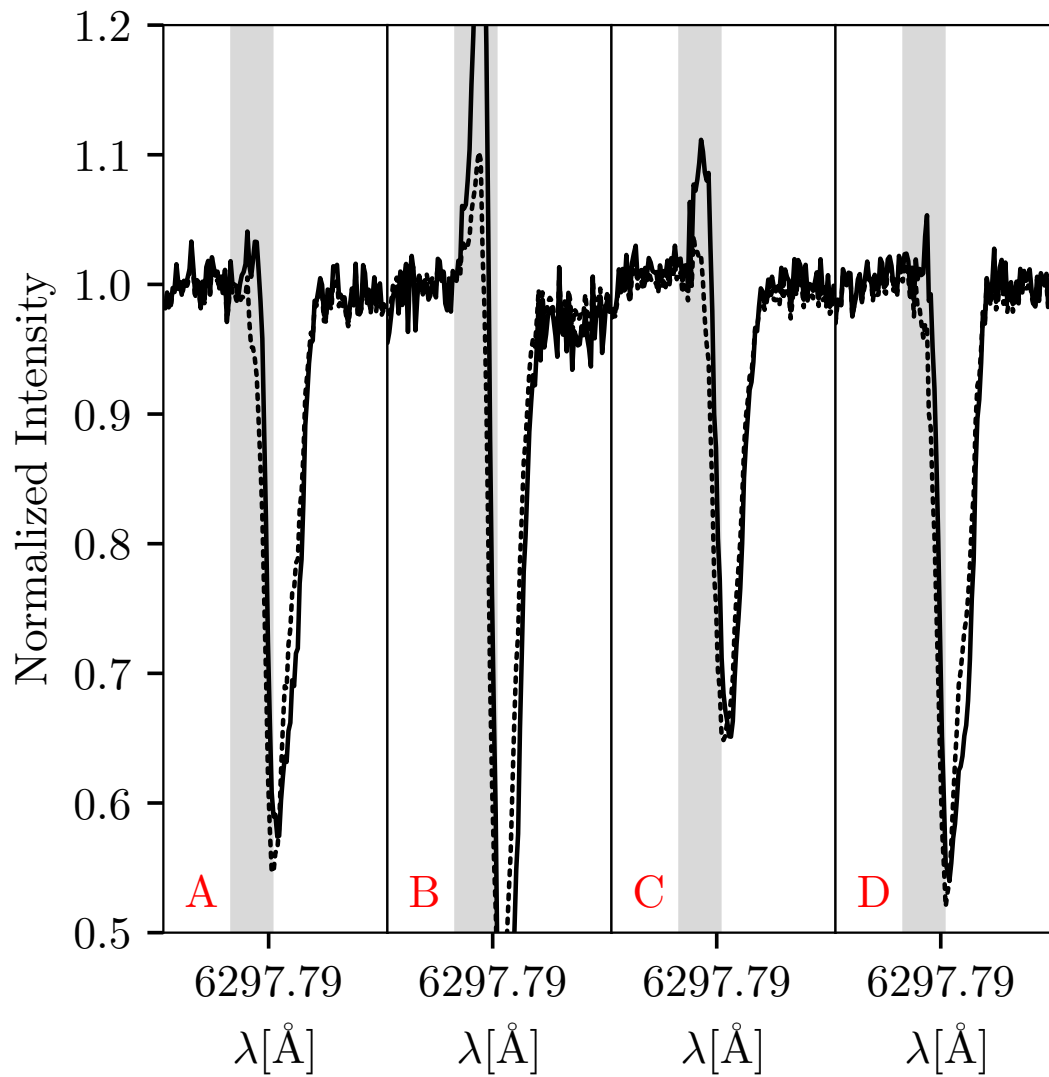


Figure 3.9: Line profiles of Fe I at 6297 Å shown before (dotted) and after (solid) the deconvolution in certain pixels. The grey shaded region highlights the location of the spike in the blue wing of the spectral line.

6301.5 Å. The selection of granules and inter-granular lanes was made on the basis of an intensity threshold. Although the differences are diminished due to the averaging, certain characteristic changes are visible.

The depth of spectral lines in the granules was found to increase, as well as become more blue-shifted. This is because the stray-light profile in granules is composed of contributions from the surrounding inter-granular lanes which are comparatively shallower, and red-shifted due to the presence of down-flows. Subtracting these contributions, therefore, causes the spectral lines to become deeper and more blue-shifted in the granules. The converse holds true for the inter-granular lanes, where removing the stray-light contribution from granules causes the spectral lines within inter-granular lanes to become shallower and more red-shifted. These effects collectively indicate that temperature gradients, as well as line-of-sight velocities in both granules, and inter-granular lanes are intrinsically larger than what would be observed without stray-light correction.

In the plage regions, the deconvolution was found to increase the amplitude of the Stokes V lobes, while decreasing the depth of spectral lines in Stokes I . Since, Stokes V is roughly proportional to the derivative of Stokes I (under the weak-field approximation), deconvolution increases the deduced field strengths of the plage. However, several degeneracies in the atmospheric parameters affecting the shape of the spectral lines exist, and an accurate quantification of the effects of stray-light removal on spectropolarimetric data requires spectropolarimetric inversions.

The deconvolution was also found to amplify artefacts in certain pixels. Fig. 3.9 shows a spectral line at 6297.79 Å in four different pixels (labelled A-D). The dotted and solid lines show the spectral line before and after stray-light deconvolution, respectively. In other words, the dotted line represents slit spectra that were restored with MFBD, and the solid lines represent slit-spectra that were restored with MFBD, followed by the stray-light deconvolution. The grey shaded regions indicate the location in the blue wing of the spectra line where a conspicuous spike appears. These spikes were found to be visible in all but the telluric lines, and their severity was found to vary. In some pixels (labelled B and C), the spike was already found in MFBD-restored data before the stray-light deconvolution. A likely cause for this may be the differential aberrations between the slit-jaw and the spectral cameras - when the slit moves or vibrates within the slit-jaw cameras' FOV during the scan. This implies that the PSFs returned by MFBD, based on the slit-jaw images alone, may not be able to precisely describe the degradation in the spectra recorded by the spectral camera. In pixels labelled A and D, it is harder to ascertain whether the spike existed before the stray-light deconvolution. Nonetheless, the stray-light deconvolution appears to have amplified it. We found the number of pixels displaying such artefacts above the noise level to be less than 0.1% of the FOV.

3.8 Discussions and conclusions

In this paper, we extended the method initially developed by Scharmer et al. (2010a) - using Kolmogorov statistics - to self consistently estimate the amount of residual stray light directly from the observations. Although we focused on slit-spectra, our method is also applicable to observations obtained with filtergraphs. We found that the RMS contrasts of granulation in our observations increased by roughly three percentage points - from 9%

to 12.5%. This is much closer to the values of contrasts found in MHD simulations. Since the RMS contrasts in MHD simulations themselves show an intrinsic variability of one percent, the discrepancy between our observations and simulations may be of the order of one to three percent.

In our method, we made several deliberate choices that theoretically lead to a slight underestimation of the residual stray light in our data for reasons of expediency, but it is possible to relax some of these constraints. For example, the estimation of the stray-light PSFs can also be performed as a function of position along the slit. One would therefore have a set of fully space variant stray-light PSFs. This requires more computational resources as multiple independent MFBD restorations need to be performed by segmenting the FOV into patches, but it would conceptually be similar to the method we have implemented here.

We note that our method only removes the component of stray light due to high-order aberrations. Stray-light contamination from instrumental sources, and optical scattering remain unknown in our observations. Progress, however, is being made in accounting for these components. Löfdahl and Scharmer (2012a) used a setup with an artificial target - situated at the primary of the focus of the telescope - to ascertain the amount of stray light originating in the post-focus optics at SST. They reported that contributions to stray light due to ghost images and scattering may be up to a few percent, in addition to the dominant contribution coming from high-order wave-front aberrations originating in the AO bimorph mirror.

Due to the lack of a comprehensive solution that accounts for all the components of stray light, our observations are still likely to contain some residual degradation. However, given that our method accounts for, and restores a good chunk of the missing contrast, we consider our observations to be suitable for spectropolarimetric inversions.

Acknowledgements

The authors would like to thank Peter Sütterlin, and Hans-Peter Dörr for their technical support and useful discussions. This project has received funding from the European Research Council (ERC) under the European Union's Horizon 2020 research and innovation program (grant agreement No. 695075) and has been supported by the BK21 plus program through the National Research Foundation (NRF) funded by the Ministry of Education of Korea. The participation of S. Saranathan was funded by the International Max Planck Research School for Solar System Science.

4 Inversions of slit-spectra

Observations of the solar spectra indicate the presence of numerous spectral lines throughout the electromagnetic wavelength range. While laboratory experiments in the 19th century confirmed these to be of spectroscopic origin, a rigorous quantitative theory describing the formation of spectral lines and the propagation of light through an ambient medium began to take shape only after the development of quantum mechanics (see for e.g. Landi Degl’Innocenti and Landolfi 2004). In the next sections of this chapter, the theory behind spectral lines is briefly reviewed, followed by an introduction to spectropolarimetric inversions. A comprehensive description of the theory behind spectral line formation and radiative transfer (in particular of polarized transfer) can be found in del Toro Iniesta (2003). In the sections that succeed, the results of the spectropolarimetric inversions on the data described and reduced in the previous chapters is presented.

4.1 Radiative transfer and spectral line formation

A beam of radiation propagating through an ambient medium such as the solar atmosphere in a given direction, is characterized by its specific intensity (I_ν), where (ν) is the frequency. If the polarization states of the beam are taken into account, additional specific intensities can be defined for all the stokes components so that the beam is well described by the full stokes vector (\mathbf{I}_ν). As the beam propagates, various physical processes may modify the stokes vector in one of three ways - extinction of the total intensity through the absorption of photons, enhancement of the total intensity through the emission of photons, or the intermixing of the stokes components through, for example, magneto-optical effects. Formally, the variation of the beam intensity with the distance (s) travelled through the medium is mathematically expressed through the equation of radiative transfer (RTE) - an energy balance equation that accounts for all physical processes that may modify the stokes vector \mathbf{I}_ν :

$$\frac{d\mathbf{I}_\nu}{ds} = -\mathbf{K}_\nu \mathbf{I}_\nu + \mathbf{J}_\nu, \quad (4.1)$$

where the subscript ν represents the frequency of the radiation, \mathbf{K} is the total absorption matrix of the medium, and \mathbf{J} is the total emission vector. Thus, the RTE is the fundamental equation that allows the computation of the emergent stokes vector of a beam of radiation that escapes the solar atmosphere. The question of how spectral lines form and what factors affect their properties is now addressed.

Consider a beam of photons at a continuum frequency i.e. a frequency that does not correspond to spectroscopic transitions of any atomic element, propagating through the

lower solar atmosphere. The contribution to the total opacity solely arises from continuum processes such as scattering that are largely independent of the photon frequency for small enough variations in the frequency, although sharp variations in opacity occur at certain frequencies corresponding to the ionization energies of the atoms and molecules in the plasma. In this case, the total intensity of the beam, as a function of the frequency, closely resembles the blackbody spectrum corresponding to the temperature(s) of the last scattering layer(s). However, at the transition frequency of any given atomic element, the total opacity of the plasma is significantly enhanced due to the availability of a large number of photon-absorbing atoms that can participate in spectroscopic transitions. The last scattering layers are then translated radially outwards to the upper cooler regions of the solar atmosphere, and the intensity of the radiation emerging from these regions is lower than the continuum values, giving rise to characteristic absorption lines in the Stokes I spectra.

The degree to which the spectroscopic transitions contribute to the total opacity is dependent on several intrinsic factors such as the oscillator strength, the effective Landé factor, the respective abundance of the atomic elements. Further, the absorption profiles of spectral lines are not Dirac-delta functions of the frequency, but are instead broadened by a number of independent physical processes. For example, the stochastic Doppler motions of atoms in the medium cause the well-known Gaussian broadening of the spectral lines near the core, while other line-damping processes such as the natural broadening, Van-der Waals broadening, and Stark broadening cause the spectral lines to have extended damped wings. Similar to the intrinsic factors, the physical conditions of the medium such as the temperature, the line-of-sight velocity, the magnetic field and their stratification may also affect the width, the depth, and the symmetry of the observed absorption profiles in Stokes I , as well as the Stokes polarization components. In general then, spectral lines encode the physical properties of the medium in their shape. Thus, given the intrinsic transition parameters and a model atmosphere, the shapes of spectral lines can be numerically computed by forward integration of the RTE. In this case, the total absorption matrix accounting is expressed as the sum of the continuum absorption and the line absorption matrix (Rees et al. 1989):

$$\mathbf{K}_\nu = \kappa_c(\mathbf{1} + \boldsymbol{\eta}_\nu) \quad (4.2)$$

for all frequencies, where κ_c denotes the continuum opacity and $\boldsymbol{\eta}_\nu$ is the line absorption matrix (Landi Degl'Innocenti and Landolfi 2004):

$$\boldsymbol{\eta}_\nu = \begin{pmatrix} \eta_I & \eta_Q & \eta_U & \eta_V \\ \eta_Q & \eta_I & \rho_V & -\rho_U \\ \eta_U & -\rho_V & \eta_I & \rho_Q \\ \eta_V & \rho_U & -\rho_Q & \eta_I \end{pmatrix}, \quad (4.3)$$

where the subscript ν has been dropped for the components of the matrix. In the presence of magnetic fields, the components of the absorption matrix account for the creation (Zeeman effect) and destruction (Hanle effect) of polarization, as well as its conversion from one form to another (magneto-optical effects). The components of the matrix are sensitive to the orientation of the magnetic field with respect to the line-of-sight:

$$\begin{aligned}\eta_I &= \frac{1}{2} \left[\eta_p \sin^2 \gamma + \frac{1}{2} (\eta_b + \eta_r) (1 + \cos^2 \gamma) \right], \\ \eta_Q &= \frac{1}{2} \left[\eta_p - \frac{1}{2} (\eta_b + \eta_r) \right] \sin^2 \gamma \sin 2\chi, \\ \eta_U &= \frac{1}{2} \left[\eta_p - \frac{1}{2} (\eta_b + \eta_r) \right] \sin^2 \gamma \cos 2\chi, \\ \eta_V &= \frac{1}{2} (\eta_b - \eta_r) \cos \gamma\end{aligned}$$

and

$$\begin{aligned}\rho_Q &= \frac{1}{2} \left[\rho_p - \frac{1}{2} (\rho_b + \rho_r) \right] \sin^2 \gamma \sin 2\chi, \\ \rho_U &= \frac{1}{2} \left[\rho_p - \frac{1}{2} (\rho_b + \rho_r) \right] \sin^2 \gamma \cos 2\chi, \\ \rho_V &= \frac{1}{2} (\rho_b - \rho_r) \cos \gamma,\end{aligned}$$

where γ specifies the angle of the magnetic field with respect to the line-of-sight and χ is the magnetic azimuth (in the plane perpendicular to the line-of-sight). The η_k and ρ_k , $k = p, b, r$ represent the general absorption profiles and the anomalous dispersion profiles respectively - given by the Voigt and Faraday-Voigt functions:

$$\begin{aligned}\eta_k &= \eta_0 \sum_M S_M^k H(a, \nu - \nu_M^k + w), \\ \rho_k &= \eta_0 \sum_M S_M^k 2F(a, \nu - \nu_M^k + w), \\ H(a, \nu) &= \frac{a}{\pi} \int_{-\infty}^{\infty} \frac{\exp(-y^2)}{(v - y)^2 + a^2} dy, \\ F(a, \nu) &= \frac{1}{2\pi} \int_{-\infty}^{\infty} \frac{\exp(-y^2)(v - y)}{(v - y)^2 + a^2} dy.\end{aligned}$$

The η_k and ρ_k account for the Zeeman splitting of the spectral line and magneto-optical effects, respectively, the S_M^k represent the unnormalized strength of the Zeeman components. The sums in the equations for ρ_k and η_k include all the components with:

$$\Delta M = M_u - M_l = \begin{cases} +1 \equiv b \\ 0 \equiv p \\ -1 \equiv r \end{cases}$$

where M_u and M_l denote the magnetic quantum numbers of the Zeeman-split lower and upper states, respectively. Further expressions for S_M^k , the damping parameter of the Voigt profile a (including Stark damping, radiation damping, and Van-der-Waal's broadening),

the shifts v_M^k , and η_0 can be found in del Toro Iniesta (2003), Landi Degl’Innocenti and Landolfi (2004), and de la Cruz Rodríguez and van Noort (2017). Thus, using the set of equations listed above, the exact shape of a spectral line corresponding to any given atomic element forming in a magnetized model atmosphere can be computed numerically.

4.2 Spectropolarimetric inversions

The term *spectropolarimetric inversions* refers to an indirect method of retrieving the physical parameters of the solar atmosphere - the temperature, the line-of-sight velocity, and the vector magnetic field - from observations. Formally, this can be represented with the following expression:

$$T(s), \mathbf{B}(s), v_{los}(s) = f^{-1}(\mathbf{I}_{obs}(v), \Theta_{atom}, \Theta_{inst}), \quad (4.4)$$

where variables on the left denote the physical parameters to be determined, $\mathbf{I}_{obs}(v)$ is the observed Stokes profile of a given region on the solar disk, Θ_{atom} are the set of intrinsic parameters for every spectral line observed in the data, and Θ_{inst} are instrumental factors that alter the observed profiles (for example, the spectral PSF). Due to the fact that different atmospheres may produce spectral lines that look relatively similar, the problem of inversions is generally a difficult one. This degeneracy is partially removed when multiple spectral lines are used in the spectropolarimetric inversions, as lines generally form in different regions of the solar atmosphere. Although analytical solutions of the inverse function (f^{-1}) do not typically exist, numerical methods can be employed to retrieve the atmospheric quantities and their stratification through the sequence of steps described below:

1. Identify the intrinsic parameters of the atomic transitions corresponding to the observed spectral lines (abundance, $\log(gf)$, Landé factor, damping constants).
2. Use the RTE to numerically synthesize the observed line profiles from an initial guess atmosphere.
3. Degrade the synthesized line-profiles with the instrumental spectral PSF (Point Spread Function).
4. Compare the shapes of the synthesized profiles with those of the observations through a suitable metric (χ^2), normalized by the noise in the observed spectra.
5. Modify the physical parameters and the stratification in the guess atmosphere so as to produce better model *fits* to the observed spectra.
6. Repeat steps 2 - 4 until the solution converges.

Over the past decades, a number of inversion codes employing different assumptions in the forward synthesis (step 2) and different techniques to update the model atmospheres have been developed. One of the first was detailed by Auer et al. (1977), who used the Milne-Eddington approximation, i.e. the source function of the medium is assumed to

vary linearly with optical depth. Although this immediately prohibits the true stratification of the physical parameters from being deduced, the RTE admits analytical solutions for the emergent intensity, making the approximation a convenient choice when rapid inversions are desired. Rewriting the RTE and the source function (S_ν) in terms of the continuum optical depth (τ):

$$\begin{aligned}\mu \frac{dI_\nu}{d\tau} &= (1 + \eta \mathbf{M}_\nu)(I_\nu - \mathbf{S}_\nu), \\ S_\nu(\tau) &= S_0 + \beta\tau,\end{aligned}$$

the Milne-Eddington approximation yields the following solutions for the components of the emergent stokes vector \mathbf{I} :

$$\begin{aligned}I &= S_0 + \mu\beta \frac{(1 + \eta M_0)}{D}, \\ Q &= -\mu\beta \frac{\eta M_1}{D}, \\ U &= -\mu\beta \frac{\eta M_2}{D}, \\ V &= -\mu\beta \frac{\eta M_3}{D},\end{aligned}$$

where η is the line-center to continuum opacity ratio, M is the absorption Mueller matrix accounting for the polarization due to the magnetic field (neglecting magneto-optical effects), and $\mu = \cos \theta$:

$$\mathbf{M} = \begin{pmatrix} M_0 & M_1 & M_2 & M_3 \\ M_1 & M_0 & 0 & 0 \\ M_2 & 0 & M_0 & 0 \\ M_3 & 0 & 0 & M_0 \end{pmatrix} \quad (4.5)$$

and

$$D = (1 + \eta M_0)^2 - \eta^2(M_1^2 + M_2^2 + M_3^2). \quad (4.6)$$

In their study, Auer et al. (1977) tested the validity of the approximation by inverting synthetic line profiles generated from a model atmosphere (HSRA) with a constant magnetic field vector and found that their inversion code retrieved the magnetic field strength to within 5% of the true value. Although an instructive approximation, the Milne-Eddington assumption falls short of reproducing the asymmetries in the line-profiles of the Stokes I spectra, as is the case in atmospheres with strong gradients in the line-of-sight velocity and the magnetic field. Following advances in computational speeds, subsequent improvements to the inversion scheme were made by Ruiz Cobo and del Toro Iniesta (1992) who developed a code that was able to retrieve the stratification of the temperature, magnetic field strength, azimuth, inclination and the line-of-sight velocity in the photosphere by implementing analytical response functions (Landi Degl'Innocenti and Landi Degl'Innocenti 1977). In their approach, they defined the χ^2 metric as:

$$\chi^2 = \frac{1}{n} \sum_{k=1}^4 \sum_{\nu} [I_k^{obs}(\nu) - I_k^{syn}(\nu)]^2, \quad (4.7)$$

where the index k denotes the Stokes component, ν the frequency, and the noise n is assumed to be a constant across the observed stokes components. In Eq. (5.7) all Stokes parameters are given equal weights for simplicity. In practice, because Stokes I , Q , U are typically much weaker than Stokes I , the former are given larger weights when computing χ^2 , so that all Stokes parameters are fit roughly equally well. The physical parameters of the model atmosphere were defined on a grid of equi-spaced optical depth locations, represented by the following vector:

$$\mathbf{A} = [T(\tau_1), T(\tau_2), \dots, T(\tau_n), \quad (4.8)$$

$$B(\tau_1), B(\tau_2), \dots, B(\tau_n), \quad (4.9)$$

$$\gamma(\tau_1), \gamma(\tau_2), \dots, \gamma(\tau_n), \quad (4.10)$$

$$\phi(\tau_1), \phi(\tau_2), \dots, \phi(\tau_n), \quad (4.11)$$

$$v_{los}(\tau_1), v_{los}(\tau_2), \dots, v_{los}(\tau_n)] \quad (4.12)$$

and analytical expressions for the response functions were derived from a first-order perturbation analysis of the RTE:

$$\delta \mathbf{I}(\nu) = \int_0^{\infty} \mathbf{R}(\nu, \tau) \delta x(\tau) d\tau$$

where $\delta x(\tau)$ denotes a perturbation to any physical parameter ($x = T, B, \dots$), and \mathbf{R} the response function (RF) vector, providing the response function for each Stokes component, which quantifies how the emergent intensities respond to perturbations in the model atmosphere. The RFs are thus equivalent to the derivatives of χ^2 with respect to the physical parameters being sought, and must be re-computed after each update to the model atmosphere. In their code, Ruiz Cobo and del Toro Iniesta (1992) implemented the Diagonal Lambda Operator (DELO) method (Rees et al. 1989) to solve the RTE for polarized light in the forward synthesis, and a regularized Levenberg-Marquardt algorithm for the minimization of the (χ^2) metric. Further, in order to reduce the number of degrees of freedom, Ruiz Cobo and del Toro Iniesta (1992) updated the model atmosphere only at specific chosen optical depth locations (nodes), while the stratification of the physical parameters between the nodes were approximated with a cubic-spline interpolation. This approach to spectropolarimetric inversions, introduced by Ruiz Cobo and del Toro Iniesta (1992), continues to be an important inversion scheme to retrieve the physical parameters of the solar atmosphere without the use of approximations on the nature of their stratification.

4.3 Introduction to facular bright points

Observations of the photometric properties of faculae¹ have revealed a complex relationship between facular contrasts and the properties of their magnetic elements, such as their lateral size, position on the solar disk (heliocentric angle), and magnetic flux densities. For example, faculae near the disk center were found to have positive contrasts in broadband observations centered around 5750Å and 8640Å, by Muller and Keil (1983) and Lawrence et al. (1988), respectively, while Topka et al. (1992) and Lawrence et al. (1993) reported negative contrasts in their observations. Similarly, the center-to-limb variations (CLVs) of these contrasts in continuum wavelengths were found to exhibit ambiguous characteristics - after finding a monotonous increase from center-to-limb, Sánchez Cuberes et al. (2002), Ortiz et al. (2002) and Berger et al. (2007) discovered a contrast peak around $\mu = 0.2$, while the existence of such a peak was disputed by Chapman and Klabunde (1982), Lawrence and Chapman (1988), Nishikawa and Hirayama (1990). On the other hand, Keller (1992) and Topka et al. (1997) investigated the dependence of facular contrasts (in the continuum) on the size of the magnetic elements, concluding that elements smaller than 300km in diameter were, on average, brighter than the quiet Sun. Further, they also investigated the dependence of these contrasts on the magnetic flux densities, a relationship that has been updated, more recently, by (Kobel et al. 2011, Yeo et al. 2013, Kahil et al. 2017) using high-resolution space-based observations. In general, the studies have indicated that for small-scale magnetic elements ($\sim 0.1''$), stronger magnetic flux densities lead to higher contrasts in the continuum. However, accurate quantitative descriptions are still difficult, on account of the role played by instrumental resolution.

From studies of the atmospheres in faculae using spectropolarimetric inversions, several important points are noted. Firstly, the magnetic elements in faculae have been associated with weak temperature gradients, typically appearing brighter than the quiet Sun at equal optical depths in the upper photospheric layers (Buehler et al. 2015). This is evidenced by the weakening of photospheric spectral lines, although other physical parameters affect the line-depths albeit to a lesser degree. Secondly, in high-resolution observations, facular magnetic elements have been reported to show sub-structures in temperature, with the hottest regions occurring more at the edges of the magnetic flux patches than at the center (Buehler et al. 2015). Thirdly, Martínez Pillet et al. (1997), Narayan and Scharmer (2010) and Buehler et al. (2015) found systematic downflows and strong line-of-sight velocity gradients at the boundaries of some of the magnetic elements. Such downflows have been theorized to overturn and drag with them some of the magnetic fields in the flux elements back into the solar interior. This would create opposite polarity patches adjacent to the source fields. However, the detection of such fields in spectropolarimetric observations has so far been difficult owing to finite polarimetric sensitivities, and a limited number of spectral lines used in inversions. On the other hand, the magnetic fields in plages are currently understood to be largely vertical with respect to the local solar surface (inclination up to 15°) at the photosphere (Martínez Pillet et al. 1997), while no preferred direction for their azimuths has been conclusively established. These fields are found to expand rapidly with height, an interpretation supported by (Martínez Pillet

¹The terms *plage* and *faculae* are used interchangeably to refer to the same active region components regardless of their position on the solar disk, and/or wavelength of observations.

et al. 1997) who find the strengths of magnetic fields to decrease with heliocentric angle in their Milne-Eddington inversions.

As is evident, small-scale magnetic elements in plages participate in a variety of physical processes, and are key components of surface magnetism in the Sun. They are currently modelled as thin, cylindrical flux-tubes (see Solanki 1993, for a review), the magnetic fields within which are thought to be intensified by the convective collapse instability (Parker 1978, Spruit 1979, Grossmann-Doerth et al. 1998) to kG values. Eventually, the flux-tubes reach an equilibrium state, where the internal gas density is reduced due to pressure equilibrium with the surrounding granular walls. This causes a reduction in the internal opacity i.e. the optical depth surfaces within the flux-tubes shift downward to deeper layers. When such flux-tubes are viewed along a line-of-sight that is oblique to their axis, the reduced opacity allows radiation from the walls of the limbward granule to escape into the line-of-sight i.e. the hot wall effect (Spruit 1976). On the other hand, if the flux-tubes have small diameters, radiation from the walls may heat the interiors of the flux-tubes, or scatter into the line-of-sight. The differences between the two scenarios are reflected in the morphology of the contrasts. In the former, the brightness appear elongated by $\sim 0.5''$ (Lites et al. 2004), aligned diskward, while in the latter, the brightness is compact and point-like. These have been qualitatively reproduced in 3D magneto-convective simulations performed, for example by Keller et al. (2004), Carlsson et al. (2004) and Okunev and Kneer (2005). Further, the temporal evolution of such flux-tubes was studied by De Pontieu et al. (2006), who used observations from the Swedish Solar Telescope (SST, Scharmer et al. (2003a)), concluding that the evolution of small-scale magnetic elements in faculae are strongly driven by the surrounding convection. However, quantitative uncertainties regarding the energy transport and dissipation mechanisms within these magnetic elements still exist. The focus of this thesis is the occurrence of several facular bright points, near the larger distributions of magnetic flux, that were identified in the cores of the neutral-iron spectral lines at 6297.79\AA , 6301.49\AA , and 6302.50\AA . Such bright points in faculae have been previously studied in observational data by Kobel et al. (2009), Kobel et al. (2014), Riethmüller et al. (2014), and Riethmüller and Solanki (2017). In the next section, the results of the inversions of the slit-spectra are presented, with particular emphasis on the atmospheres in facular bright points.

4.4 Inversions of facular bright points

In the slit-spectra, a total of 17 usable photospheric spectral lines were identified from the VALD (Vienna Atomic Line Database), NIST, and Kurucz (Kurucz and Bell 1995) atomic databases, including the Fe I iron pair at 6301.5\AA and 6302.5\AA . These lines were identified by synthesizing spectra using the standard HSRA (Gingerich et al. 1971) quiet Sun reference atmosphere, and comparing their strengths with respect to the standard spectrum obtained with the Jungfraujoeh atlas (Delbouille et al. 1973b). The abundance of each element in the synthesis were taken from Asplund et al. (2009). Further, spectral lines that were either blended with telluric lines, or corresponded to the atomic transitions of doubly (or more) ionized atoms were excluded from the inversions.

The numerical code used for the inversions (SPINOR-LTE), developed by Frutiger et al. (2000a), allows for a set of given atmospheric parameters to be independently deduced at multiple optical depths (nodes), while the values of the atmospheric parameters between the nodes are interpolated onto a finer grid of optical depths using a cubic-spline interpolation. Similar to the inversion scheme adopted by Ruiz Cobo and del Toro Iniesta (1992), the code also computes the response functions for each Stokes component, and the χ^2 metric is minimized through the Levenberg-Marquardt regularized algorithm. Both the noise in the respective Stokes profiles and the spectral PSF of the instrument were taken into account when comparing the synthesized and observed spectra. Since a partial correction for stray-light in the data have been made, the assumption that the atmospheres pertaining to each pixel are independent can be made - the so-called 1.5D approach. Three nodes for the temperature, the magnetic field strength, the inclination, the line-of-sight velocity and microturbulence, and one node for azimuth were chosen. This particular configuration was found to produce optimal results, given the number of spectral lines selected for inversions.

Since the atomic parameters of the spectral lines are generally determined to different accuracies (log(*gf*), collision broadening, stark broadening, etc.), it is necessary to calibrate these intrinsic parameters in order to obtain better quality fits. For this step, a snapshot of a quiet Sun atmosphere from an MHD simulation with an average $B_{\text{LOS}} = 30$ Gauss was used to generate synthetic quiet Sun spectral profiles. The shapes of these synthetic line-profiles, averaged over the FOV of the snapshot, were then iteratively matched to those of standard FTS spectra by tuning the $\log(gf)$ and the damping constants until a satisfactory match was obtained. Further, in order to account for the broadening of spectral lines in the FTS spectra due to granulation and p-mode oscillations, the synthesized line profiles were convolved with a Gaussian kernel with a FWHM of 1 km/s at each step of the iteration. To select the positions of the nodes in $\log(\tau)$, test inversions were made with the objective of removing salt-and-pepper noise in the inverted atmospheres as well as improving the quality of the fits to the observed spectra. In addition to the photosphere ($\log(\tau) = 0.0$), a middle node at $\log(\tau) = -1.0$ and an upper node at $\log(\tau) = -2.4$ were found to produce optimal results. Lastly, since the χ^2 minimization algorithm may settle into a local minimum, periodic smoothing - after every 7 iterations - of the inverted atmospheres was found to be helpful in improving the results of the inversions. The iterations were continued until the inverted atmospheres did not appreciably change, and the χ^2 metric stabilized.

The top and bottom panels of Fig. 4.2 display the images corresponding to the Fe I 6297.79Å, obtained as the core intensity at each pixel. The locations of these regions within the larger FOV have been indicated through the offsets in their respective axes. In addition to this spectral line, the Fe I line pair at 6301.49Å and 6302.50Å were also used to identify bright points within the field of view, using independent intensity and area thresholds. These bright points have been highlighted in Fig. 3.2 using circular reticles, color coded by their respective spectral line of detection. We note that the bright points are not always uniformly detected in all three spectral lines, and also draw attention to the slight offsets in their detected centroids. In such cases, the offsets were not found to be oriented in any particular direction, suggesting that they may be caused by the geometrical

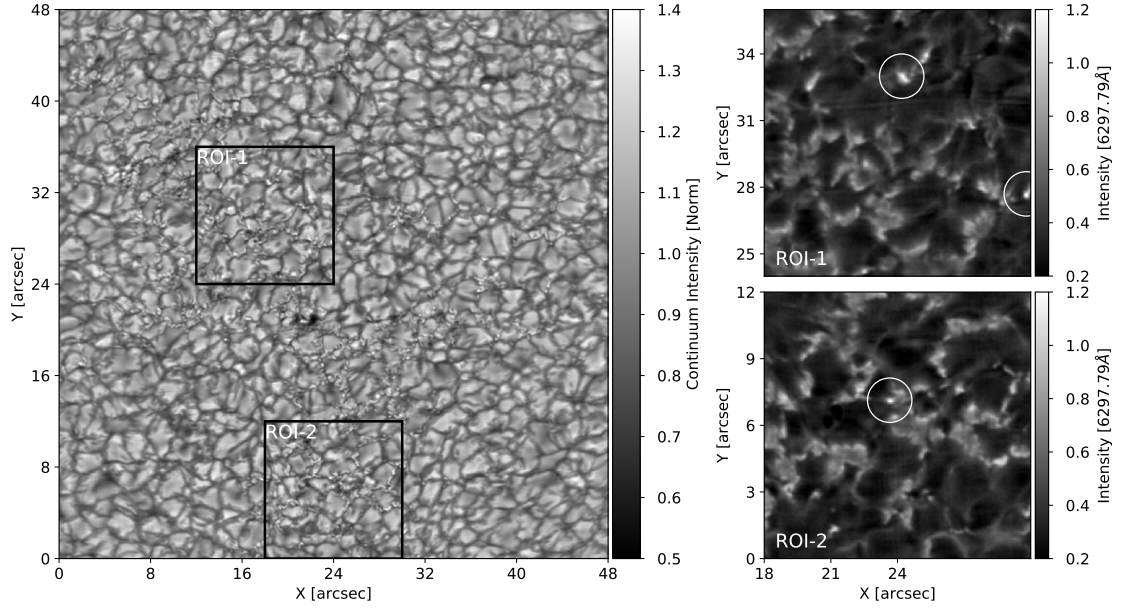


Figure 4.1: Images showing the faculae in the FOV. *Left*: Continuum image from the spectra averaged over wavelengths near 6294.5\AA . The rectangular boxes highlight regions of interest containing a number of bright points. The grey scale values denote intensity normalized to the mean over the FOV. *Right*: Magnified regions of interest as they appear in the core of the Fe I 6297.79\AA spectral line. A few select bright points have been encircled in white.

expansion of the field in combination with the different sensitivities of the spectral lines to the magnetic field. On the other hand, they may also imply heating effects that may be local to certain optical depths as the spectral lines are formed at different regions in the atmosphere. In order to enable the comparison of the atmospheres between different features in the FOV, the pixels were classified into two categories.

We define the 'core' of the plage to be the set of pixels with $B_{los} < -1000G$ at $\log(\tau) = 0.0$, and the 'flank' to be those with $-1000G < B_{los} < -400G$ at the same optical depth. The nodes at the top and middle are unsuitable for such a definition as the magnetic fields expand with height, and since the observations are not at disk center ($\mu = 0.93$), a classification based on the upper atmospheric layers is likely to include pixels which constitute the periphery of the flux elements at the photosphere (the magnetic fields may bend into the line-of-sight and therefore appear stronger). Following this, we observed several patches of weaker positive polarity fields in the immediate vicinity of the facular magnetic elements. In order to ensure that false positives (due to the errors intrinsic to inversions) are excluded in their classification, we systematically filtered out the potentially dubious pixels using the following method; In the first step, all the pixels that had a B_{los} within $\mu[B_{LOS}]_{qs} + 6\sigma[B_{LOS}]_{qs}$ were excluded, where $\mu[B_{LOS}]_{qs}$ and $\sigma[B_{LOS}]_{qs}$ corresponded to the mean and the standard deviation of B_{LOS} in a quiet Sun region, respectively. We then applied an area threshold to the resultant binary map (minimum of 7 pixels at $\log(\tau) = 0.0$). Finally, for each feature (set of connected pixels) in the binary map, the Stokes V amplitudes of the Fe I line pair at 6302.0\AA were averaged over the rel-

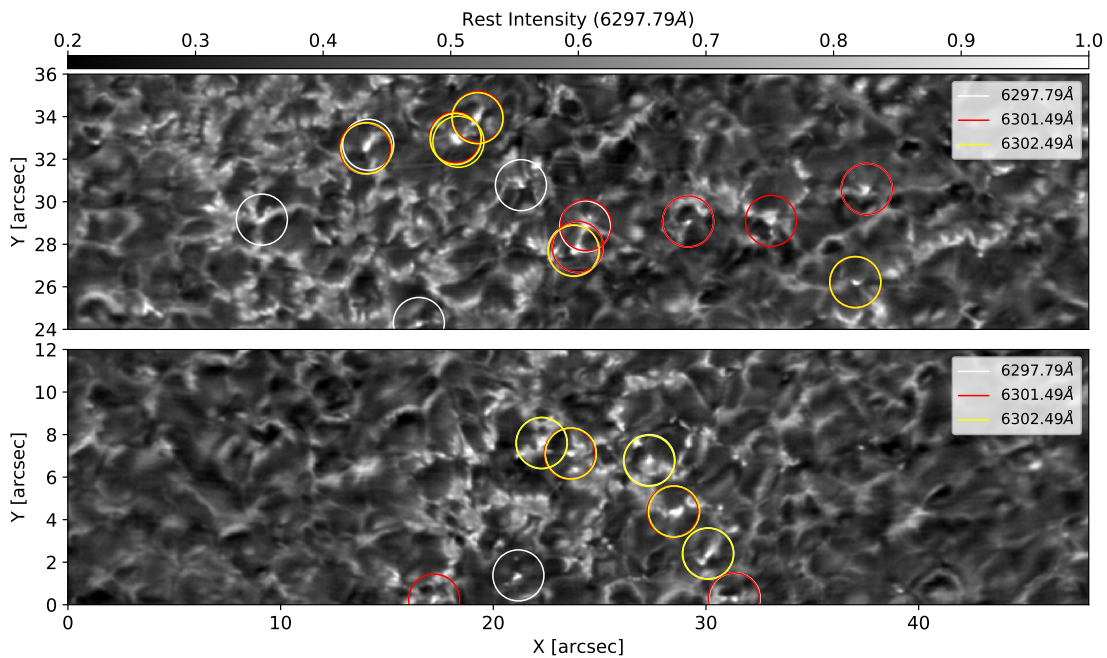


Figure 4.2: **Top:** Blowup of the FOV as seen in the core of the Fe I 6297.79 Å spectral line. The bright points have been identified using the core images in the three strongest spectral lines - white (Fe I 6297.79 Å), red (Fe I 6301.49 Å), and yellow (Fe I 6302.49 Å).

evant pixels, and an amplitude threshold was imposed on the averaged Stokes V profiles. This last step was found to be especially robust in ensuring that the selected pixels had non-zero positive polarity fields associated with them. The floor of our detection limit for B_{los} at $\log(\tau) = 0.0$ was found to be ~ 100 G for the positive polarity fields.

4.4.1 Temperature

The maps of the inverted temperatures corresponding to **ROI-1** (Fig.4.3) have been displayed in the top row of Fig. 4.3. From left to right, they correspond to the three optical depth nodes at $\log(\tau) = 0.0, -1.0, -2.4$, as labelled in the respective panels. The color-scales have been saturated to improve the contrasts of the temperature structure, and therefore do not represent the maximum or minimum values within the FOV.

At the solar surface ($\log(\tau) = 0.0$), the temperature maps reveal the familiar granulation pattern in the regions adjacent to the magnetic flux distribution. The granules in the quiet regions are significantly larger than those adjacent to or interspersed within the dominant flux distribution due to the suppression of convection by the strong magnetic fields of the faculae. Confirmations of this effect have been made earlier in continuum images by Title et al. (1992) in observations taken with a spatial resolution of $1''$, as well as in similar inverted maps by Narayan and Scharmer (2010) taken with a spatial resolution of $0.1''$. The average temperatures in the strong-field regions of the faculae are found to be comparable to those of the inter-granular lanes, and cooler than the average quiet Sun by approximately 100 K. The faculae correspondingly do not show an appreciable difference in their intensity contrasts, as is verified in the continuum image

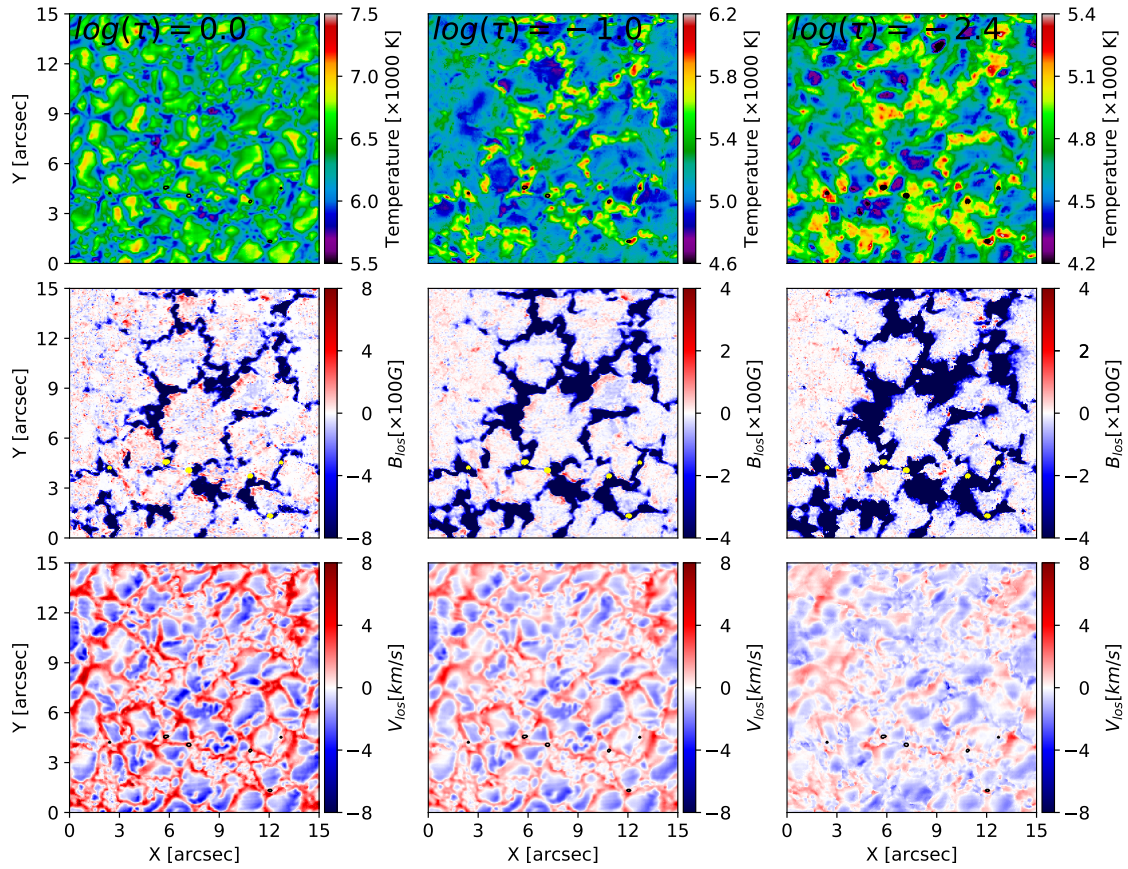


Figure 4.3: Row: Inverted maps of the temperature (top), line-of-sight magnetic field (middle), and line-of-sight velocity (bottom). Column: Optical depth node of the corresponding maps - $\log(\tau) = 0.0$ (left), $\log(\tau) = -1.0$ (middle), $\log(\tau) = -2.4$ (right). The black and yellow contours in the maps denote the location of bright points, and the color scale for B_{los} has been saturated to highlight the adjacent positive polarities.

shown in the left panel of Fig. 4.1. At the middle and upper nodes, however, the temperature difference between the strong-field regions (plage core) and the quiet Sun are better visible in the histograms plotted in Fig.4.4, where the average values of the respective color-coded features are mentioned in all the panels. Further, the locations of the bright points have been highlighted by black contours in the temperature maps. These pixels were identified by applying an intensity threshold to the core-images (image obtained at the line core) of the three strongest spectral lines in the data - Fe I 6297.79Å, Fe I 6301.49Å, and Fe I 6302.49Å. The bright points were found to be preferably situated at the edges of the large-scale flux distribution, and appreciably hotter than the strong-field regions by approximately 500 K. However, owing to their lack of a definite positive contrast (Fig. 4.1), they are harder to identify in the continuum images. In the middle and upper nodes at $\log(\tau) = -1.0, -2.4$, the reduced stratification of the temperature in the magnetized atmospheres of the faculae is easily visible, as is the well-known reverse granulation pattern. In this layer, the temperature in the strong-field regions are hotter than the quiet Sun (≈ 400 K). Such temperature enhancements are observed to be larger

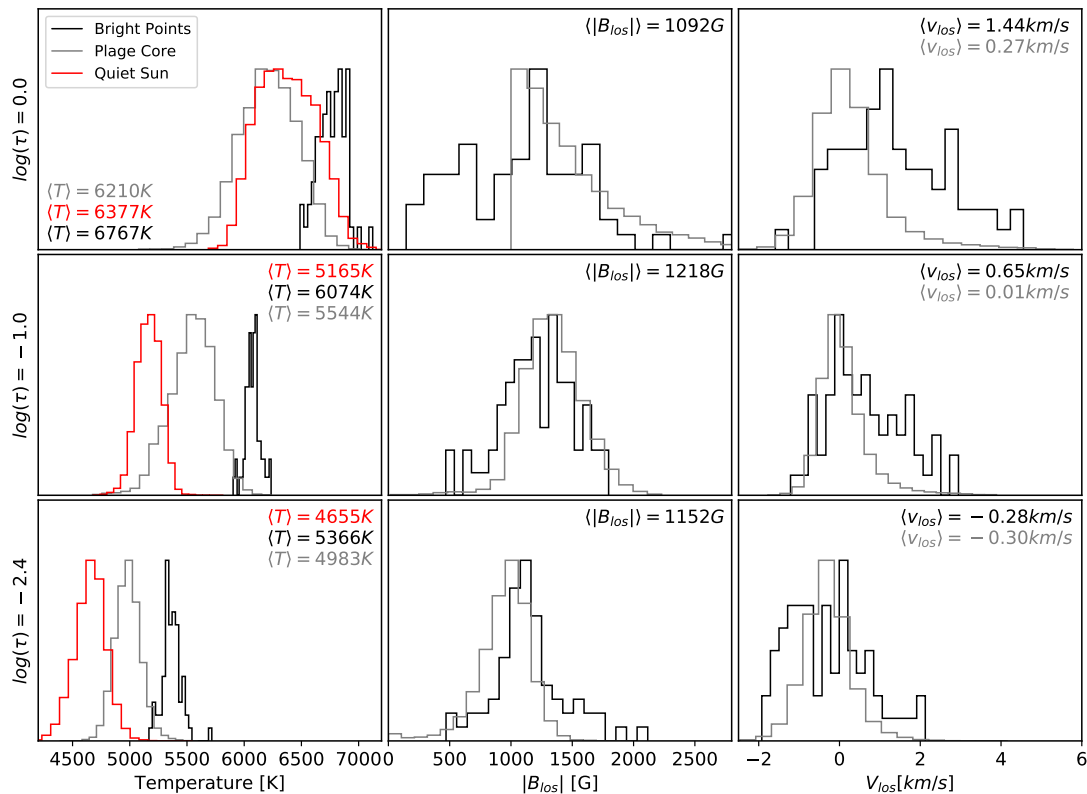


Figure 4.4: Histograms of the physical parameters in the core pixels of the plage (gray), bright points (black), and the quiet Sun (red) at the three optical depth nodes $\log(\tau = 0.0)$ (top), $\log(\tau = -1.0)$ (middle), $\log(\tau = -2.4)$ (bottom). *Left to right*: Temperature, line-of-sight magnetic field, and the line-of-sight velocity.

for smaller-scale magnetic structures, an effect particularly visible in the map at the upper node ($\log(\tau) = -2.4$). Similar to the photosphere, the temperatures at the locations of the facular bright points are observed to be significantly hotter than the strong-field regions in the middle and upper nodes, exceeding them by $\approx 400 K$ and $300 K$ at $\log(\tau) = -1.0$, and $\log(\tau) = -2.4$, respectively (Fig.4.4). Although the bright points are hotter, their excess temperatures compared to the faculae were found to be largely constant with height, indicating an atmosphere with a similar thermal stratification. The average temperature of the facular bright points at the middle and upper nodes were found to be $6074 K$ and $5366 K$, respectively, while the spread in temperature ($\approx 400 K$) was found to be largely uniform across the the three nodes (Fig. 4.4).

In relation to the magnetic flux distribution, the bright points are also seen to be co-spatial with the edges of the magnetic flux concentrations and possess a non-uniform spatial structure. These properties were also reported in some of the facular magnetic elements by Buehler et al. (2015) who performed spatially coupled inversion of a plage on data that were obtained with the Hinode/SOT (Kosugi et al. 2007, Tsuneta et al. 2008) spacecraft.

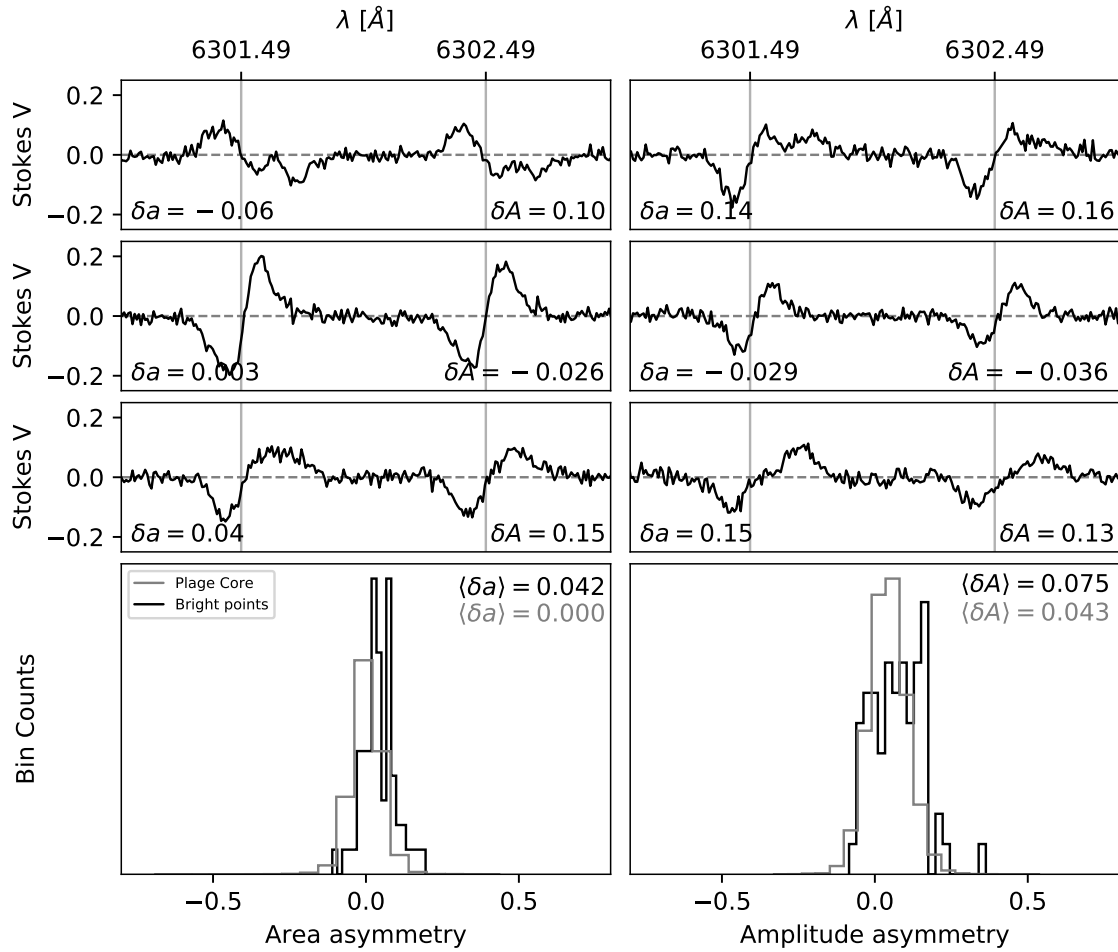


Figure 4.5: Stokes V profiles of select facular bright points found in the FOV. In the bottom row, histograms of the area asymmetry (left) and amplitude asymmetry (right) have been contrasted for the strong-field regions and facular bright points. The asymmetries (relative) were calculated from the red and blue lobes of the respective Stokes V profiles (see for e.g. Martínez Pillet et al. 1997)

4.4.2 Magnetic fields

The maps of the inverted line-of-sight magnetic fields are displayed in the middle row of Fig. 4.3. The color-scales have been saturated to highlight the presence of opposite polarity fields in the vicinity of the dominant flux distribution, and the locations of the bright points are highlighted by yellow contours. In the photospheric layer, several opposite polarity fields (colored red) were found to exist adjacent to the dominant flux distribution in the faculae (blue). The procedure undertaken to verify that the atmospheres in these pixels are not artifacts of the inversion was outlined in the previous section. We, therefore, consider these regions to substantiate the existence of actual magnetic fields of opposite polarity, first seen by Buehler et al. (2015). In accordance with the scenario mentioned in the introduction, these patches of opposite polarities may be caused the action of overturning convection which drags the field lines of the dominant polarity into the downflow lanes. At the photospheric layer, this would cause the field lines at the interface of the

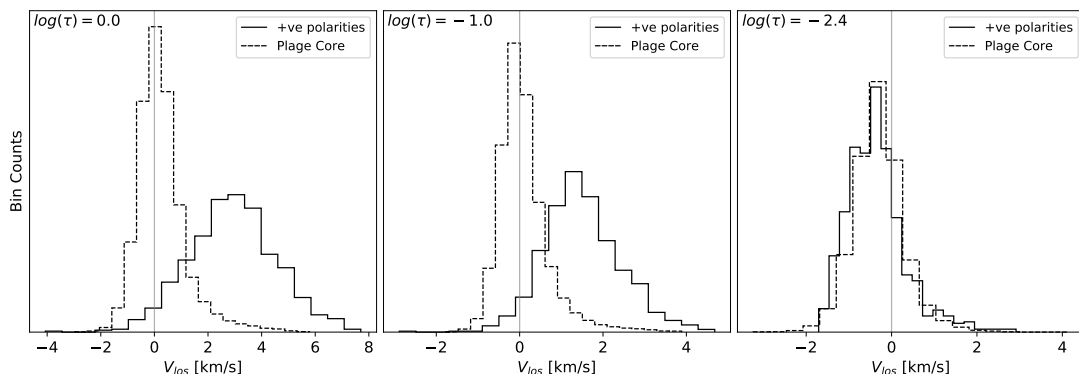


Figure 4.6: Normalized histograms of line-of-sight velocities comparing pixels in the core of the plage with positive

flux distribution and the surrounding inter-granular lanes to become extremely curved, preventing them from being detected by the inversions at the upper nodes due to the rapid expansion of the dominant polarity field with height i.e. the expansion of the magnetic fields of the faculae with height quickly leads to the formation of a canopy above the opposite polarity patches.

At the photospheric layer, consistent with the findings from several studies made with spectropolarimeters, the flux distribution of the faculae is found to take on a filamentary and fractal appearance. Histograms of the line-of-sight magnetic field component reveal the presence of a number of strong kilo-Gauss fields in the cores of the faculae (Fig. 4.4), although it is difficult to compute an average field strength value due to the thresholding applied in selecting the core pixels (note that these are lower limits for the field strength, since only a single, although dominant, magnetic component is considered). Nonetheless, this is in agreement with the numerous studies (see Chapter 1) that have confirmed the existence of kilo-Gauss fields in the solar atmosphere. Further, the histograms of the field strength in the middle and upper layers of the solar atmosphere indicate a small decrease in the mean line-of-sight field strength, suggesting that the magnetic fields in the cores of the faculae are largely vertical with respect to the solar surface. This decrease with height is also exhibited by the bright points, which are also seen to harbour a slightly lesser average line-of-sight field strength compared to the strong-field regions, particularly in the lower and middle node. This appears to be consistent with their peripheral location with respect to the dominant flux distribution.

4.4.3 Line-of-sight velocities

The panels in the bottom row of Fig. 4.3 show the inverted maps of the line-of-sight velocity corresponding to **ROI-1**. In the quiet field-free regions, the strongest downflows in turbulent convection were found to be $\approx 7 \text{ km/s}$ (approximately the speed of sound), and strongest upflows $\approx 6 \text{ km/s}$. In the strong-field regions of the faculae, the line-of-sight velocity maps mirror the maps of temperature in indicating the presence of abnormal granulation at the photospheric layer. Similar to the temperature maps, the locations of the facular bright points are highlighted by black contours. Many of these bright points are

found to occur at the interface between the large-scale flux distribution of the faculae and the inter-granular lanes. This suggests that the origin and evolution of facular bright points are crucially driven by the interaction of the faculae with the surrounding granulation. Further, flows of up to $\approx 8 \text{ km/s}$ were detected in the downflows adjacent to the faculae in the photosphere. Evidence of such supersonic downflows have been reported earlier by Buehler et al. (2015). Within the core pixels of the faculae, however, the average line-of-sight velocity was found to be 0.27 km/s , where the calibration for the absolute line-of-sight velocity was performed by setting the mean v_{los} over a quiet Sun region in the FOV to zero at the photosphere.

Comparisons of the histograms of the line-of-sight velocity (v_{los}) of the strong-field regions (plage cores) and the bright points (Fig.4.4, right column) indicate the presence of stronger downflows in the latter, with $\langle v_{los} \rangle = 1.44 \text{ km/s}$ and $\langle v_{los} \rangle = 0.65 \text{ km/s}$ at $\log(\tau) = 0.0$ and $\log(\tau) = -1.0$, respectively. The distribution of their v_{los} histogram is also observed to be moderately asymmetric, with maximum velocities in the bright points reaching $\approx 4 \text{ km/s}$ and $\approx 3 \text{ km/s}$ at $\log(\tau) = 0.0$ and $\log(\tau) = -1.0$, respectively. This again appears to be due to the fact that several pixels in bright points are co-spatial with the inter-granular lanes bordering the magnetic flux distribution. On the contrary, the line-of-sight velocities in the strong-field regions are found to be much lesser on average (see Chapter 1). At the upper node, both bright points and the core pixels are found to be equally associated with upflows and downflows, with an average upflow of only $\langle v_{los} \rangle \approx 0.30 \text{ km/s}$. This is difficult to interpret directly from the histograms, and we reserve our conclusions for the next chapter where the line-of-sight velocities of bright points are studied using numerical simulations.

The top three rows of Fig. 4.5 show examples of the Stokes V profiles found in facular bright points. It is seen that several of these profiles exhibit strong area and amplitude asymmetries (relative), which can be defined and calculated for the corresponding profiles according to (Grossmann-Doerth et al. 1989, Martínez Pillet et al. 1997):

$$\delta a = \frac{a_b - a_r}{a_b + a_r},$$

$$\delta A = \frac{A_b - A_r}{A_b + A_r},$$

where a_b and A_b denote the area and amplitude of the blue (r represents red) lobe of the Stokes V profiles, respectively. These relative asymmetries indicate the presence of gradients in the line-of-sight velocity as well as the magnetic field strength (Solanki and Pahlke 1988, Solanki 1993), histograms of which have been plotted in the bottom row of Fig. 4.5. Both the computed average amplitude ($\langle \delta A \rangle = 0.075$) and area ($\langle \delta a \rangle = 0.042$) asymmetries in facular bright points are larger than that of the cores, indicating stronger accelerating downflows, consistent with the values of $\langle v_{los} \rangle$ reported in Fig.4.4. This provides direct confirmation of the Stokes V asymmetry models by Grossmann-Doerth et al. (1988, 1989), Solanki (1989). It also generally agrees with the picture obtained from Sunrise/IMaX data (Solanki et al. 2010, Barthol et al. 2011, Martínez Pillet et al. 2011a,b, Martínez González et al. 2012). Additionally, further indications of the association of overturning convection with opposite polarity patches is found in the histograms

of Fig. 4.6. The line-of-sight velocities in the positive polarity patches are found to be significantly higher than their counterparts in the core of the faculae. Thus, we believe that the spectropolarimetric inversions of our observations substantiate the dragging of the field-lines by overturning convection. However, in order to study the origins of the facular bright points and their dynamic properties, we turn to the MHD simulations of faculae in the next chapter.

5 Numerical simulations of faculae

Due to the diffraction limit of optical systems, the smallest observable magnetic structures ($\approx 100 \text{ km}$) in the solar atmosphere are still resolved by high resolution observations with but limited fidelity. Even with fast cadence, a small-scale magnetic element with a lifetime of 3 *min* decays in time-series observations made with a cadence of 30 *sec* in six time steps. In conventional slit-spectra, the evolution of such structures is altogether absent, so that questions concerning their formation and dynamics cannot be sufficiently addressed for shorter time intervals. In order to further probe the physics governing these structures on smaller spatial scales with higher cadence, the complimentary technique of direct-numerical-simulations (DNS) to simulate solar magnetic structures can also be employed. Moreover, DNS provide a way of circumventing limitations imposed by image degradation and other uncertainties (for example, degeneracies in inversions), making them a useful method of pinning the physics underlying solar phenomena.

Since the pioneering work of Nordlund (1982), several numerical codes such as STAGGER (Stein and Nordlund 1998), MURaM (Vögler et al. 2005a, Rempel 2017), BIFROST (Gudiksen et al. 2011), and CO5BOLD (Freytag et al. 2012) have been used to simulate different solar magnetic structures such as faculae (Vögler and Schüssler 2003, Keller et al. 2004, Carlsson et al. 2004), active region sunspots (Rempel et al. 2009, Cheung et al. 2010, Rempel 2011), quiet Sun magnetic fields (Vögler and Schüssler 2007, Rempel 2014) in the photosphere as well as the chromosphere. Two key objectives of such simulation-based studies have been to reproduce the observed (or inferred) properties of solar magnetic elements in simulated structures, as well as to probe the physical processes participating in their evolution on scales inaccessible to observations. For example, Carlsson et al. (2004) used 3D radiative-MHD simulations of photospheric faculae within a $6 \times 6 \text{ Mm}^2$ computational domain, extending from the temperature minimum region to a depth of 2.5 *Mm* below the solar surface. The spatial resolutions (grid-spacing) chosen for the simulation were 25 *km* in the horizontal direction, and varied from 15 – 35 *km* in the vertical direction (height). Initially, a uniform magnetic field of $\langle B \rangle = 250 \text{ Gauss}$ was introduced in the simulation box following which the system was allowed to relax to a statistically stationary state. Their simulation qualitatively reproduced some important observed properties of faculae - the expulsion of flux (Parker 1963) from the center of granules, their concentration in inter-granular lanes, the intensification of field strengths to kilo-Gauss values, confirmation of the hot-wall effect (Spruit 1976), and the center-to-limb variation of the facular intensities. The realism of their simulation was further evident when they reported that the difference between the synthetic spectra of 1838 G-band spectral lines and the Jungfrauoch atlas (Delbouille et al. 1973b) was not more than 8% rms. In an another complimentary study, De Pontieu et al. (2006) compared

the photometric properties of limb-faculae ($\mu = 0.65$) observed in the data collected at the Swedish Solar Telescope (SST, Scharmer et al. (2003a)) with the simulation runs of Carlsson et al. (2004). The focus of their study, however, was to investigate the temporal evolution of facular elements. Over a period of several minutes, the facular structures, both in their observations and simulations, were observed to rapidly change their morphological properties on timescales corresponding to the solar granulation. They argued that the variability in the photometric properties of limb-faculae is, therefore, chiefly driven by solar granulation.

In addition to comparing images, studies comparing the synthetic Stokes profiles generated from simulated atmospheres with spectropolarimetric observations have also been pursued. For example, Khomenko et al. (2005) used the 3D radiative-MHD MURaM (Vögler and Schüssler 2003, Vögler et al. 2005a) code to simulate mixed-polarity faculae spanning a $6 \times 6 Mm^2$ FOV, with a lateral spatial resolution of 20 km. The simulations were run with different values for the initial uniform magnetic field ($\langle B \rangle = 140, 30, 10$ Gauss). In their study, they synthesized the Stokes I and V profiles of the Fe I 6301.5Å, Fe I 6302.5Å, Fe I 15648Å, Fe I 15652Å spectral lines, comparing them with the observed line profiles in the Liège atlas (Delbouille et al. 1989). They reported both agreements and discrepancies in their comparison. For example, the Stokes I profiles were found to match the observed profiles in the atlas well, the amplitude and area asymmetries of the Stokes V profiles degraded to 1'' were found to match those of the network and inter-network regions, and the average area and amplitude asymmetries of the Stokes V profiles at 1'' resolution was found to be positive in granules and close to zero / negative in the inter-granular lanes. Some of the discrepancies they reported included a larger number of irregular Stokes V profiles compared to observations, as well as zero-crossing wavelengths of Stokes V, in the quiet Sun, that were too redshifted.

Such comparative studies between simulations and observations are an effective way of diagnosing potential issues in models of radiation-matter interactions (see Stein 2012, Leenaarts 2020, for a review). Moreover, simulations also facilitate the study of physical processes that are difficult to detect without extremely good seeing conditions (for ground-based telescopes) and sophisticated image-restoration techniques. In the previous chapter, spectropolarimetric observations and their inversions were used to identify and study the stratification of physical parameters in facular bright points. In this chapter, we attempt to address some of the questions concerning their origin, and evolution using numerical simulations.

5.1 Numerical code and simulation setup

The MURaM (MPS/University of Chicago Radiative MHD) code (Vögler and Schüssler 2003, Vögler et al. 2005a, Rempel 2017), jointly developed at the Max Planck Institut für Sonnensystemforschung in Katlenburg-Lindau and the University of Chicago, is a radiative MHD code that simulates magneto-convection in the Sun. The computational domain in MURaM simulations typically includes regions of the convection zone below the solar surface, extending to the upper layers of the lower solar atmosphere (and in

some cases into the corona). The primary physical parameters of the plasma - density (ρ), temperature (T), total energy density (e), velocity (\mathbf{v}), and the magnetic field (\mathbf{B}) - are self-consistently obtained from the MHD equations at every time step on a 3D cartesian equidistant grid of cells. The set of equations include the continuity equation:

$$\frac{\partial \rho}{\partial t} + \nabla \cdot (\rho \mathbf{v}) = 0, \quad (5.1)$$

the momentum equation:

$$\frac{\partial \rho \mathbf{v}}{\partial t} + \nabla \cdot \left[\rho \mathbf{v} \mathbf{v} + \left(p + \frac{|\mathbf{B}|^2}{8\pi} \right) \mathbf{1} - \frac{\mathbf{B}\mathbf{B}}{4\pi} \right] = \rho \mathbf{g} + \nabla \cdot \underline{\tau}, \quad (5.2)$$

where p is the gas pressure; $\mathbf{1}$ is the 3×3 unity matrix, and $\underline{\tau}$ is the viscous stress tensor; the induction equation for the magnetic field:

$$\frac{\partial \mathbf{B}}{\partial t} + \nabla \cdot (\mathbf{u}\mathbf{B} - \mathbf{B}\mathbf{u}) = -\nabla \times (\eta \nabla \times \mathbf{B}), \quad (5.3)$$

and the equation for the total energy density (e):

$$\frac{\partial e}{\partial t} + \nabla \cdot \left[\mathbf{v} \left(e + p + \frac{|\mathbf{B}|^2}{8\pi} \right) - \frac{1}{4\pi} \mathbf{B}(\mathbf{v} \cdot \mathbf{B}) \right] = \frac{1}{4\pi} \nabla \cdot (\mathbf{B} \times (\eta \nabla \times \mathbf{B})) + \nabla \cdot (\mathbf{v} \cdot \underline{\tau}) + \nabla \cdot (K \nabla T) + \rho(\mathbf{g} \cdot \mathbf{v}) + Q_{rad}, \quad (5.4)$$

where $\eta = c^2/4\pi\sigma$ is the magnetic diffusivity, c is the speed of light, σ is the electrical conductivity, and K is the thermal conductivity. Further, the MURaM code also accounts for the transport of energy through radiation - the term Q_{rad} , representing radiative heating and cooling rates, is computed as the divergence of the radiative energy flux \mathbf{F}_ν integrated over frequency:

$$Q_{rad} = - \int_\nu (\nabla \cdot \mathbf{F}_\nu) d\nu = 4\pi\rho \int_\nu \kappa_\nu (J_\nu - S_\nu) d\nu, \quad (5.5)$$

$$\mathbf{F}_\nu = \int_{4\pi} I_\nu(\mu) \mu d\Omega, \quad (5.6)$$

$$J_\nu = \frac{1}{4\pi} \int_{4\pi} I_\nu(\mu) d\Omega, \quad (5.7)$$

where \mathbf{F}_ν is the radiative energy flux, J_ν is the solid-angle averaged specific intensity, and the source function S_ν is taken as the planck function (B_ν) in magneto-convective simulations of the photosphere. In the computation of Q_{rad} and \mathbf{F}_ν , the integration over the frequency is done approximately by dividing the electromagnetic spectrum into frequency bins (non-gray) and using their respective bin-averaged opacities. For the integration over the solid angle in Eq 6.6 and Eq 6.7, the specific intensities are obtained by solving the radiative transfer equation along 24 ray directions spanning 4π steradian in order to account for three-dimensional radiative transport of energy. Lastly, the system of MHD equations listed above are closed with an equation of state (EOS) that accounts for the effects of partial ionization of the 11 most abundant elements.

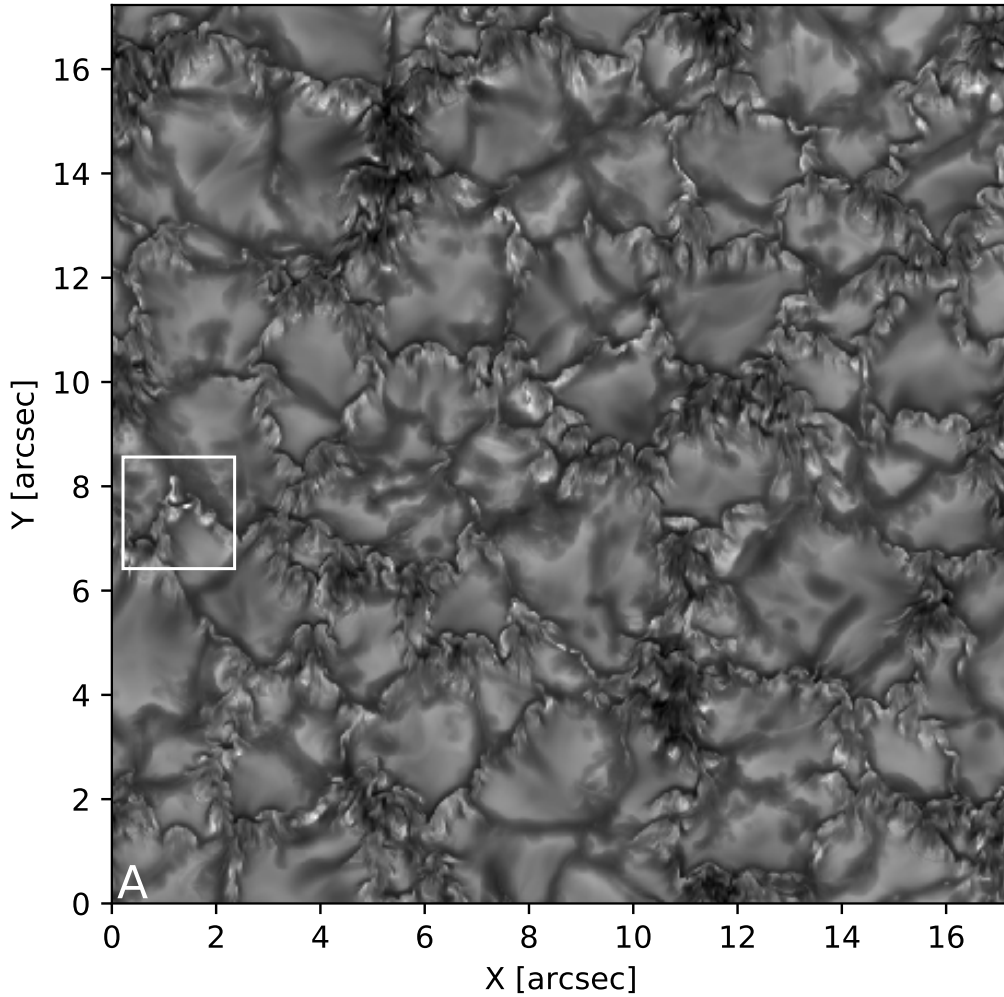


Figure 5.1: Continuum image synthesised from a snapshot of 3D radiative-MHD MURaM simulations. The white box provide a reference for the scale of the FOV for which high-cadence (2 s) simulations of a facular bright point have been used in the following sections.

For the simulation runs used in this thesis, an open lower boundary was adopted i.e. plasma is allowed to freely enter and exit the computational domain. The pressure, however, is assumed to be uniform and is continuously adjusted to conserve the mass of the plasma within the computational domain, and the magnetic field at the lower boundary is assumed to be strictly vertical at all time steps. At the upper boundary, the outflows were allowed to leave the computational domain (open) while the magnetic field configuration was assumed to be potential (force-free). The latter assumption is taken to hold good as the plasma-beta ($\beta \propto P_{gas}/B^2$) at the top of the box (1.5 Mm above the solar surface) is much less than unity, and the field becomes increasingly force-free with height. Similarly, an open lower boundary - allowing plasma to enter and exit the computational domain - was adopted. Along with the imposition of periodicity at the sides of the computational domain, this leads to the conservation of magnetic flux at all heights and at every time step ($\nabla \cdot \mathbf{B} = 0$). The physical dimensions of the computational domain are $12.5 \times 12.5 Mm^2$

(horizontal), extending from 1.5 Mm above the solar surface to a depth of 2.5 Mm below the surface. The grid size of the domain was chosen to be $1024 \times 1024 \times 512$ - corresponding to a resolution of 12.20 km in the horizontal direction and 7.8 km in the vertical direction. Fig. 5.1 gives a sense of the horizontal size of the box.

Initially in the simulation, convection was allowed to set in and stabilise over a period of eight hours, following which a uniform unipolar vertical magnetic field with $\langle B \rangle = 420$ Gauss was introduced throughout the computational domain. The simulation was then run for two hours to allow magneto-convection to reach a quasi-stationary state, followed by another six hours over which several bright points were identified in images ($\mu = 1.0, 0.93$) synthesized with the forward synthesis module of the SPINOR-LTE (Frutiger et al. 2000a) code. For this step involving the identification of bright points, images were synthesised from the snapshots for every ≈ 2 *min* of solar time. Further, the synthesised images were degraded to the spatial resolution of observations to test the visibility of the identified bright points. Subsequently, their evolution was then studied with an approximate cadence of 2 *sec*, in the line-core of the Fe I 6297.79Å spectral line - one of the lines chosen for the study of bright points with spectropolarimetric inversions in the previous chapter. The atomic parameters of the spectral line used during the synthesis were identical to those used in the inversions.

In Fig. 5.2 we display a continuum image of the simulated domain sufficiently after the magnetic field was inserted, so that it correspond to a statistically steady phase. By this time the magnetic field is concentrated in the intergranular lanes, very similar to the situation seen in the observations. In this thesis, we focus on discussing the properties and evolution of a single bright point studied with high-cadence, appearing in the region enclosed by the white box. A discussion on other simulated bright points and their statistical properties is reserved for a follow-up paper.

5.2 Simulation results

5.2.1 Photometric properties of simulated facular bright points

Fig. 5.2 and Fig. 5.3 display a time-series of synthetic images at full grid resolution in the continuum, and in the core of the Fe I 6297.79Å spectral line, respectively. For the purposes of motivating a discussion on the morphological properties of bright points, the images have been cropped from the full FOV of the MHD simulations with the dimensions indicated by their respective axes. In the panels shown, a bright point (highlighted by red contours) is observed to spontaneously appear and disappear at the vertex of three granules within a span of approximately 2 *min*. The pixels constituting the bright point were identified by applying an intensity threshold to the line-core images - similar to the procedure followed in the previous chapter - as well as an area threshold. The values of the intensity and area thresholds were chosen so as to strike a balance between capturing the bright point for the longest contiguous time interval and preventing disjoint pixels in the FOV from being included. In the initial stages of evolution from time $t = 47s$, the bright point can be seen reaching maximum intensity at time $t = 77s$ with a size of approximately $0.25'' \times 3''$. While this is theoretically resolvable by 1m-class telescopes, studying such structures in ground-based observations would likely be still difficult with-

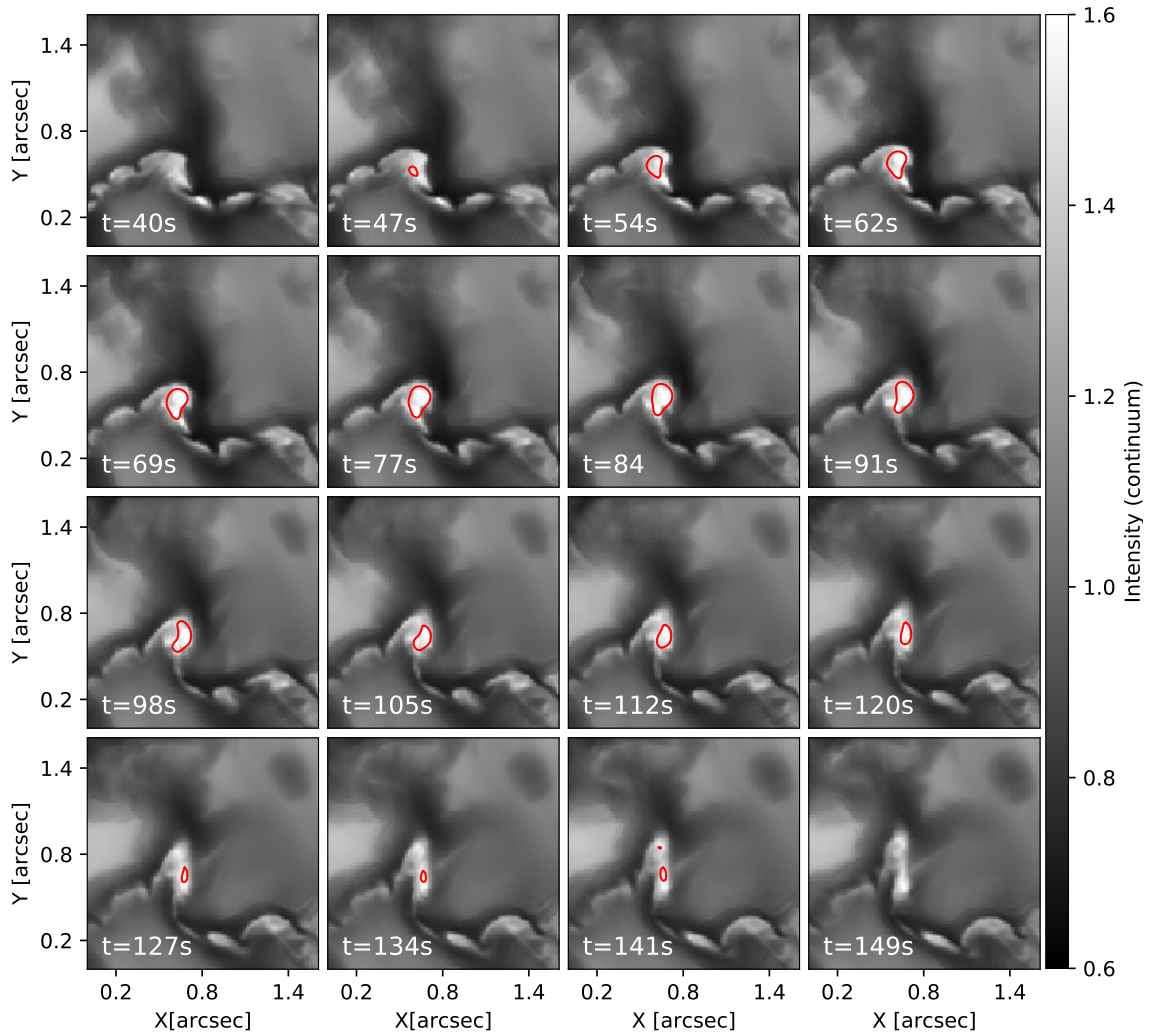


Figure 5.2: Continuum images showing the evolution of a bright point with time at full resolution, with identical grey scales.

out excellent seeing conditions and sophisticated image restoration techniques. Throughout its lifetime, brightness of the structure is also seen to be co-spatial with the magnetic flux patch occupying the inter-granular lane. The morphology of the brightness evolves, especially rapidly during the decay phase from time $t = 120s$, changing from a nearly elliptical structure to a thin sheet, elongated along the y -direction and compressed along the x -direction by the surrounding convection.

Further evidence of the temporal variability of the spectral properties of the bright point is found in Fig. 5.4. Defining the centroid of the bright point to be the pixel with maximum brightness at any given time in a smoothed line-core image, the normalized Stokes I (solid) line-profiles at the centroid have been plotted for the corresponding time steps in Fig. 5.4. Also plotted are the Stokes V (dash-dotted) line-profiles of the centroids with an artificially added vertical offset of 0.70. The vertical dotted lines in the plots denote the nominal center of the spectral line. The plots of Fig. 5.4 can be used to make a few noteworthy observations. Firstly, during the growth phase of the bright point from

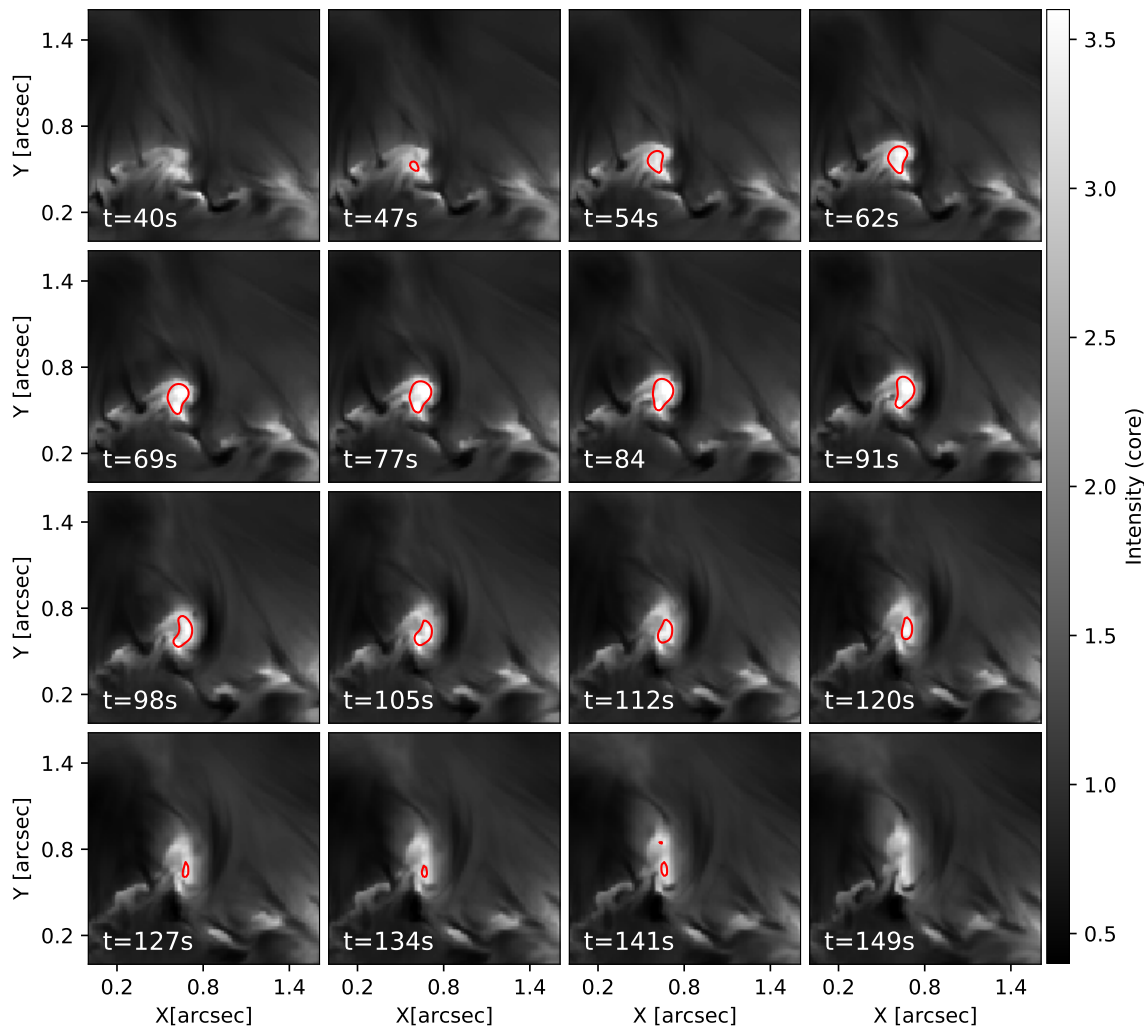


Figure 5.3: Similar to Fig.5.2, but in the line-core of the Fe I 6297.79Å spectral line, normalized with respect to their average over the field of view.

time $t = 47 - 77s$, the line-profiles of both stokes components are simple in character. However, during the decay phase (bottom panels in Fig. 5.4, some of the Stokes I line-profiles are completely split while the Stokes V profiles become irregular and asymmetric. In order to better understand the dynamical properties of the bright point, we now attempt to directly interpret the simulated atmospheres in the next sections.

5.2.2 Atmosphere in simulated facular bright points

To track the bright point as it evolves with time, intensity and area thresholds were first applied to the line-core images smoothed with an appropriate kernel at each time step. The centroid of the bright point was defined as the pixel with the maximum intensity in the smoothed image. In order to obtain the mapping between the geometrical heights and optical depths in the simulated atmospheres, the optical depth mapping module of the inversion code (MAPTAU) was used. This step facilitates a direct comparison of the simulated

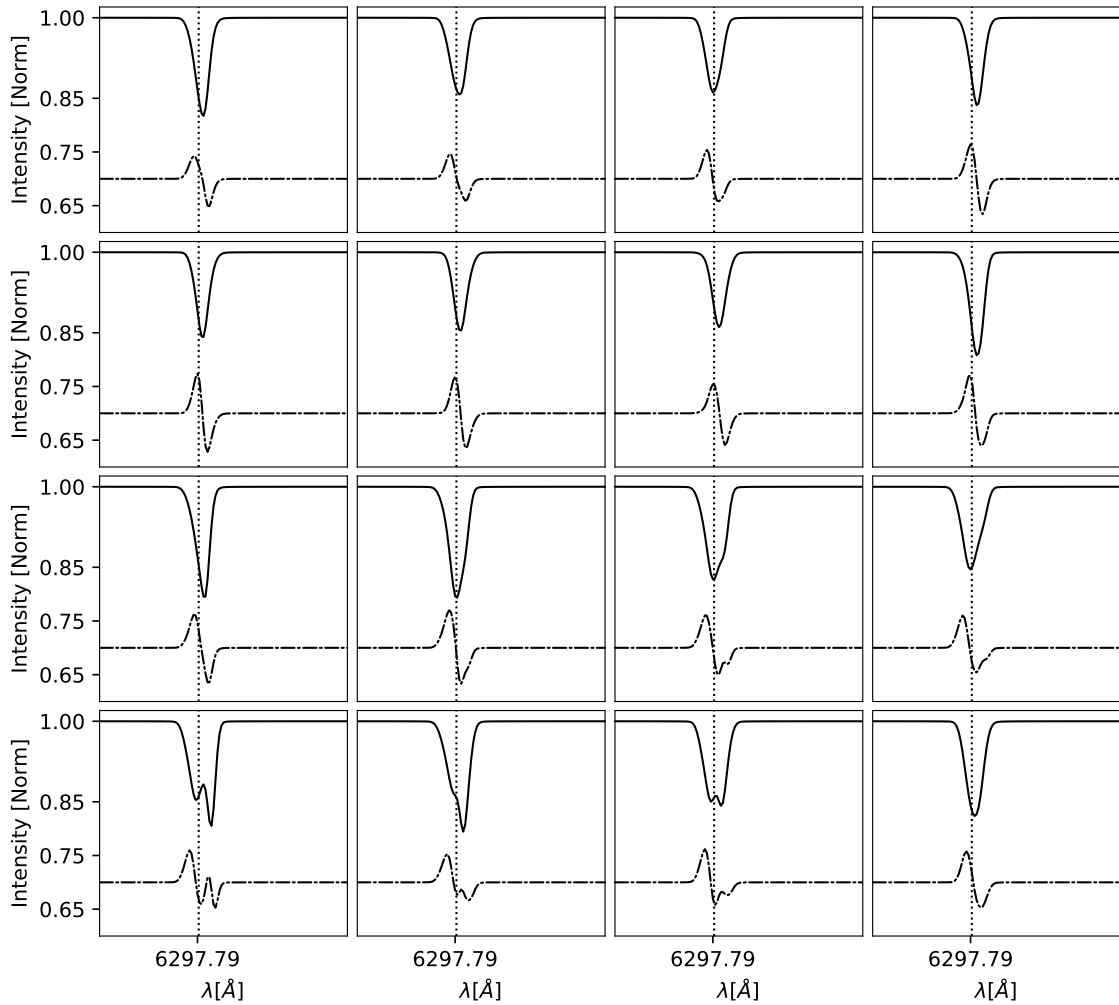


Figure 5.4: Synthetic Stokes I (solid), V (dash-dotted) line-profiles of the Fe I 6297.79Å spectral line, corresponding to the bright point in Fig. 5.2 and Fig. 5.3. Note that the vertical axis labelling refers only to Stokes I.

quantities at the relevant optical depth surfaces with the observations, since the latter are frequently expressed in the optical depth scale. Fig. 5.5 and Fig. 5.6 show vertical cuts of v_{los} and B_{los} taken at the center of the bright point, taken from MHD simulations: $v_{los}(x, z)$ and $v_{los}(y, z)$, $B_{los}(x, z)$ and $B_{los}(y, z)$ - the vector plots in the figures represent the projection of the respective 3D vector fields on the vertical planes. The horizontal lines (solid) in the figures show the position of the $\log(\tau) = 0.0$ layer, only for the pixel highlighted with the red cross-hair, while the vertical lines (solid) denote the x and y co-ordinate of the cross-hair on the respective vertical planes. The vector plots in the bottom row of the figure are identical to the ones shown at the top, but for the line-of-sight magnetic field (B_{los}). The right hand panels in both figures display images in the continuum and the core of the spectral line (Fe I 6297.79Å) for easy identification of the bright points. In Fig. 5.5, the bright point has not yet completely formed and its core intensity begins increasing with time. The magnetic fields in the flux region can be seen to be nearly vertical with respect to the solar surface in the photosphere (Martínez Pillet et al. 1997). They quickly

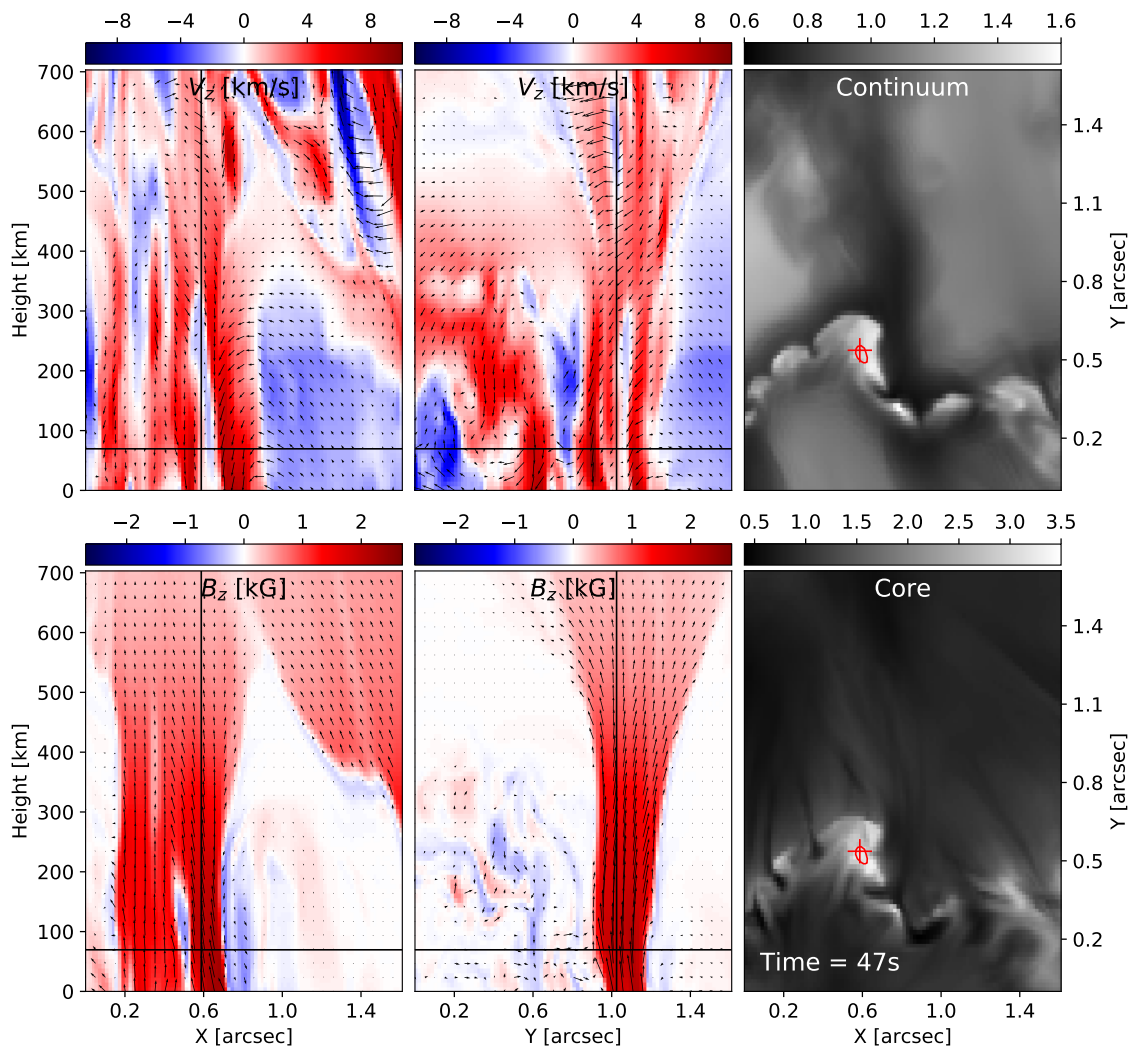


Figure 5.5: Vector plots showing vertical cuts of the line-of-sight velocity and the line-of-sight magnetic field at the centroid pixel indicated by the red cross-hair in the continuum (top right) and line-core (bottom right) images, as a function of two spatial dimensions: $v_{los}(x, z)$ (top left), $v_{los}(y, z)$ (top middle), $B_z(x, z)$ (bottom left), and $B_z(y, z)$ (bottom middle). The arrows represent the projection of the vector quantities in the plotted plane. The horizontal line (solid black) denotes the position of the $\log(\tau) = 0.0$ surface at the centroid pixel, and the vertical line (solid black) denotes the x and y co-ordinates of the cross-hair in the respective vertical planes.

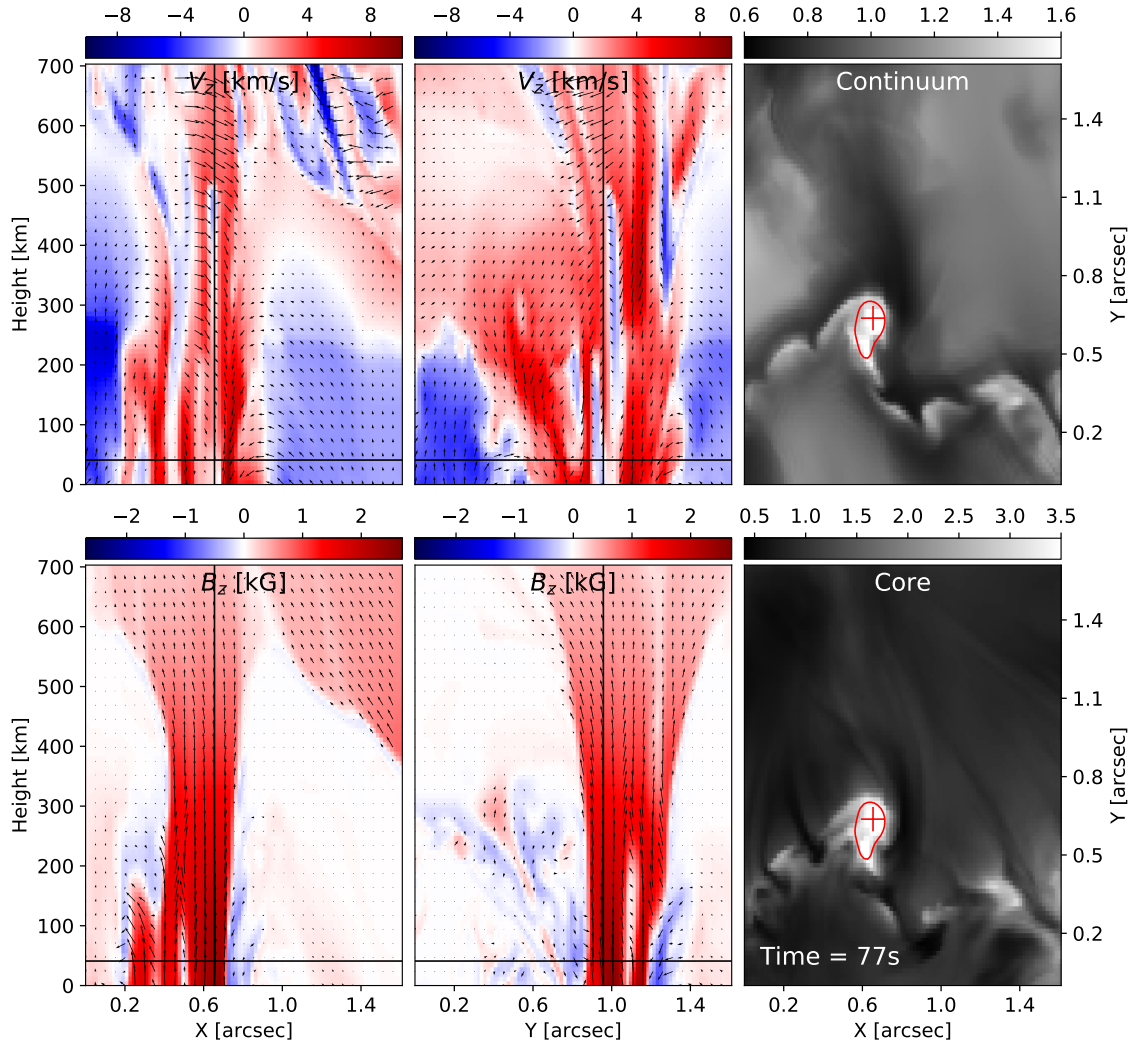


Figure 5.6: Identical to Fig. 5.5, but shown at a later time $t = 53s$

expand above the photosphere to form a canopy at a height of approximately 500 km . Also visible are several opposite polarity fields adjacent to the dominant flux region. As mentioned in the previous chapters, the existence of these opposite polarities is a possible indication of the field-dragging effect of overturning convection, the confirmation of which can be attempted by using field-line tracing techniques.

In the vector plots of v_{los} , the spectropolarimetric color convention was used so that the red and blue regions represent downflows and upflows respectively. While most of the flux region is co-spatial with downflows, a narrow blue elongated (upflow) feature is visible in both the vertical cuts of v_{los} , oriented along the solid vertical line. This feature can also be found in the v_{los} plots of Fig. 5.6, which is another snapshot at a later instant in time. However, the feature seems to have propagated upwards, traversing a distance of approximately 200 km in roughly $30s$, i.e. with a velocity of $6 - 7\text{ km/s}$. The origin of this jet-like structure is unclear, but it appears to be playing a role in the time-evolution of the bright point's intensity. The propagation of mode-converted slow magneto-acoustic

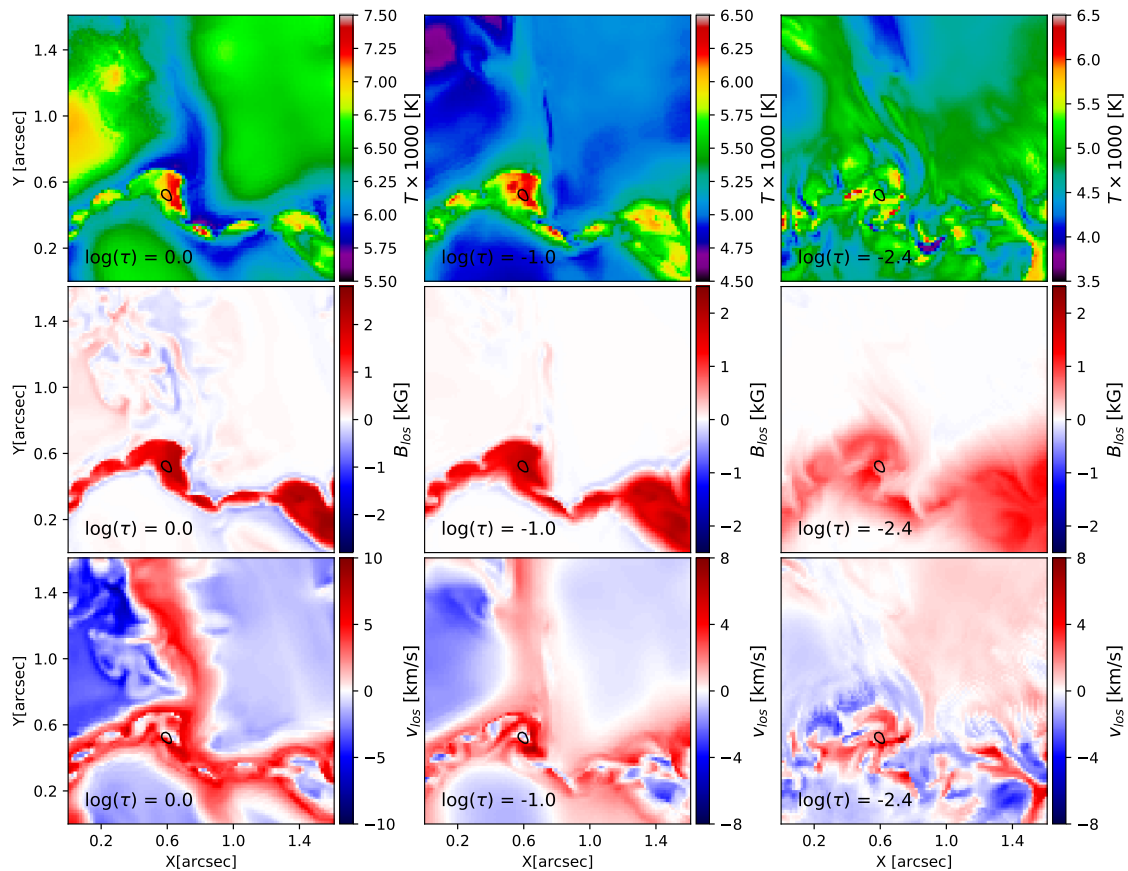


Figure 5.7: Maps of the atmospheric parameters obtained from the MHD simulations: temperature (top), B_{los} (middle), and v_{los} (bottom) at the three optical depth positions: $\log(\tau) = 0.0, -1.0, -2.4$. The atmospheres correspond to the time $t = 47s$.

waves in fluxtubes, excited by the turbulent convection, has been proposed and studied before by several authors (see for e.g. Spruit 1991, Cally and Bogdan 1997, Khomenko et al. 2008). Such oscillations propagating through a fluxtube may develop into shocks at the upper atmospheric layers and dissipate the energy locally (Vecchio et al. 2009). However, the phase speeds of the slow magneto-acoustic waves in the photosphere are $\approx 4 \text{ km/s}$, which appears to be slower than the propagation speed of the jet-like structure in the observed bright point. On the other hand, (Yadav et al. 2020) recently studied vortex flows as a source of chromospheric heating. In this and many other lower resolution simulations, the observed bright points were found to not be associated with significant vorticity, and therefore their role as a mechanism for heating appears to be limited, at least in the photosphere.

5.2.2.1 Temperature of the simulated facular bright points

The top rows of Fig. 5.7, Fig. 5.8, and Fig. 5.9 show maps of the temperature from the MURaM simulations obtained at the optical depths corresponding to the inversions: $\log(\tau) = 0.0, -1.0, -2.4$, from left to right. The three figures, in their order of mention,

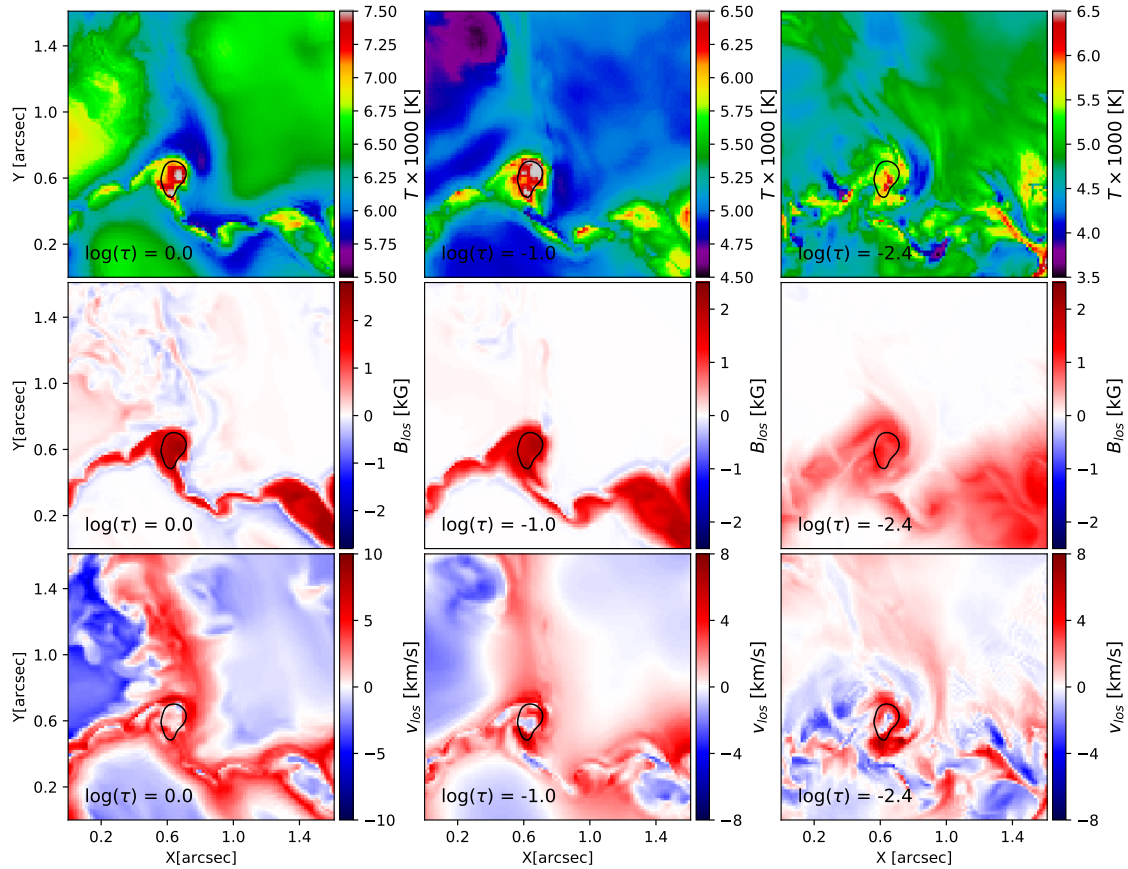


Figure 5.8: Similar to Fig.5.7, obtained at the time step ($t = 77s$) where the intensity of the bright point is maximum.

represent snapshots of the atmosphere at times $t = 47, 77, 149s$ - the beginning, peak, and decay phases of the bright point according to Fig. 5.3 and Fig. 5.2. Mapping of the optical depth to the geometrical height of the MURaM atmospheres was performed using the optical depth mapping module (MAPTAU) of SPINOR (Frutiger et al. 2000a). At time $t = 47s$, the maximum and minimum temperatures within the bright point (black contours) were found to be $7241 K$ and $7070 K$ at the photosphere (Fig. 5.7), respectively, already hotter than the bright points found in our observations. During the growth phase, the temperature difference between the hottest and the coldest pixels within the bright point were observed to steadily increase from $100 K$ to $1312 K$ at time $t = 77s$ (Fig. 5.7). The corresponding maximum and minimum temperatures within the bright point were found to be $8758 K$ and $7445 K$, respectively, at the photospheric layer. As a result of the sharp differences in the rates with which the temperatures in such pixels increased, the bright point at time $t = 77s$ (peak intensity) shows a strong temperature structure in the photosphere and at the middle node. Further, contrary to some of the bright points found in the observations, the simulated bright point does not appear to have an identifiable temperature structure at the top node. Whether this is a general feature of all bright points, or an artifact of the choice of the boundary conditions is not clear at present. However, in order to understand the temperature differential in the bright point, the geometrical separation in height between the two pixels due to corrugations of the $\log(\tau) = 0.0$ surface

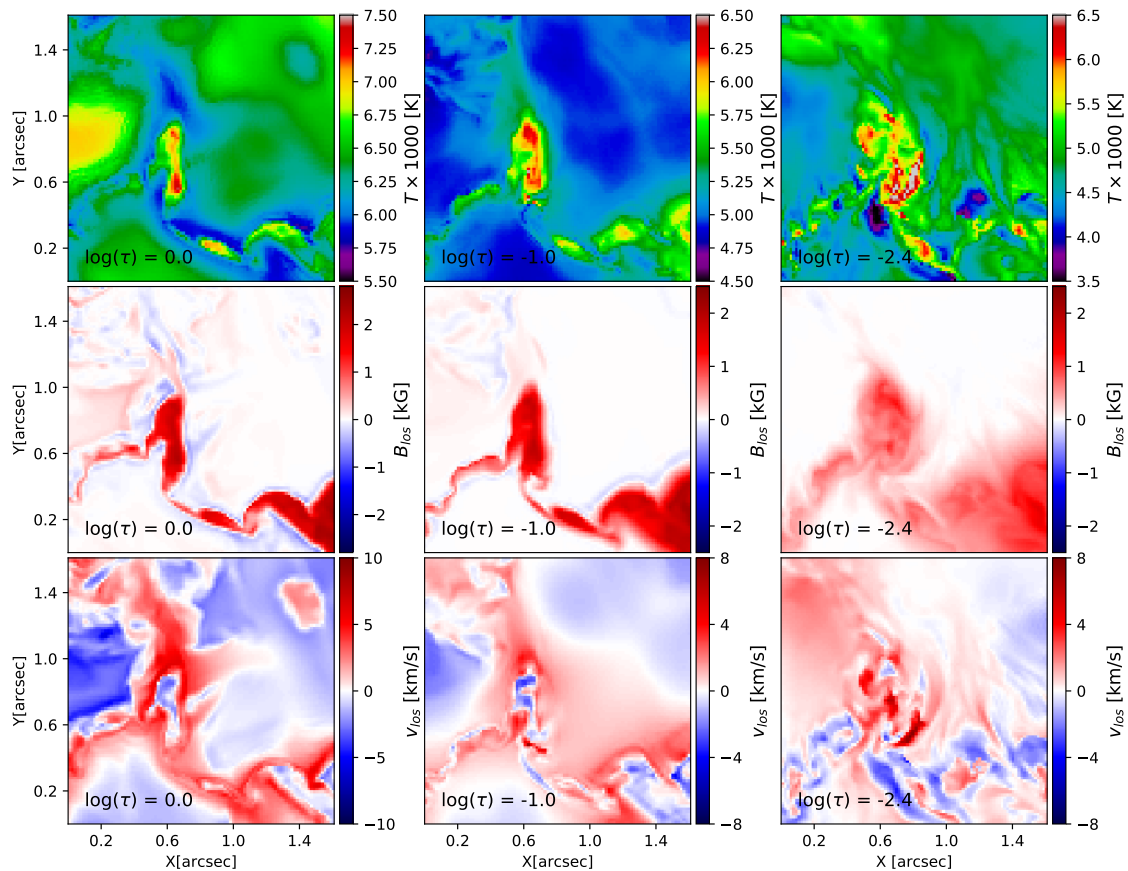


Figure 5.9: Similar to Fig.5.7, obtained at the time step ($t = 149s$) where the bright point has decayed.

must also be taken into account. Subsequently, the height difference between the hottest and coldest pixels was observed to grow from 8 km at $t = 47s$ to approximately 125 km at $t = 77s$. With respect to the average quiet Sun, the $\log(\tau) = 0.0$ surface was found to have a depression of $\approx 200\text{ km}$ at peak intensity. Further, the density of the plasma in the bright point, and consequently the opacity, was found to be the lowest at the same time. This suggests that the radiation emitted from the deeper, hotter layers of a partially evacuated fluxtube continues to be the primary reason for the excess brightness of bright points at disk center. (see e.g. Carlsson et al. 2004, Shelyag et al. 2004, Keller et al. 2004). However, the effects of jet-like structures identified in the previous sections on the dynamical properties of facular bright points is presently unclear.

The temperature maps of the bright point also show notable similarities with the results of the spectropolarimetric inversions. For example, in the photosphere and at the middle node, the hottest regions of the bright point appear to be located on the edges of the magnetic flux distribution. The study by Buehler et al. (2015) using Hinode/SOT data (Kosugi et al. 2007, Tsuneta et al. 2008) produced similar results. Further, the simulated bright point was found to be hotter than the strong field regions of the faculae and the quiet Sun regions - similar to our observations. However, to properly compare the atmospheres of the spectropolarimetric inversions with the simulations, the synthetic images would

have to be degraded to the spatial resolution of the observations, followed by inverting them.

5.2.2.2 Magnetic fields in facular bright points

The maps of the line-of-sight magnetic field (B_{los}) are shown in the middle rows of Fig. 5.7 and Fig. 5.8. In agreement with the results established with the help of 3D-MHD magneto-convective simulations (see Vögler and Schüssler 2003, Keller et al. 2004, Carlsson et al. 2004), the magnetic fields in the facular elements are seen predominantly to be concentrated in the inter-granular lanes on account of flux-expulsion from the granules (Parker 1963). During the growth phase of the bright point, both the absolute field strength and B_{los} were found to increase identically in the centroid at $\log(\tau) = 0.0$ - from a value of 2 kilo-Gauss at $t = 47s$ to 2.5 kilo-Gauss at $t=77s$. Firstly, this is in agreement with the observation that the orientation of the magnetic field is mostly vertical in the bright point. Secondly, this implies that the intensification of the magnetic field is true, and not merely an artifact caused by the depression in the unity optical depth surface to deeper, less-inclined field regions. This inference is further justified by the observation that the density of the plasma within the bright point decreases at $\log(\tau) = 0.0$ with time until peak intensity is reached. Thus, in contrast to the observed area of the brightness in the synthetic images, the actual diameter of the fluxtube is found to stay approximately the same with time in the photosphere. For an intensification of the field strength by a factor of 1.25, the area should change by its inverse - a value that is too small to be detected in the simulated atmospheres, also because the magnetic features have a complex shape and are interconnected. The B_{los} maps in Fig. 5.7 ($t = 47s$) and Fig. 5.7 ($t = 77s$) tell a similar story - the fluxtube in the photospheric layer at $t = 77s$ already appears to have a different morphology than the one observed at $t = 47s$ so that the definition of a diameter is difficult. However, qualitatively, the area of the flux region that is co-spatial with the bright point does not seem to change significantly between the two snapshots. After the decay of the bright point at time $t = 149s$, the structure of the magnetic fluxtube is seen to show clear signs of shearing due to the action of horizontal convective flows. The fluxtube is almost split into two, and the field strengths were found to decrease to ≈ 2 kilo-Gauss again at the photosphere.

In comparing the B_{los} maps in Fig. 5.7 with those obtained from the inversions, a few qualitative agreements can be observed. The magnetic fields in the inverted maps appear to have a similar expansion profile compared to the simulations, and the diffuse appearance of the magnetic field at the top node is visible in both maps. Also, at $\log(\tau) = 0.0, -1.0$, in Fig. 5.7, Fig. 5.8, and Fig. 5.9, opposite polarity fields are seen adjacent to the dominant polarity at all times, usually in the form of thin flux sheets. Such a configuration can also be found at the photosphere in the map of B_{los} obtained with inversions. Although the 3D geometry of these fields and their evolution is difficult to understand without the use of more sophisticated methods like field-line tracing, such fields seem to preferably occur at lower heights, suggesting that interaction of the turbulent convection with the flux patches also leads to the generation of turbulent fields at the photosphere. Compared to the internal energy density of photospheric plasma, the stored magnetic energy density in these fields is far too small to affect the thermodynamics of the gas at photospheric

heights. Flux cancellation between patches of opposite polarity have been hypothesized to affect the energetics of coronal loops, however (see e.g. Chitta et al. 2017).

5.2.2.3 Velocities in facular bright points

The panels in the bottom row of Fig. 5.7, Fig. 5.8, and Fig. 5.9 show maps of v_{los} from MURaM simulations obtained at the nodes mentioned earlier. The color convention used in spectropolarimetry has been adopted for v_{los} maps, and the order of figures themselves, in the order listed above, correspond to the times $t = 47s, 77s, 149s$. From these maps, a few striking features are easily observed. Firstly, the region broadly associated with the bright point is seen to be composed of several plumes of upflows, for example, at the (x, y) locations $(0.4'', 0.6'')$, $(0.2'', 0.5'')$, and $(0.1'', 0.4'')$ to the left of the dark contour in the bottom left panel of Fig. 5.7 i.e. $\log(\tau) = 0.0$. Similar upflow regions can also be found to the right of the central fluxtube along the inter-granular lane. These plumes give the visual appearance of islands embedded in a background sea of downflows. Upon zooming further into the field of view, these 'islands' also appear to be connected by weak sheets of magnetic flux, which are especially visible in Fig. 5.7. Going by the visual structure of these islands, it seems plausible that fragments of the magnetic field break away from the flux concentration due to the shearing forces of horizontal convective flows via the Kelvin-Helmholtz instability.

At time $t = 47s$ (Fig. 5.7), typical plasma speeds of $0.5 - 1.0 \text{ km/s}$ were found in the compact upflow regions adjacent to the bright point. For the upflow region near the edge of the FOV $(0.1'', 0.4'')$, stronger and more uniform velocities of 2.5 km/s were found. The bright point (indicated by the dark contour), interestingly, seems to be co-spatial with the interface of upflows and downflow that occur well within the boundaries of the flux distribution. The pixels enclosed by the contour include a fast downflow region (6 km/s) adjacent to the interface, and a slow upflow (-0.1 km/s) region at the photosphere. The respective values in the middle node are 4 km/s and -1 km/s . Therefore, these columns of opposite flows separated by an interface stretch several hundred kilometers into the solar atmosphere, as can be verified in the bottom center panel of Fig. 5.7. However, it is unclear how, and why such systems form within a single flux distribution. As the bright point evolves and reaches peak intensity at time $t = 77s$ (Fig. 5.8), the bi-directional flow interface regions within the flux distribution constituting the bright point become more diffuse, and the upflow islands mentioned above appear elongated in the photosphere, both in the photosphere and the middle node. At the top node, however, the pattern of v_{los} seems to suggest that the magnetic field is also twisted in the bright point. In this peak intensity phase, where the bright point continues to radiate away energy for approximately half a minute, the strongest upflow and downflow speeds found within the region encircled by the dark contour are -1.4 km/s , and 4 km/s - similar to the values reported for the earlier time-stamp. The corresponding values in the middle node are -1.05 km/s and 7.2 km/s . Finally, after the decay of the bright point at time $t = 149s$ (Fig. 5.9), a strong and voluminous upflow region forms at the photosphere and the middle node, with upflow speeds of up to -3 km/s .

Further, scatter plots of the intensity of the pixels constituting the bright point vs their line-of-sight velocity show moderate correlation - the brightest pixels in the bright point

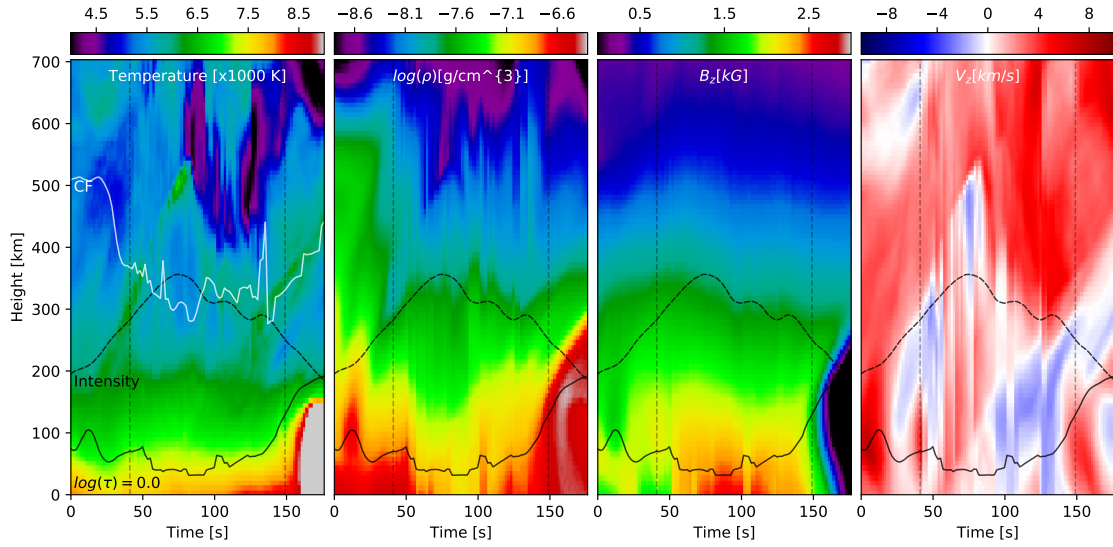


Figure 5.10: **From left:** Time-distance plots of the temperature (T), density ($\log(\rho)$), line-of-sight magnetic field (B_{los}), and the line-of-sight velocity (v_{los}).

tend to have upflows. This strongly indicates that the brightness in the simulated bright point is due to a dynamic mechanism(s) that actively heat(s) the interior of the fluxtube. In the next section, we provide further evidence for this hypothesis.

5.2.3 Time-distance analysis of facular jets

Fig. 5.10 shows the cropped height profile of four different physical quantities - temperature (T), logarithm of density ($\log(\rho)$), line-of-sight magnetic field (B_z) and the line-of-sight velocity (v_z) - at the centroid of the simulated bright point as a function of time. In every panel, the x and y co-ordinate represent time (t) and height (z), respectively. The zero position of the height does not correspond to the bottom boundary of the computation domain but an arbitrary height very close to the surface. The zero position of the time is the same epoch with respect to which time scales in the previous figures were displayed. The dashed semi-transparent vertical lines in the temperature panel represent the start (47s) and end times (149s) within which the bright point was tracked contiguously. The dashed black curves is the maximum core intensity of the bright point at each instant in time, the solid black line is the $\log(\tau) = 0.0$ position in each vertical profile, and the white line is the position of the weighted line-contribution function of the Fe I 6297.79Å spectral line. Thus, Fig. 5.10 represents a time-distance plot of the four physical parameters. The plots were constructed by tracking the bright point at each instant in time using a combination of intensity and area thresholds. Once the pixels constituting the bright point were identified, the centroid of the bright point was computed as the pixel with the highest core-intensity in the smoothed image. If the bright point did not exist (such as before 47s), the pseudo-centroid was chosen as the position at which the bright point first appears in the FOV. This was done so as to prevent huge jumps in the profiles that would otherwise appear as vertical discontinuities in the plots. Thus, both the lateral shifts of the centroid and the variations in the $\log(\tau) = 0.0$ position with time

are accounted for.

The most conspicuous feature in the temperature-plot on the left is the positive-sloped ridge. It represents a high-temperature front that is seen propagating from a height of 193.0 km at $t = 22\text{ s}$ to a height of 530 km at 82 s . This corresponds to a propagation speed of approximately 5.7 km/s . As mentioned in the previous sections, the periods of high intensity in the bright point are accompanied by a depression in the $\log(\tau) = 0.0$ surface. The corresponding line-formation regions also experience a shift in the downward direction. Further, another ridge at $t \simeq 120\text{ s}$ is observed to form, but with a smaller slope. This could be an indication of periodic excitation of shocks or jets, although analyses of longer time-series data are required for confirmation. In the density-plots, a similar ridge is found at the same location with a similar slope. Thus, the density and temperature plots indicate a shock, jet, or a magneto-acoustic wave propagating through the facular atmosphere. Due to the earlier observation that the core-intensity correlates with the direction of the line-of-sight velocity at the middle node, the propagating front is likely a shock, or a jet. The line-of-sight velocity plot also shows an identical ridge (blue regions are up-flows). The abrupt downflows at $t \simeq 60\text{ s}$ are possibly due to the sharp bi-directional flow interfaces that were observed in the bright point in Fig. 5.7 and Fig. 5.7. If small variations in the position of the centroid while tracking capture a region across such an interface, the flow will be observed to abruptly flip direction. Since the velocities of the downflows were observed to be supersonic (or near supersonic), the downflow ridges must be much steeper, which is what is observed. Thus, the possible existence of jets and shocks in faculae was briefly discussed in Sec 6.2.2 using the vector plots of the line-of-sight velocity. Fig. 5.10 is, therefore, taken to be stronger evidence of dynamical processes that actively participate in the heating of a bright point, an indication that is also supported by the strongly evolving Stokes I and V line-profiles in Fig. 5.4. More evidence of such ridges in other simulation runs of bright points is being found and gathered. We intend to discuss the results of the simulations as the inversions in more detail in the follow-up paper.

6 Conclusions and outlook

The work undertaken in this thesis was based on spectropolarimetric observations (slit-spectra) obtained with high spatial resolution ($0.1''$ at 6300\AA), high spectral sampling ($9\text{ m}\text{\AA}$), and good polarimetric sensitivity (10^{-2}) at the Swedish Solar Telescope (SST, Scharmer et al. (2003a)). The observations were obtained with the TRIPPEL spectrograph (Kiselman et al. 2011b) using a polarimeter based on the concept of the Fast Solar Polarimeter (FSP, Iglesias et al. (2016b)), with a modulation frequency of 100 Hz . The use of a spectrograph allowed the capture of a large range of wavelengths (spanning 18\AA) including several photospheric lines, which in turn act to better constrain the physical parameters deduced with spectropolarimetric inversions. Studies discussing the benefits of such multi-line inversions have been undertaken, for example, by Riethmüller and Solanki (2019). The thesis is divided into two broad sections - chapters 3 and 4 discuss the methods of image restoration and stray-light correction employed in restoring the data, while chapters 5 and 6 discuss the results of spectropolarimetric inversions and 3D radiative-MHD simulations of faculae and facular bright points.

Turbulence in the Earth's atmosphere causes severe image degradation in ground-based observations in the form of reduced spatial resolution, decreased polarimetric sensitivity, seeing-induced crosstalk, and stray-light contamination. The correction (or circumvention) of this degradation begins with the use of adaptive optics (AO) and post-facto image restoration techniques. Two well-known image restoration methods were briefly discussed in chapter 3 - speckle reconstruction (Keller and von der Luehe 1992a) and multi-frame blind deconvolution (MFBD, Paxman et al. (1992), Paxman et al. (1996)). In our observations, the latter method was used on the slit-jaw images to yield optical transfer functions with which the spectra recorded by the spectral cameras were subsequently restored. A comprehensive discussion of this procedure is found in van Noort (2017a). However, due to the limitations of the AO and the MFBD restoration method, the wings of the PSFs corresponding to the retrieved optical transfer functions are underestimated. This leads to the presence of residual image degradation even in the restored slit-spectra in the form of stray-light contamination. While stray-light contamination does not significantly affect the spatial resolution, the mixing of intensities still leads to undesirable modifications to the shapes of spectral lines, causing greater uncertainties in the physical parameters retrieved by inversion codes and generally poorer fits to the observed profiles.

Thus, in chapter 4, an improvement to a statistical method developed by Scharmer et al. (2010b) was discussed in detail, with the objective of quantifying (and removing) residual stray-light contamination in the observations. Only the component of stray light arising from high-order wave-front aberrations was addressed. The method relies on the

assumption that turbulence in the Earth's atmosphere is adequately described by Kolmogorov's theory (Kolmogorov 1941). In the first step, the values of the Fried parameter (Fried 1966) - a statistical quantity that characterises atmospheric seeing - reported by the AO during the observing period were used to generate an ensemble of Kolmogorov phase screens. Different methods of simulating such phase screens can be found in the literature (see for e.g. Noll 1976, McGlamery 1976, Lane et al. 1992, Glindemann et al. 1993). In the second step, the PSFs corresponding to every realisation of the phase screens were then used to degrade an image of solar granulation synthesised from an MHD-simulation snapshot. Since the phase screens are not corrected in any way, this step leads to the generation of synthetic, degraded images that would be identical (in the degree of image degradation) to observations obtained without the AO-compensation, under similar seeing conditions. Thirdly, since the efficiencies of the AO-compensations are generally unknown, the joint restoration of the synthetic dataset and the actual observations yields a way of estimating the efficiency with which the AO corrected wave-front aberrations in the actual observations. Finally, the computed efficiencies can be used to estimate the amount of residual image degradation (in the form of stray-light contamination) in the observations. While the method was found to improve the granulation contrasts in the observations from 9% to 12.5% (closer to the values found in images synthesized from state-of-the-art radiative-MHD simulations), the use of several simplifying approximations provide opportunities of improving the stray-light correction method in the following ways:

1. In observations obtained with an AO system composed of a single deformable mirror and wave-front sensor, the presence of high-altitude seeing also produces anisoplanatic aberrations in the incident wave fronts. Since the AO unavoidably applies wave-front corrections that are global to the FOV, the center of the FOV (AO hotspot) is likely to be better corrected than the edges. Due to the neglect of high-order aberrations, both by the AO and the MFBD restoration method, the issue of anisoplanatism is carried over to the residual stray-light contamination in observations. Therefore, an improvement to the method would be to simulate Kolmogorov phase screens that account for anisoplanatism, provided the different turbulent layers of the Earth's atmosphere are able to be characterised, each by a suitable Fried parameter. In our observations, the consequences of using isoplanatic wave fronts are that the stray-light contamination in the edges of the FOV are underestimated.
2. In the calculation of the AO efficiency, an iterative scheme can instead be setup to arrive at more accurate estimates. Initially, the set of efficiencies retrieved from the joint MFBD restorations can be used to generate another set of partially degraded synthetic images. Performing joint restorations with MFBD at each iteration, in principle, would lead to a convergence of the derived AO-efficiencies. Although this iterative scheme should, in principle, lead to exact convergence of the retrieved efficiencies, it incurs additional computational cost.
3. The stray-light correction method addresses residual stray light caused exclusively by high-order uncompensated wave-front aberrations. For a more satisfactory removal of stray-light from ground-based observations, other sources such as atmospheric scattering and instrumental scattering (due to the surface roughness of op-

tical elements) must be included. While it is generally difficult to characterise the former, progress is being made in characterising stray light of instrumental origin (see for e.g. Löfdahl and Scharmer 2012b).

4. In this thesis, the stray-light correction method was applied to slit-spectra. However, the method is also expected to work on observations obtained with filtergraphs and hyper-spectral imagers. A possible extension of the method described here is to test its consistency and validity on observations obtained with different instruments.

In chapter 5, the results of the spectropolarimetric inversions were discussed, with the objective of characterising the atmospheres in faculae and facular bright points. It is to be noted that the quality of image restoration methods used in this thesis, combined with the availability of multiple photospheric lines for inversions provided a unique opportunity to study the magnetic elements in faculae with increased reliability. In the quiet Sun, typical granulation velocities of $4 - 5 \text{ km/s}$ were observed, while a few select regions harbouring flows approaching the speed of sound were also found. The presence of fast downflows adjacent to magnetic flux distributions was earlier studied by Buehler et al. (2015), and several such regions have also been identified in our data. However, the presence of fast upflows and downflows in the quiet Sun is not well understood, and is potentially an interesting topic of future research. In agreement with several studies that can be found in the literature (see chapter 2 for references), the typical field strength of facular magnetic elements was found to be $1 - 2$ kilo-Gauss. These magnetic fields were found to be nearly vertical at the photospheric surface, expanding rapidly with height. Further, the spectropolarimetric inversions also reveal the existence of numerous regions of opposite polarity, confirming the findings of the study undertaken earlier by Buehler et al. (2015). While the close proximity of these regions to the dominant polarity suggest that they may be consequences of over-turning convection, other physical processes such as flux-emergence and the small-scale dynamo may also contribute to their existence in varying degrees. In the cores of the faculae, the average line-of-sight velocities at the photospheric surface (250 km/s) were found to be in agreement with values reported in literature (see, e.g., Solanki and Stenflo 1986). Additionally, a number of magnetic elements were also found to be associated with positive Stokes V relative amplitude asymmetries (Grossmann-Doerth et al. 1988, 1989, Solanki 1989).

At several locations near the edges of the large-scale flux distribution, facular bright points were identified in the line-core images of the Fe I 6297.79\AA , the Fe I 6301.5\AA , and the Fe I 6302.5\AA spectral lines. The inverted atmospheres reveal the bright points to be:

1. compact, bright structures with a distinct appearance in the line-core images.
2. significantly hotter than the cores of the faculae as well as the quiet Sun at all optical depth layers.
3. associated with downflows, on average, at the lower photospheric layers and showing larger Stokes V amplitude and area asymmetries compared to the magnetic elements of the faculae.
4. magnetic in nature with field strengths comparable to, if not slightly lower than, the strong-field regions of the faculae. .

These enumerated properties possibly indicate a fundamental distinction between magnetic elements in the faculae and facular bright points, the origin(s) and evolution(s) of which cannot be investigated with slit-spectra. Other studies that investigated the photometric and morphological properties exclusively of bright points in faculae, for example, have been made by Kobel et al. (2009, 2014).

Chapter 6 in the thesis discusses the results of 3D radiative-MHD simulations of faculae and a selected facular bright point, performed with the MURaM code (Vögler et al. 2005a). The simulations were run with high grid resolution and cadence to enable a study of their evolution. In the simulated faculae, the bright point was observed to spontaneously form and disappear with a lifetime of $\approx 2 \text{ min}$. Analysis of the physical parameters in the bright point indicate a complex and dynamic atmosphere with a structuring that may be beyond the spatial resolution of modern spectropolarimetric observations. In particular, maps of the line-of-sight velocity at various stages of the bright point's life indicate interface regions separating columns of bi-directional flows, with a persistent upflow in the centroid of the bright point. Further, tracking the bright point's lateral movement with time revealed a conspicuous propagation of a high-temperature front from the solar surface upwards into the lower solar atmosphere in the time-distance plots. Although the origin(s) and cause(s) of this front are unclear, the propagating front was found to participate in the evolution of the bright point's intensity. This may be an indication of additional dynamical processes that contribute to the photometric properties of bright points in faculae. Thus, we intend to further expand our investigation of facular bright points using 3D radiative-MHD simulations in the following ways:

1. Performing additional simulations of faculae and compiling a catalogue of high-resolution, high-cadence bright points, with the aim of studying their thermodynamic and magnetic properties statistically.
2. Understanding the origin(s) and cause(s) of the propagating fronts, especially if they are a common occurrence in simulated bright points.
3. Synthesising Stokes profiles from the simulation snapshots followed by degrading them to the spatial and spectral resolution of the observations. This would facilitate a direct comparison of the inverted atmospheres between simulations and observations, in addition to clarifying the effects of spatial resolution on the inverted atmospheres of bright points.

Thus, the work on stray-light correction, undertaken as part of this thesis, may help in improving the quality of ground-based observations, and indirectly the reliability of atmospheres retrieved with spectropolarimetric inversions. However, its efficacy on data obtained with different instruments is yet to be rigorously tested. Finally, the preliminary work on the properties of facular bright points is intended to be the first step in a larger, simulation-based study of numerous facular bright points. This may help us understand not only their origins, but also their contribution to solar irradiance and its variability.

Another important step in the study of small-scale magnetic features is their investigation with a hyperspectral imager (or integral field unit), such as a Microlens Hyperspectral Imager (MiHI), which has been recently installed at the Swedish Solar Telescope. Data

taken with this instrument cover both spatial dimensions and the spectrum, analysis of which would allow the determination of not just the structure of magnetic features, as done here, but also their dynamics.

Bibliography

- Alfvén, H.: 1942, *Nature* **150(3805)**, 405
- Asplund, M., Grevesse, N., Sauval, A. J., and Scott, P.: 2009, *ARA&A* **47(1)**, 481
- Auer, L. H., Heasley, J. N., and House, L. L.: 1977, *Sol. Phys.* **55(1)**, 47
- Babcock, H. W.: 1953, *ApJ* **118**, 387
- Babcock, H. W. and Babcock, H. D.: 1955, *ApJ* **121**, 349
- Barthol, P., Gandorfer, A., Solanki, S. K., Schüssler, M., Chares, B., Curdt, W., Deutsch, W., Feller, A., Germerott, D., Grauf, B., Heerlein, K., Hirzberger, J., Kolleck, M., Meller, R., Müller, R., Riethmüller, T. L., Tomasch, G., Knölker, M., Lites, B. W., Card, G., Elmore, D., Fox, J., Lecinski, A., Nelson, P., Summers, R., Watt, A., Martínez Pillet, V., Bonet, J. A., Schmidt, W., Berkefeld, T., Title, A. M., Domingo, V., Gasent Blesa, J. L., Del Toro Iniesta, J. C., López Jiménez, A., Álvarez-Herrero, A., Sabau-Graziati, L., Widani, C., Haberler, P., Härtel, K., Kampf, D., Levin, T., Pérez Grande, I., Sanz-Andrés, A., and Schmidt, E.: 2011, *Sol. Phys.* **268(1)**, 1
- Baur, T. G., Elmore, D. E., Lee, R. H., Querfeld, C. W., and Rogers, S. R.: 1981, *Sol. Phys.* **70(2)**, 395
- Baur, T. G., House, L. L., and Hull, H. K.: 1980, *Sol. Phys.* **65(1)**, 111
- Beck, C., Rezaei, R., and Fabbian, D.: 2011, *A&A* **535**, A129
- Beckers, J. M.: 1968, *Sol. Phys.* **5(1)**, 15
- Beckers, J. M. and Schröter, E. H.: 1968, *Sol. Phys.* **4(2)**, 142
- Bellot Rubio, L. and Orozco Suárez, D.: 2019, *Living Reviews in Solar Physics* **16(1)**, 1
- Berger, T. E., Rouppe van der Voort, L., and Löfdahl, M.: 2007, *ApJ* **661(2)**, 1272
- Bernasconi, P. N., Keller, C. U., and Stenflo, J. O.: 1994, in K. S. Balasubramaniam and G. W. Simon (eds.), *Solar Active Region Evolution: Comparing Models with Observations*, Vol. 68 of *Astronomical Society of the Pacific Conference Series*, p. 131
- Borrero, J. M., Asensio Ramos, A., Collados, M., Schlichenmaier, R., Balthasar, H., Franz, M., Rezaei, R., Kiess, C., Orozco Suárez, D., Pastor, A., Berkefeld, T., von

- der Lühe, O., Schmidt, D., Schmidt, W., Sigwarth, M., Soltau, D., Volkmer, R., Waldmann, T., Denker, C., Hofmann, A., Staude, J., Strassmeier, K. G., Feller, A., Lagg, A., Solanki, S. K., Sobotka, M., and Nicklas, H.: 2016, *A&A* **596**, A2
- Brault, J. W.: 1978, in G. Godoli (ed.), *Future solar optical observations needs and constraints*, Vol. 106, p. 33
- Buehler, D., Lagg, A., Solanki, S. K., and van Noort, M.: 2015, *A&A* **576**, A27
- Caccin, B., Falciani, R., and Donati-Falchi, A.: 1974, *Sol. Phys.* **35(1)**, 41
- Cally, P. S. and Bogdan, T. J.: 1997, *ApJ* **486(1)**, L67
- Carlsson, M., Stein, R. F., Nordlund, Å., and Scharmer, G. B.: 2004, *ApJ* **610(2)**, L137
- Chapman, G. A.: 1970, *Sol. Phys.* **14(2)**, 315
- Chapman, G. A.: 1977, *ApJS* **33**, 35
- Chapman, G. A.: 1979, *ApJ* **232**, 923
- Chapman, G. A. and Klabunde, D. P.: 1982, *ApJ* **261**, 387
- Chapman, G. A. and Sheeley, N. R., J.: 1968, *Sol. Phys.* **5(4)**, 442
- Cheung, M. C. M., Rempel, M., Title, A. M., and Schüssler, M.: 2010, *ApJ* **720(1)**, 233
- Chitta, L. P., Peter, H., Solanki, S. K., Barthol, P., Gandorfer, A., Gizon, L., Hirzberger, J., Riethmüller, T. L., van Noort, M., Blanco Rodríguez, J., Del Toro Iniesta, J. C., Orozco Suárez, D., Schmidt, W., Martínez Pillet, V., and Knölker, M.: 2017, *ApJS* **229(1)**, 4
- Danilovic, S., Gandorfer, A., Lagg, A., Schüssler, M., Solanki, S. K., Vögler, A., Katsukawa, Y., and Tsuneta, S.: 2008, *A&A* **484**, L17
- David, K. H. and Elste, G.: 1962, *ZAp* **54**, 12
- de la Cruz Rodríguez, J. and van Noort, M.: 2017, *Space Sci. Rev.* **210(1-4)**, 109
- De Pontieu, B., Carlsson, M., Stein, R., Rouppe van der Voort, L., Löfdahl, M., van Noort, M., Nordlund, Å., and Scharmer, G.: 2006, *ApJ* **646(2)**, 1405
- Defouw, R. J.: 1976, *ApJ* **209**, 266
- Deinzer, W., Hensler, G., Schussler, M., and Weisshaar, E.: 1984, *A&A* **139**, 435
- del Toro Iniesta, J. C.: 2003, *Introduction to Spectropolarimetry*
- Delbouille, L., Roland, G., and Neven, L.: 1973a, *Atlas photometrique du spectre solaire de [λ] 3000 a [λ] 10000*
- Delbouille, L., Roland, G., and Neven, L.: 1973b, *Atlas photometrique du spectre solaire de [λ] 3000 a [λ] 10000*

- Delbouille, L., Roland, G., and Neven, L.: 1989, *Atlas photometrique du spectre solaire de [λ] 3000 a [λ] 10000. Vol.2*
- Dunn, R. B. and Zirker, J. B.: 1973, *Sol. Phys.* **33(2)**, 281
- Foukal, P., Duvall, T., J., and Gillipsie, B.: 1981, *ApJ* **249**, 394
- Frazier, E. N.: 1971, *Sol. Phys.* **21(1)**, 42
- Frazier, E. N. and Stenflo, J. O.: 1972, *Sol. Phys.* **27(2)**, 330
- Freytag, B., Steffen, M., Ludwig, H. G., Wedemeyer-Böhm, S., Schaffenberger, W., and Steiner, O.: 2012, *Journal of Computational Physics* **231(3)**, 919
- Fried, D. L.: 1966, *Journal of the Optical Society of America (1917-1983)* **56(10)**, 1372
- Fried, D. L.: 1966, *J. Opt. Soc. Am.* **56(10)**, 1372
- Frutiger, C., Solanki, S. K., Fligge, M., and Bruls, J. H. M. J.: 2000a, *A&A* **358**, 1109
- Frutiger, C., Solanki, S. K., Fligge, M., and Bruls, J. H. M. J.: 2000b, *A&A* **358**, 1109
- Gezari, D. Y., Labeyrie, A., and Stachnik, R. V.: 1972, *ApJ* **173**, L1
- Gingerich, O. and de Jager, C.: 1968, *Sol. Phys.* **3(1)**, 5
- Gingerich, O., Noyes, R. W., Kalkofen, W., and Cuny, Y.: 1971, *Sol. Phys.* **18(3)**, 347
- Giovanelli, R. G. and Brown, N.: 1977, *Sol. Phys.* **52(1)**, 27
- Giovanelli, R. G. and Ramsay, J. V.: 1971, in R. Howard (ed.), *Solar Magnetic Fields*, Vol. 43, p. 293
- Giovanelli, R. G. and Slaughter, C.: 1978, *Sol. Phys.* **57(2)**, 255
- Glindemann, A., Lane, R. G., and Dainty, J. C.: 1993, *Journal of Modern Optics* **40**, 2381
- Grigorjev, V. M.: 1969, *Sol. Phys.* **6(1)**, 67
- Grossmann-Doerth, U., Schuessler, M., and Solanki, S. K.: 1988, *A&A* **206(2)**, L37
- Grossmann-Doerth, U., Schuessler, M., and Solanki, S. K.: 1989, *A&A* **221(2)**, 338
- Grossmann-Doerth, U., Schuessler, M., and Steiner, O.: 1998, *A&A* **337**, 928
- Gudiksen, B. V., Carlsson, M., Hansteen, V. H., Hayek, W., Leenaarts, J., and Martínez-Sykora, J.: 2011, *A&A* **531**, A154
- Harvey, J. and Hall, D.: 1975, in *Bulletin of the American Astronomical Society*, Vol. 7, p. 459
- Harvey, J. and Livingston, W.: 1969, *Sol. Phys.* **10(2)**, 283

- Harvey, J., Livingston, W., and Slaughter, C.: 1972, in *Line Formation in the Presence of Magnetic Fields*, p. 227
- Hasan, S. S.: 1985, *A&A* **143(1)**, 39
- Howard, R.: 1959, *ApJ* **130**, 193
- Howard, R.: 1967, *ARA&A* **5**, 1
- Ichimoto, K., Lites, B., Elmore, D., Suematsu, Y., Tsuneta, S., Katsukawa, Y., Shimizu, T., Shine, R., Tarbell, T., Title, A., Kiyohara, J., Shinoda, K., Card, G., Lecinski, A., Streander, K., Nakagiri, M., Miyashita, M., Noguchi, M., Hoffmann, C., and Cruz, T.: 2008, *Sol. Phys.* **249(2)**, 233
- Iglesias, F. A., Feller, A., Nagaraju, K., and Solanki, S. K.: 2016a, *A&A* **590**, A89
- Iglesias, F. A., Feller, A., Nagaraju, K., and Solanki, S. K.: 2016b, *A&A* **590**, A89
- Kahil, F., Riethmüller, T. L., and Solanki, S. K.: 2017, *ApJS* **229(1)**, 12
- Keller, C. U.: 1992, *Nature* **359(6393)**, 307
- Keller, C. U. and Johannesson, A.: 1995, *A&AS* **110**, 565
- Keller, C. U., Schüssler, M., Vögler, A., and Zakharov, V.: 2004, *ApJ* **607(1)**, L59
- Keller, C. U., Steiner, O., Stenflo, J. O., and Solanki, S. K.: 1990, *A&A* **233(2)**, 583
- Keller, C. U. and von der Luehe, O.: 1992a, *A&A* **261(1)**, 321
- Keller, C. U. and von der Luehe, O.: 1992b, *A&A* **261**, 321
- Khomenko, E., Collados, M., and Felipe, T.: 2008, *Sol. Phys.* **251(1-2)**, 589
- Khomenko, E. V., Shelyag, S., Solanki, S. K., and Vögler, A.: 2005, *A&A* **442(3)**, 1059
- Kiepenheuer, K. O.: 1953, *ApJ* **117**, 447
- Kiselman, D., Pereira, T., Gustafsson, B., Asplund, M., Meléndez, J., and Langhans: 2011a, *A&A* **535**, A14
- Kiselman, D., Pereira, T. M. D., Gustafsson, B., Asplund, M., Meléndez, J., and Langhans, K.: 2011b, *A&A* **535**, A14
- Knoelker, M., Schuessler, M., and Weisshaar, E.: 1988, *A&A* **194(1-2)**, 257
- Knox, K. T. and Thompson, B. J.: 1973, *ApJ* **182**, L133
- Kobel, P., Hirzberger, J., and Solanki, S. K.: 2014, *arXiv e-prints* p. arXiv:1410.5354
- Kobel, P., Hirzberger, J., Solanki, S. K., Gandorfer, A., and Zakharov, V.: 2009, *A&A* **502(1)**, 303

- Kobel, P., Solanki, S. K., and Borrero, J. M.: 2011, *A&A* **531**, A112
- Kolmogorov, A.: 1941, *Akademiia Nauk SSSR Doklady* **30**, 301
- Kosugi, T., Matsuzaki, K., Sakao, T., Shimizu, T., Sone, Y., Tachikawa, S., Hashimoto, T., Minesugi, K., Ohnishi, A., Yamada, T., Tsuneta, S., Hara, H., Ichimoto, K., Suematsu, Y., Shimojo, M., Watanabe, T., Shimada, S., Davis, J. M., Hill, L. D., Owens, J. K., Title, A. M., Culhane, J. L., Harra, L. K., Doschek, G. A., and Golub, L.: 2007, *Sol. Phys.* **243(1)**, 3
- Koutchmy, S. and Stellmacher, G.: 1978, *A&A* **67(1)**, 93
- Kurucz, R. L. and Bell, B.: 1995, *Atomic line list*
- Labeyrie, A.: 1970, *A&A* **6**, 85
- Landi Degl'Innocenti, E. and Landi Degl'Innocenti, M.: 1977, *A&A* **56**, 111
- Landi Degl'Innocenti, E. and Landolfi, M.: 2004, *Polarization in Spectral Lines*, Vol. 307
- Lane, R. G., Glindemann, A., and Dainty, J. C.: 1992, *Waves in Random Media* **2**, 209
- Lawrence, J. K. and Chapman, G. A.: 1988, *ApJ* **335**, 996
- Lawrence, J. K., Chapman, G. A., and Herzog, A. D.: 1988, *ApJ* **324**, 1184
- Lawrence, J. K., Topka, K. P., and Jones, H. P.: 1993, *J. Geophys. Res.* **98(A11)**, 18911
- Leenaarts, J.: 2020, *Living Reviews in Solar Physics* **17(1)**, 3
- Leighton, R. B.: 1959, *ApJ* **130**, 366
- Leighton, R. B., Noyes, R. W., and Simon, G. W.: 1962, *ApJ* **135**, 474
- Lites, B. W., Scharmer, G. B., Berger, T. E., and Title, A. M.: 2004, *Sol. Phys.* **221(1)**, 65
- Löfdahl, M. G. and Scharmer, G. B.: 1994a, *A&AS* **107**, 243
- Löfdahl, M. G. and Scharmer, G. B.: 1994b, *A&AS* **107**, 243
- Löfdahl, M. G. and Scharmer, G. B.: 2012a, *A&A* **537**, A80
- Löfdahl, M. G. and Scharmer, G. B.: 2012b, *A&A* **537**, A80
- Mackay, D. H. and Yeates, A. R.: 2012, *Living Reviews in Solar Physics* **9(1)**, 6
- Martínez González, M. J., Bellot Rubio, L. R., Solanki, S. K., Martínez Pillet, V., Del Toro Iniesta, J. C., Barthol, P., and Schmidt, W.: 2012, *ApJ* **758(2)**, L40
- Martínez Pillet, V.: 1992, *Sol. Phys.* **140(2)**, 207

- Martínez Pillet, V., Del Toro Iniesta, J. C., Álvarez-Herrero, A., Domingo, V., Bonet, J. A., González Fernández, L., López Jiménez, A., Pastor, C., Gasent Blesa, J. L., Mellado, P., Piqueras, J., Aparicio, B., Balaguer, M., Ballesteros, E., Belenguer, T., Bellot Rubio, L. R., Berkefeld, T., Collados, M., Deutsch, W., Feller, A., Girela, F., Grauf, B., Heredero, R. L., Herranz, M., Jerónimo, J. M., Laguna, H., Meller, R., Menéndez, M., Morales, R., Orozco Suárez, D., Ramos, G., Reina, M., Ramos, J. L., Rodríguez, P., Sánchez, A., Uribe-Patarroyo, N., Barthol, P., Gandorfer, A., Knoelker, M., Schmidt, W., Solanki, S. K., and Vargas Domínguez, S.: 2011a, *Sol. Phys.* **268**(1), 57
- Martínez Pillet, V., Del Toro Iniesta, J. C., Álvarez-Herrero, A., Domingo, V., Bonet, J. A., González Fernández, L., López Jiménez, A., Pastor, C., Gasent Blesa, J. L., Mellado, P., Piqueras, J., Aparicio, B., Balaguer, M., Ballesteros, E., Belenguer, T., Bellot Rubio, L. R., Berkefeld, T., Collados, M., Deutsch, W., Feller, A., Girela, F., Grauf, B., Heredero, R. L., Herranz, M., Jerónimo, J. M., Laguna, H., Meller, R., Menéndez, M., Morales, R., Orozco Suárez, D., Ramos, G., Reina, M., Ramos, J. L., Rodríguez, P., Sánchez, A., Uribe-Patarroyo, N., Barthol, P., Gandorfer, A., Knoelker, M., Schmidt, W., Solanki, S. K., and Vargas Domínguez, S.: 2011b, *Sol. Phys.* **268**(1), 57
- Martínez Pillet, V., Lites, B. W., and Skumanich, A.: 1997, *ApJ* **474**(2), 810
- Mathew, S. K., Zakharov, V., and Solanki, S. K.: 2009, *A&A* **501**(3), L19
- Mattig, W.: 1971, *Sol. Phys.* **18**, 434
- McGlamery, B. L.: 1976, in J. C. Urbach (ed.), *Image processing*, Vol. 74 of *Proc. SPIE*, pp 225–233
- Mehlretter, J. P.: 1974, *Sol. Phys.* **38**(1), 43
- Muller, R. and Keil, S. L.: 1983, *Sol. Phys.* **87**(2), 243
- Nagaraju, K. and Feller, A.: 2012, *arXiv e-prints*
- Narayan, G. and Scharmer, G. B.: 2010, *A&A* **524**, A3
- Nicholls, T. W., Boreman, G. D., and Dainty, J. C.: 1995, *Optics Letters* **20**, 2460
- Nishikawa, J. and Hirayama, T.: 1990, *Sol. Phys.* **127**(2), 211
- Noll, R. J.: 1976, *Journal of the Optical Society of America (1917-1983)* **66**, 207
- Nordlund, A.: 1982, *A&A* **107**, 1
- Okunev, O. V. and Kneer, F.: 2005, *A&A* **439**(1), 323
- Orozco-Suárez, D., Bellot-Rubio, L. R., and del Toro Iniesta, J. C.: 2007, *The Astrophysical Journal Letters* **662**(1), L31
- Ortiz, A., Solanki, S. K., Domingo, V., Fligge, M., and Sanahuja, B.: 2002, *A&A* **388**, 1036

- Parker, E. N.: 1963, *ApJ* **138**, 552
- Parker, E. N.: 1974, *ApJ* **190**, 429
- Parker, E. N.: 1976a, *ApJ* **204**, 259
- Parker, E. N.: 1976b, *ApJ* **204**, 259
- Parker, E. N.: 1978, *ApJ* **221**, 368
- Paxman, R. G., Schulz, T. J., and Fienup, J. R.: 1992, *J. Opt. Soc. Am. A* **9(7)**, 1072
- Paxman, R. G., Seldin, J. H., Loefeldahl, M. G., Scharmer, G. B., and Keller, C. U.: 1996, *ApJ* **466**, 1087
- Rao, C., Jiang, W., and Ling, N.: 2000, *Journal of Modern Optics* **47**, 1111
- Rees, D. E., Murphy, G. A., and Durrant, C. J.: 1989, *ApJ* **339**, 1093
- Rempel, M.: 2011, *ApJ* **740(1)**, 15
- Rempel, M.: 2014, *ApJ* **789(2)**, 132
- Rempel, M.: 2017, *ApJ* **834(1)**, 10
- Rempel, M., Schüssler, M., and Knölker, M.: 2009, *ApJ* **691(1)**, 640
- Riethmüller, T. L. and Solanki, S. K.: 2017, *A&A* **598**, A123
- Riethmüller, T. L. and Solanki, S. K.: 2019, *A&A* **622**, A36
- Riethmüller, T. L., Solanki, S. K., Berdyugina, S. V., Schüssler, M., Martínez Pillet, V., Feller, A., Gandorfer, A., and Hirzberger, J.: 2014, *A&A* **568**, A13
- Rieutord, M. and Rincon, F.: 2010, *Living Reviews in Solar Physics* **7(1)**, 2
- Rimmele, T. R. and Marino, J.: 2011, *Living Reviews in Solar Physics* **8(1)**, 2
- Rimmele, T. R. and Marino, J.: 2011, *Living Reviews in Solar Physics* **8(1)**, 2
- Roberts, B. and Webb, A. R.: 1978, *Sol. Phys.* **56(1)**, 5
- Roddier, F.: 2004, *Adaptive Optics in Astronomy*
- Rogerson, John B., J.: 1961, *ApJ* **134**, 331
- Ruiz Cobo, B. and del Toro Iniesta, J. C.: 1992, *ApJ* **398**, 375
- Sánchez Cuberes, M., Bonet, J. A., Vázquez, M., and Wittmann, A. D.: 2000, *ApJ* **538**, 940
- Sánchez Cuberes, M., Vázquez, M., Bonet, J. A., and Sobotka, M.: 2002, *ApJ* **570(2)**, 886

- Sarazin, M. and Roddier, F.: 1990, *A&A* **227**, 294
- Scharmer, G. B., Bjelksjo, K., Korhonen, T. K., Lindberg, B., and Petterson, B.: 2003a, in S. L. Keil and S. V. Avakyan (eds.), *Proc. SPIE*, Vol. 4853 of *Society of Photo-Optical Instrumentation Engineers (SPIE) Conference Series*, pp 341–350
- Scharmer, G. B., Bjelksjo, K., Korhonen, T. K., Lindberg, B., and Petterson, B.: 2003b, in S. L. Keil and S. V. Avakyan (eds.), *Innovative Telescopes and Instrumentation for Solar Astrophysics*, Vol. 4853 of *Proc. SPIE*, pp 341–350
- Scharmer, G. B., Löfdahl, M. G., van Werkhoven, T. I. M., and de la Cruz Rodríguez, J.: 2010a, *A&A* **521**, A68
- Scharmer, G. B., Löfdahl, M. G., van Werkhoven, T. I. M., and de la Cruz Rodríguez, J.: 2010b, *A&A* **521**, A68
- Scherrer, P. H., Schou, J., Bush, R. I., Kosovichev, A. G., Bogart, R. S., Hoeksema, J. T., Liu, Y., Duvall, T. L., Zhao, J., Title, A. M., Schrijver, C. J., Tarbell, T. D., and Tomczyk, S.: 2012, *Sol. Phys.* **275(1)**, 207
- Schmahl, G.: 1967, *ZAp* **66**, 81
- Severny, A.: 1964, *Space Sci. Rev.* **3(4)**, 451
- Sheeley, N. R., J.: 1966, *ApJ* **144**, 723
- Sheeley, N. R., J.: 1967, *Sol. Phys.* **1(2)**, 171
- Shelyag, S., Schüssler, M., Solanki, S. K., Berdyugina, S. V., and Vögler, A.: 2004, *A&A* **427**, 335
- Shimizu, T., Nagata, S., Tsuneta, S., Tarbell, T., Edwards, C., Shine, R., Hoffmann, C., Thomas, E., Sour, S., Rehse, R., Ito, O., Kashiwagi, Y., Tabata, M., Kodeki, K., Nagase, M., Matsuzaki, K., Kobayashi, K., Ichimoto, K., and Suematsu, Y.: 2008, *Sol. Phys.* **249(2)**, 221
- Simon, G. W. and Leighton, R. B.: 1964, *ApJ* **140**, 1120
- Simon, G. W. and Noyes, R. W.: 1971, in R. Howard (ed.), *Solar Magnetic Fields*, Vol. 43, p. 663
- Sirajul Hasan, S.: 1984, *ApJ* **285**, 851
- Skumanich, A. and Lites, B. W.: 1987, *ApJ* **322**, 473
- Solanki, S. K.: 1986, *A&A* **168(1-2)**, 311
- Solanki, S. K.: 1989, *A&A* **224(1-2)**, 225
- Solanki, S. K.: 1993, *Space Sci. Rev.* **63(1-2)**, 1

- Solanki, S. K., Barthol, P., Danilovic, S., Feller, A., Gandorfer, A., Hirzberger, J., Riethmüller, T. L., Schüssler, M., Bonet, J. A., Martínez Pillet, V., del Toro Iniesta, J. C., Domingo, V., Palacios, J., Knölker, M., Bello González, N., Berkefeld, T., Franz, M., Schmidt, W., and Title, A. M.: 2010, *ApJ* **723(2)**, L127
- Solanki, S. K. and Pahlke, K. D.: 1988, *A&A* **201(1)**, 143
- Solanki, S. K. and Stenflo, J. O.: 1984, *A&A* **140(1)**, 185
- Solanki, S. K. and Stenflo, J. O.: 1986, *A&A* **170(1)**, 120
- Spruit, H. C.: 1976, *Sol. Phys.* **50(2)**, 269
- Spruit, H. C.: 1979, *Sol. Phys.* **61(2)**, 363
- Spruit, H. C.: 1991, *Absorption of p-Mode Waves by Magnetic Fields*, Vol. 388, pp 121–134
- Spruit, H. C. and Zweibel, E. G.: 1979, *Sol. Phys.* **62(1)**, 15
- Staveland, L.: 1970, *Sol. Phys.* **12**, 328
- Stein, R. F.: 2012, *Living Reviews in Solar Physics* **9(1)**, 4
- Stein, R. F. and Nordlund, Å.: 1998, *ApJ* **499(2)**, 914
- Steiner, O., Grossmann-Doerth, U., Knölker, M., and Schüssler, M.: 1998, *ApJ* **495(1)**, 468
- Stellmacher, G. and Wiehr, E.: 1971, *Sol. Phys.* **18(2)**, 220
- Stellmacher, G. and Wiehr, E.: 1973, *A&A* **29**, 13
- Stenflo, J. O.: 1966, *Arkiv for Astronomi* **4**, 173
- Stenflo, J. O.: 1973, *Sol. Phys.* **32(1)**, 41
- Stenflo, J. O.: 1975, *Sol. Phys.* **42(1)**, 79
- Stenflo, J. O., Solanki, S., Harvey, J. W., and Brault, J. W.: 1984, *A&A* **131(2)**, 333
- Stumpff, P.: 1961, *Veroeffentlichungen der Universitaets-Sternwarte zu Goettingen* **7**, 305
- Suematsu, Y., Tsuneta, S., Ichimoto, K., Shimizu, T., Otsubo, M., Katsukawa, Y., Nagagiri, M., Noguchi, M., Tamura, T., Kato, Y., Hara, H., Kubo, M., Mikami, I., Saito, H., Matsushita, T., Kawaguchi, N., Nakaoji, T., Nagae, K., Shimada, S., Takeyama, N., and Yamamuro, T.: 2008, *Sol. Phys.* **249(2)**, 197
- Takeuchi, A.: 1993, *PASJ* **45**, 811
- Tarbell, T. D. and Title, A. M.: 1977, *Sol. Phys.* **52(1)**, 13
- Thiessen, G.: 1952, *Nature* **169(4291)**, 147

- Title, A. M., Topka, K. P., Tarbell, T. D., Schmidt, W., Balke, C., and Scharmer, G.: 1992, *ApJ* **393**, 782
- Topka, K. P., Tarbell, T. D., and Title, A. M.: 1992, *ApJ* **396**, 351
- Topka, K. P., Tarbell, T. D., and Title, A. M.: 1997, *ApJ* **484(1)**, 479
- Tsuneta, S., Ichimoto, K., Katsukawa, Y., Nagata, S., Otsubo, M., Shimizu, T., Suematsu, Y., Nakagiri, M., Noguchi, M., Tarbell, T., Title, A., Shine, R., Rosenberg, W., Hoffmann, C., Jurcevich, B., Kushner, G., Levay, M., Lites, B., Elmore, D., Matsushita, T., Kawaguchi, N., Saito, H., Mikami, I., Hill, L. D., and Owens, J. K.: 2008, *Sol. Phys.* **249(2)**, 167
- Uitenbroek, H., Tritschler, A., and Rimmele, T.: 2007, *The Astrophysical Journal* **668(1)**, 586
- Unno, W.: 1956, *PASJ* **8**, 108
- van Noort, M.: 2012, *A&A* **548**, A5
- van Noort, M.: 2017a, *A&A* **608**, A76
- van Noort, M.: 2017b, *A&A* **608**, A76
- van Noort, M., Rouppe van der Voort, L., and Löfdahl, M. G.: 2005, *Sol. Phys.* **228**, 191
- Vecchio, A., Cauzzi, G., and Reardon, K. P.: 2009, *A&A* **494(1)**, 269
- Vögler, A. and Schüssler, M.: 2003, *Astronomische Nachrichten* **324(4)**, 399
- Vögler, A. and Schüssler, M.: 2007, *A&A* **465(3)**, L43
- Vögler, A., Shelyag, S., Schüssler, M., Cattaneo, F., Emonet, T., and Linde, T.: 2005a, *A&A* **429**, 335
- Vögler, A., Shelyag, S., Schüssler, M., Cattaneo, F., Emonet, T., and Linde, T.: 2005b, *A&A* **429**, 335
- von der Luehe, O.: 1985, *High Resolution Speckle Imaging of Solar Small-Scale Structure: the Influence of Anisoplanatism*, Vol. 223, p. 96
- von der Luhe, O.: 1987, in J. W. Goad (ed.), *Interferometric Imaging in Astronomy*, p. 37
- von der Luhe, O. and Dunn, R. B.: 1987, *A&A* **177(1-2)**, 265
- Wanders, A. J. M.: 1934, *ZAp* **8**, 108
- Wedemeyer-Böhm, S. and Rouppe van der Voort, L.: 2009, *A&A* **503**, 225
- Wiehr, E.: 1978, *A&A* **69**, 279
- Wiehr, E.: 1985, *A&A* **149(1)**, 217

Yadav, N., Cameron, R., and Solanki, S.: 2020, in *AAS/Solar Physics Division Meeting*, Vol. 52 of *AAS/Solar Physics Division Meeting*, p. 201.07

Yeo, K. L., Solanki, S. K., and Krivova, N. A.: 2013, *A&A* **550**, A95

Zwaan, C.: 1965, in R. Lust (ed.), *Stellar and Solar Magnetic Fields*, Vol. 22 of *IAU Symposium*, p. 277

Acknowledgements

Foremost, I am deeply indebted to my doctoral advisors - Prof. Dr. Sami Solanki and Dr. Michiel van Noort - without whose expert guidance this thesis would have not been possible. The depths of their scientific expertise and insight are inspirational, and my discussions with them have been a rich learning experience. I am very grateful for their time, patience and continued support, especially during periods of difficulty, and for their scrupulous corrections and feedback on the dissertation.

Two other scientists who inspired and encouraged me are Dr. Dipankar Banerjee and Dr. Bernd Inhester - the internships I pursued under their guidance turned my nascent interests in solar physics into a desire to apply for the PhD. I also thank the SLAM group and the larger scientific community at MPS for interesting talks and lectures, and Dr. Ivan Milic (an excellent teacher) in particular. His lectures on the theory of radiative transfer and spectropolarimetric inversions were extremely helpful to me in developing a better understanding of the subject during my initial years, and he was always available for discussions, patient, and enthusiastic in answering my questions.

Life in Göttingen would have been very different without the interactions I have had with my fellow PhD students. They have given me memories I will cherish for a long time. I would like to thank the present and past members of MegaGauss - especially Felix Mackebrandt, Alessandro Cilla, and Theodosios Chatzistergos - with whom I have had the pleasure of jamming and performing at various events. Equally wonderful has been the time I spent with Eliana Amazo-Gomez, Sebastian Castellanos, Fatima Kahil, Paul-Louis Poulhier, Majid Pourabdian, Mariangela Viviani, and Sihane Merouane, with whom I have had numerous lively discussions on topics both scientific and otherwise.

I would like to thank Dr. Sonja Schuh, the program co-coordinator of the International Max Planck Research School (IMPRS), for inviting me to apply for the PhD program, and for providing crucial help with administrative duties and tasks. I also thank Dr. Natalie Krivova, Prof. Dr. Ariane Frey, Prof. Dr. Andreas Tilgner, and Prof. Dr. Hardi Peter for agreeing to be members of my defence panel, and Prof. Dr. Ansgar Reiners for agreeing to be a referee for this thesis, in addition to providing valuable input during TAC meetings.

I would like to express my gratitude to Ameya Prabhu, Rakshit Joshi, Mayukh Panja, Franziska Zeuner, Bianca Scholz, Hannah Moritz, and my friends back home for their incredible support during the later years of my PhD, and for their belief in my abilities even when I had none. They deserve a special mention.

Finally, I dedicate this thesis to my family back home. They have supported me in all

Acknowledgements

my endeavours, through the ups and downs, and I can never thank them enough for their love and sacrifices.

Curriculum vitae and publications

Personal Information

Name: Sudharshan Saranathan

Date of birth: 21/06/1992

Place of birth: Chennai, India

Education

2017 – 2021: PhD, Physics
International Max Planck Research School for Solar System Science (IMPRS), Georg-August-Universität Göttingen, Germany
Thesis: *Analysis of solar faculae using stray-light-corrected spectropolarimetric data and numerical simulations*

2009 – 2014: Integrated B.Sc + M.Sc, Physics
Indian Institute of Technology Kharagpur, West Bengal, India
Thesis: *Application of Genetic Algorithm (GA) to K-Means clustering*

Work Experience

2014 – 2015: Applications Development Engineer
KLA-Tencor Software India Private Limited, Chennai, India

Scientific Publications

- Saranathan, S., van Noort, M., Solanki, S. K.: Correction of atmospheric stray light in restored slit spectra, *Astronomy and Astrophysics*, in press, DOI: 10.1051/0004-6361/201937100

References

- Prof. Dr. Sami K. Solanki, Max-Planck Institut für Sonnensystemforschung, Göttingen: solanki@mps.mpg.de
- Dr. Michiel van Noort, Max-Planck Institut für Sonnensystemforschung, Göttingen: vannoot@mps.mpg.de